UC Santa Barbara

UC Santa Barbara Electronic Theses and Dissertations

Title

Transparent Conducting Oxide Clad Limited Area Epitaxy Semipolar III-nitride Laser Diodes

Permalink

https://escholarship.org/uc/item/07v9q6nj

Author

Myzaferi, Anisa

Publication Date

2016

Peer reviewed|Thesis/dissertation

eScholarship.org Powered by the California Digital Library
University of California

UNIVERSITY OF CALIFORNIA

Santa Barbara

Transparent Conducting Oxide Clad Limited Area Epitaxy Semipolar III-nitride Laser Diodes

A dissertation submitted in partial satisfaction of the

requirements for the degree of

Doctor of Philosophy

In

Electrical and Computer Engineering

by

Anisa Myzaferi

Committee in charge:

Professor Steven P. DenBaars, Chair

Professor Shuji Nakamura

Professor James S. Speck

Professor Nadir Dagli

December 2016

The dissertation of Anisa Myzaferi is approved.

_____

Professor James S. Speck

_____

Professor Shuji Nakamura

_____

Professor Nadir Dagli

_____

Professor Steven P. DenBaars, Committee Chair

May 2016

Transparent Conducting Oxide Clad Limited Area Epitaxy Semipolar III-nitride Laser Diodes

Copyright © 2016

by

Anisa Myzaferi

Dedicated to my remarkably loving parents, Meleq and Miranda.
Thank you for never giving up on me.
Kjo ishte për ju.

Me sy cilun afër djepit,
Me kujdes e me dashtni,
Për vaj tem tue hjekun zi,
Tue shëndue kur m'shifshi n'shënd.

Babë e nanë sa keni derdhë
Mbi shteg tem e hire e dritë;
Ah, sa mirë m'keni gatitë
Për ç'do kohë e për ç'do vënd.

Ju ma ndez't nji flakë në zemër
Për punë t'na`lta e për lumni
Për ju pra, o prind't e mi,
Mënd e zëmra më lakmon.

- *Ndre Mjeda*

ACKNOWLEDGEMENTS

This dissertation wouldn't have been possible without the guidance and trust of my committee members, particularly Prof. Steve DenBaars. I would like to thank Steve for taking me into his group, trusting me with a multi-faceted interdisciplinary project, and supporting me unconditionally throughout my time at SSLEEC. I would like to also thank Prof. Jim Speck for all the materials science knowledge he introduced me to and thank Prof. Nakamura for his encouragement and support at all stages of my dissertation. I would like to thank Prof. Dagli for asking insightful questions during my qualifier that opened new avenues for me to pursue while developing the optical modeling portion of my research. I also thank Prof. Dagli for being the first professor to teach me intuitive understanding of electromagnetism.

I would like to single out Dr. Bob Farrell, without whom, my understanding of my project wouldn't be at its current level. I can't thank him enough for all he's taught me about MOCVD growth, processing troubleshooting, modeling approaches and just overall being a great mentor. I'm really lucky to have worked with you. I also have a lot of gratitude towards Dr. Dan Cohen, whose guidance helped grow my theoretical understanding of the challenges of my project as well as help me setup and develop the optical modeling executed in this dissertation. Dr. Erin Young has been a rock for me ever since I joined the SSLEEC and I can't thank her enough for unconditionally supporting as I learned how to do research as well as inspiring unparalleled professionalism and a genuine friendship.

I want to thank Dr. Matt Hardy and Dr. Dan Haeger for getting me started on my project and teaching me MOCVD growth and III-nitride laser processing. Their outstanding mentorship got me hitting the ground running and I owe my early success to them. I also can't thank the UCSB cleanroom staff enough for their unparalleled support with everything and anything to with processing. Brian, Aiden, Tony, Don, Adam, Bill, Tom- you guys are seriously phenomenal.

I am thankful for the SSLEEC administrators and MOCVD engineers for always supporting us and helping our research run smoothly.

Grad school wouldn't have been the same without the support, love and jokes of all my friends. Virginia, Sarah, Christine, Jestha, Jerry, Selvi, Leah, Tanya, Joe, Erin, Stacy, Chris, Tom, Chandra, Chelsea, Yoni, Takako, Mike, Jacquie, Rob, Barbara, Sami, Anne and Patrick – I love you guys. Couldn't have done this and keep sane without all of you.

Finally, and most importantly, I would like to thank my family. My parents are unbelievably amazing human beings who have showed me what unconditional love, support, and loyalty mean. They've sacrificed so much for me and taught me all I could possibly ever need to have a good life. I'm beyond lucky to be your daughter.

Curriculum Vitae

ANISA MYZAFERI

EDUCATION

University of California Santa Barbara (UCSB) ***Santa Barbara, CA***
Doctor of Philosophy in Electrical Engineering and Photonics ***December, 2016***
Thesis Title: Transparent Conducting Oxide Clad, Limited Area Epitaxy Semipolar III-Nitride Lasers
Thesis Committee: Prof. Steven P. DenBaars, Prof. James S. Speck, Prof. Shuji Nakamura, Prof. Nadir Dagli

Northwestern University (NU) ***Evanston, IL***
Master of Science in Electrical Engineering Solid State ***December 2010***
Research Project: Optical Coatings for the improved performance of Quantum Cascade Lasers
Research Advisor: Manijeh Razeghi

Bachelor of Science in Electrical Engineering ***June 2009***

RESEARCH EXPERIENCE

UCSB Solid State Lighting and Energy Electronics Center (SSLEEC) ***Santa Barbara, CA***
PhD Candidate · January 2013 – Present

Device highlights

- Demonstrated the first continuous wave LAE-ZnO $(20\bar{2}1)$ blue laser diode at UCSB
- Demonstrated the first hydrothermally grown ZnO top clad $(20\bar{2}1)$ blue InGaN/GaN laser diode
- Demonstrated the first ITO top clad limited area epitaxy $(20\bar{2}1)$ blue InGaN/GaN laser diode
- Enhanced high current density device performance of GaN LEDs at by replacing ITO current spreading layer with ZnO:Ga

Material growth and characterization

- Performed MOCVD epitaxial growth of InGaN and AlGaN based blue and green laser diodes on LAE patterned semipolar GaN substrates
- Developed and performed aqueous solution growth of ZnO transparent conducting oxide (TCO) for laser diode cladding and LED current spreading layers
- Executed structural, optical and electrical characterization of MOCVD grown III-nitride material using X-ray diffraction (XRD), reciprocal space maps (RSMs), photoluminescence (PL), Cathodoluminescence (CL), fluorescence microscopy (FM), electroluminescence (EL), and secondary ion mass spectroscopy (SIMS)
- Conducted full laser diode electrical and optical device characterization

Laser diode processing and fabrication

- Processed semipolar GaN substrates for limited area epitaxy (LAE)
- Processed semipolar GaN-based edge emitting lasers with etched and polished facets
- Improved dicing process for polished facet laser fabrication to increase device yield

Device optical modeling and design

- Employed Fimmwave software to simulate the effect of cladding and waveguide design on the optical modes of TCO top clad $(20\bar{2}1)$ GaN lasers in the blue and green spectral regions

- Evaluated the performance of ZnO compared to ITO as the TCO top cladding layer for the design permutations of $(20\bar{2}1)$ GaN lasers in the blue and green spectral regions

University of California Santa Barbara Molecular Beam Epitaxy Lab ***Santa Barbara, CA***
Graduate Research Assistant · *May 2011 – December 2012*

- Processed of ErSb:GaSb material for electrical properties characterization
- Investigated anisotropic electrical conductance and magnetoresistance of ErSb nanostructures embedded in GaSb

Northwestern University Center for Quantum Devices (CQD) ***Evanston, IL***
Research Assistant · June 2008 – December 2010

Quantum Cascade Laser (QCL) processing and fabrication

- Processed lasers with buried ridge and Fabry Perot laser geometries
- Fabricated and packaged processed lasers into epi-layer up and epi-layer down bonding configurations

QCL performance testing

- Performed PIV and lifetime testing in pulsed and continuous wave (CW) mode operation of optically coated QCLs
- Determined laser core parameters with temperature dependent PIV testing and analysis in both pulsed and CW operation
- Characterized and analyzed QCL structural and optical performance using Scanning Electron Microscopy, Fourier Transform IR (FTIR) spectroscopy, and far field laser beam measurements.

Ion Beam Sputtering Deposition

- Focused on SiO_2 and Y_2O_3 single-layer, dielectric thin film deposition for anti-reflection and high-reflectance optical coatings for improving QCL optical performance
- Performed optical transmittance and reflectance FTIR measurements of the thin film dielectric materials
- Evaluated the surface morphology of the thin film dielectric materials using Atomic Force Microscopy (AFM)

III-V semiconductor MOCVD material growth

- Executed the MOCVD material growth of InP-based, Quantum-Dot-in-a-Well Infrared Photodetectors (QDWIP)
- Developed an Iron (Fe) doped InP regrowth procedure for buried ridge QCL channels
- Mastered and conducted optical, structural and electrical QDWIP and InP-based material characterizations.

TECHNICAL SKILLS

Semiconductor and transparent conducting oxide material growth
Class 1000 cleanroom experience; Metal Organic Chemical Vapor Deposition (MOCVD) operation, system maintenance and support; Aqueous solution growth of ZnO TCO; Heated electron beam deposition of ITO TCO

Semiconductor and dielectric material characterization
Scanning Electron Microscopy (SEM); High Resolution X-ray Diffraction (HRXRD); Atomic Force Microscopy (AFM); Surface optical profiling; Photoluminescence measurements; Electric Capacitance-Voltage (ECV) Profiling; Van der Pauw Hall measurements; Cathodoluminescence (CL); Florescence Microscopy (FM); Ion Beam Sputtering Deposition (IBSD) operation and system maintenance

Semiconductor Material Processing
Projection stepper and UV photolithography; Rapid thermal annealing (RTA); Gold wire bonding for device packaging; Metal electron beam evaporation; Sputter deposition; Electron cyclotron resonance (ECR) dry

etching; Reactive ion (RIE) dry etching; Chemical wet etching; Plasma enhanced chemical vapor deposition (PECVD); Semiconductor dicing, lapping and polishing

LEADERSHIP

UCSB Science and Industry Exchange (SciiX) ***Santa Barbara, CA***
Co-Founder and President · Summer 2012 - Spring 2014

- Founded new niche graduate student group aimed at fostering personal interaction with industry professionals
- Initiated and developed professional mentorship and partnership with scientists from the Howard Hughes Laboratories (HRL), Wyatt Technology Corporation, Northrop Grumman Corporation, Aurrion Inc., Soraa Inc., Raytheon Vision Systems, DuPont Technologies, Dako, Lockheed Martin, Image Searcher, CamFind and Transphorm, Inc.
- Organized and moderated the following events:
  - Post Graduate Careers Industry Panel
  - Evening with Entrepreneurs- CamFind App: from idea to product release
  - Summer Career Workshop- Negotiating salaries, surviving your first job after graduation, dealing with adversity in the workplace
  - Resume Workshop- Resumes, CVs, cover letters
- Coordinated and participated in site visits to the following companies: HRL, Aurrion, Lockheed Martin
- Secured funding and sponsorship, totaling $3,500, for these events from UCSB Graduate Division, the UCSB Center for Science and Engineering Partnership and Professional Development Series, the Materials Research Laboratories (MRL), and the California NanoSystems Institute (CNSI)

NU Society of Women Engineers ***Evanston, IL***
Executive Board Alumni Relations Chair · Executive board 2008; Involvement 2005 – 2009

- Activities Coordinator: Career Day for Girls –
- Upperclassman mentor to incoming freshmen
- Community outreach activities volunteer: Industry Day organizing volunteer

NU SAE Mini-Baja Car Construction Team ***Evanston, IL***
Electronics Specialist and Executive Board Treasurer and External Relations · 2007 – 2008

- Designed and installed the electrical circuits for the brake and reverse lights for the NU car in compliance with the SAE Mini-Baja design competition guidelines
- Drafted and presented a proposal that won the team a $10,000 FORD Motor Co. sponsorship

PUBLICATIONS and CONFERENCE PROCEEDINGS

- **A. Myzaferi,** A.H. Reading, R.M. Farrell, D.A. Cohen, S. Nakamura, J.S. Speck, S.P DenBaars (2015). "ZnO transparent conducting oxide clad $(20\bar{2}1)$ semipolar blue InGaN/GaN laser diodes", In preparation to be submitted to Appl. Phys. Express

- **A. Myzaferi,** A.H. Reading, R.M. Farrell, D.A. Cohen, S. Nakamura, J.S. Speck, S.P DenBaars (2015). "Transparent conducting oxide clad limited area epitaxy semipolar III-nitride laser diodes", *Applied Physics Letters, Vol* ***109****, 061109 (2016)*

- A.J. Mughal, S. Oh, **A. Myzaferi**, S. Nakamura, J.S. Speck, S.P DenBaars (2015). "High power LEDs using Ga-doped ZnO current spreading layers", *Electronic Letters Vol.* ***52****, Issue 4, p. 304-306 (2016)*

- **A. Myzaferi,** *et al* (2015). Transparent conducting oxide clad limited area epitaxy semipolar III-nitride lasers. Oral presentation at the *42nd International Symposium on Compound Semiconductors,* Santa Barbara, CA.

- **A. Myzaferi,** *et al* (2014). First Demonstration of hydrothermally grown ZnO clad (20-21) semipolar InGaN/GaN laser diode. Oral presentation at the *56th Annual Electronics Materials Conference (EMC),* Santa Barbara, CA.

- N. Bandyopadhyay, Y. Bai, B. Gokden, **A. Myzaferi**, S.Tsao, S. Slivken and M. Razeghi (2010). "Watt level performance of quantum cascade lasers in room temperature continuous wave operation at λ~3.76 μm," *Applied Physics Letters*, Vol. **97**, No.131117.

- S. Tsao, **A. Myzaferi**, and M. Razeghi (2010). "High Performance quantum dot-quantum well infrared focal plane arrays," SPIE Proceedings, Vol. **7605**, p.76050J-1.

- T. Yamanaka, B. Movaghar, S. Tsao, S. Kuboya, **A. Myzaferi** and M. Razeghi (2009). "Gain-length scaling in quantum dot/quantum well infrared photodetectors," *Applied Physics Letters, Vol.* ***95****,* 093502.

- **A. Myzaferi** and M. Razeghi. "*Atomic Scale Characterization of Quantum Cascade Laser Structural Properties*", 19th Argonne National Lab Annual Symposium for Undergraduates in Science, Eng. and Mathematics, Argonne, IL 2008; Abstract **87**.

ACADEMIC TEACHING EXPERIENCE

UCSB *Department of Electrical and Computer Engineering*

- ECE 2B: Circuits, Devices and Systems II with Prof. John Shynk ***Winter 2013***
- ECE 137B: Circuits and Electronics II with Prof. Luke Theogorajan ***Spring 2013***
- ECE 2A: Circuits, Devices and Systems I Head Teaching Assistant with Prof. Hua Lee ***Fall 2013***
- ECE 162: Fundamentals of Solid State with Prof Steve DenBaars ***Winter 2014***

  Responsibilities included:
  - Lead weekly lab session for ECE 2A
  - Lead weekly discussion session and supplementary lectures for ECE 132B

- Assignment grading and held weekly office hours for all classes
- ABET review material collection for ECE 2A

AWARDS

- SSLEC Outstanding Graduate Student Research Achievement Award · 2013
- UCSB Doctoral Scholars Fellow · 2011-2015
- R.R. McCormick School of Engineering and Applied Science High Honors · 2008-2009
- NU Society of Women Engineers Outstanding Junior of the Year Award · 2008
- *James F. Gibbons Endowed Scholarship · 2008-2009*
- *Joseph Blazek Foundation Scholarship · 2005-2009*
- *Warren H. Cook Memorial Scholarship · 2005*

PROFICIENCY

- ***Programming & Modeling Software*** - Origin Pro, X'Pert Epitaxy, L-Edit, MATLAB and Fimmwave
- ***Linguistic*** - Fluent in Albanian; can translate from Italian and Spanish into English; basic German

ABSTRACT

Transparent Conducting Oxide Clad Limited Area Epitaxy Semipolar III-nitride Laser Diodes

by

Anisa Myzaferi

Basal plane III-nitride laser diodes have been commercialized for wide ranging technologies, including pico projectors for solid state RGB displays, optical data storage and automotive headlights. Active research is focused in solid state lighting and visible light communications. Despite widespread commercialization, c-plane devices are affected by the inherent spontaneous and piezoelectric polarizations of the basal plane. These polarization effects are significantly reduced in semipolar planes of GaN, creating a vast design space for III-nitride optoelectronic devices.

III-nitride semipolar laser design and performance are considerably affected by the material composition and growth conditions of the cladding layers. The bottom cladding design is limited by stress relaxation of ternary alloys while the top cladding is limited by the growth time and temperature of the p-type (Al,In,Ga)N layers. These design limitations have been independently addressed by using limited area epitaxy (LAE) to enable n-AlGaN bottom cladding layers and by using thin p-GaN and transparent conducting oxide (TCO) top cladding layers.

In this work, we investigate a new laser design that simultaneously incorporates LAE-enabled n-AlGaN bottom cladding and thin p-GaN and TCO top cladding layers in $(20\bar{2}1)$ III-nitride laser structures. We evaluate the performance of two different TCOs as the top cladding layer: indium-tin-oxide (ITO) and zinc oxide (ZnO). Thorough optical modeling of the LAE-TCO laser design will be discussed for various Al compositions in the LAE-enabled n-AlGaN bottom cladding and varying p-GaN thicknesses in the top cladding. The LAE-TCO laser design was first demonstrated using ITO as the top cladding layer, with pulsed lasing achieved at 446 nm with a threshold current density of 8.5 kA/cm^2 and a threshold voltage of 8.4 V. Insights from the optical modeling in conjunction with improvements in the LAE-TCO laser fabrication process led to the demonstration of the LAE-TCO design using ZnO as the top cladding layer, with pulsed lasing achieved at 445 nm with a threshold current density of 5.6 kA/cm^2 and a threshold voltage of 6.7 V. This notable improvement in threshold current density and voltage led to the first continuous wave (CW) operation of blue $(20\bar{2}1)$ LAE-ZnO laser structures.

1

Introduction

1.1 Introduction to III-nitride material system

GAN and its ternary and quaternary alloys constitute a very versatile material system for optoelectronic device design and development. The wurtzite III-nitride has direct bandgap emission, which ranges from 0.7 eV to 6.2 eV.[1–5] This emission range spans the full spectrum and enables light emitting diode (LED) and laser diode (LD) operation in infrared, visible and UV wavelengths.[6] The breakthrough of high quality p-GaN doping was the essential

development that really established the III-nitride material system as a powerhouse in the optoelectronic market. [5,7–9]

State-of-the-art III-nitride LEDs and LDs are grown on the *c*-plane wurtzite crystal structure.[10,11] Despite widespread commercialization, *c*-plane devices are nonetheless affected by the inherent spontaneous and piezoelectric polarizations of the basal plane.[12–14] The negative impacts of *c*-plane polarization fields include fixed charges at heterointerfaces that cause spatial separation between electron and hole wave functions that reduces radiative recombination probability,[14–16] the occurrence of the quantum confined Stark effect (QCSE),[17,18] and *V*-defects during metalorganic chemical vapor deposition growth (MOCVD)[19,20].

In contrast, these polarization discontinuities can be significantly reduced in semipolar planes and eliminated in nonpolar planes of GaN, creating a wide design space for III-nitride optoelectronic devices.[21,22] Semipolar planes also have favorable band structure for higher gain relative to *c*-plane due to increased splitting of the valence band and reduced hole mass or increased curvature of the valance bands.[23–25] These benefits are predicted to be more prominent in the $(20\bar{2}1)$ plane relative to the basal plane.[25–27] Semipolar LDs have several advantages over *c*-plane LDs, including reduced transparency carrier density, increased optical gain, and reduced blue shift in wavelength with increasing current density.[22,28]

1.2 GaN-based laser applications and design

The applications of semipolar GaN-based lasers have been discussed at length in literature.[2,10,11,15,29–33] Such LD-based applications include visible light communications (VLC)[34–39], laser based solid state lighting,[11,15,30] and pico projectors.[40,41] The recurring goal of GaN-based laser research it to develop laser structures with low threshold conditions, high output power in pulsed or continuous wave operation, low differential resistance and high differential resistance and wall plug efficiency. There are many components of a laser structure that can be optimized, but this dissertation we will only focus on top and bottom cladding design. The next two sections, Chapter 1.3 and 1.4, will outline the design limitations for each cladding, some of the current solutions to these limitations. Chapter 1.5 will outline the new proposed $(20\bar{2}1)$ laser design structure that we aim to develop and demonstrate.

1.3 GaN-based laser top cladding design

The top cladding for III-nitride LDs is typically comprised of p-type (Al,In,Ga)N layers. The performance of these devices is limited by the high electrical resistivity and growth temperature of p-type AlGaN. Several groups have investigated improving p-AlGaN resistivity for various Al compositions and

by various growth and doping methods.[42–48] All of these studies consistently found p-AlGaN resistivity to be higher than p-GaN resistivity. High resistivity layers are not desirable because they increase device operating voltages. p-AlGaN cladding layers are normally grown at temperatures higher than 1030 °C.[49] Such high p-cladding growth temperatures result in thermal damage of the InGaN quantum wells (QWs) in the active region, particularly for blue and green LDs, which require higher In contents (>15%).[50] To mitigate these issues, p-cladding can be grown cooler than optimal temperatures,[51] but this approach leads to increased electrical resistivity of the p-cladding layers. This increases the operating voltage and heating and reduces the wall plug efficiency of GaN LDs.

An alternative to growing AlGaN p-cladding at lower than optimal temperatures is to utilize non-epitaxial cladding layers to replace a part of the III-nitride p-cladding. Violet and blue *c*-plane LDs have been demonstrated using evaporated/sputtered Ag and APC (Ag-Pd-Cu) alloy and indium-tin-oxide (ITO) top claddings.[52–54] The benefit of this design is noticeably increased refractive index contrast in the GaN-based laser waveguide due to the very low refractive index value of Ag, namely $n_{Ag} = 0.17 + 2.0i$ in blue wavelengths.[52] The downside of metal top cladding though is the really high loss of the metal, which means that even low optical mode overlap with the non-epitaxial top cladding will increase the overall internal mode loss of the device. Therefore, this is not an optimal solution to mitigating p-AlGaN related top cladding design limitations.

A likeminded designs solution, calls for replacing part of the III-nitride top cladding with a transparent conducting oxide (TCO). This top cladding design is a viable approach if the TCO provides adequate refractive index contrast to ensure optical mode confinement without introducing significant optical loss to the LD structure. A top cladding consisting of replacing thick p-AlGaN with thin p-GaN and a TCO layer reduces both growth time and temperature of the III-nitride cladding layer, thus reducing the thermal damage to the InGaN quantum wells (QWs). It also benefits LD performance by reducing the p-cladding bulk resistance because it enables a switch from thick p-AlGaN to thin p-GaN. This design has been used to demonstrate a $(20\bar{2}1)$ blue InGaN QW laser structure, using a Sn-doped In_2O_3 (ITO) layer in the top cladding. The device lased at a threshold current density, J_{th}, of 6.2 kA/cm^2 and threshold voltage, V_{th}, of 8.9 V.[55]

1.4 GaN-based laser bottom cladding design

The bottom cladding material choice and thickness in semipolar III-nitride lasers has been limited to GaN by the strain relaxation that happens from the large lattice mismatch between GaN and III-nitride ternary and quaternary alloys.[56–61] Strain relaxation also dictates alloy thickness.[62] AlGaN bottom cladding is desired due to its increased refractive index contrast with GaN, which in increases with

increasing Al composition,[63] However, AlGaN has been precluded from planar semipolar LD design due to the presence of resolved shear stress on the *c*-plane, which leads to *c*-plane slip via glide of pre-existing threading dislocations (TDs).[64] This limitation has been overcome through the use of a pre-growth substrate patterning technique commonly referred to as limited area epitaxy (LAE).[65–67]

LAE involves patterning stripes of various widths on a substrate prior to epitaxial growth. The glide of pre-existing TDs across epitaxial interfaces introduces misfit dislocations (MDs), which enable stress relaxation. As mentioned, stress relaxation is what limits the composition and thickness of ternary alloys, such as the AlGaN bottom cladding. MDs can subsequently form at multiple interfaces and sufficiently close to the active region QWs to markedly decrease the efficiency of LDs. By breaking the surface planarity, the LAE mesas block TD glide so that only TDs that were originally within the mesa borders contribute to MD formation within the mesa area.[64] The resulting decrease in MD density delays the onset of plastic relaxation, which allows for the growth of coherent AlGaN (or InGaN) layers beyond the predicted Matthews-Blakeslee critical thickness. Our group has demonstrated that LAE can be used to create modulation doped n-AlGaN bottom clad semipolar III-nitride LDs.[68,69]

1.5 Limited area epitaxy – transparent conducting oxide semipolar GaN laser design

This dissertation aims to demonstrate blue $(20\bar{2}1)$ laser structures that simultaneously incorporate LAE-enabled AlGaN bottom cladding and a TCO-based top cladding. The inception of the LAE-TCO concept is shown in Fig. 1.1. By enabling the use of n-AlGaN in the bottom cladding, LAE makes it possible to use thinner p-GaN in the top cladding, which reduces thermal damage to the QWs and the contribution from the top cladding to the overall device resistance. In addition, the design increases the index contrast in the laser waveguide, which increases the confinement factor of the lasing mode. Both ITO and ZnO will be evaluated as TCO options for the top cladding layer through optical numerical modeling and experimentally using a polished facet laser fabrication process.

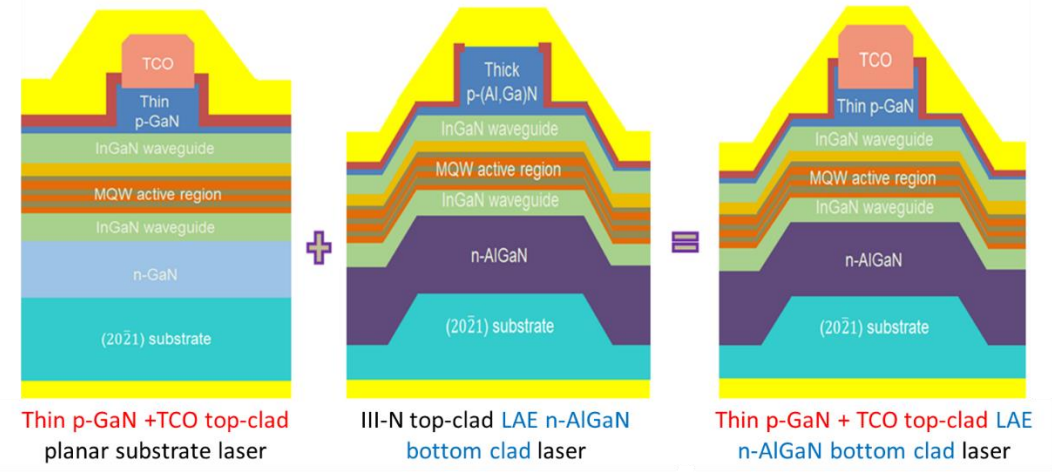

Figure 1.1 The building blocks of the proposed LAE-TCO semipolar laser structure. This design simultaneously incorporates LAE-enabled AlGaN bottom cladding and thin p-GaN and TCO top cladding. The TCOs that were evaluated in this dissertation are ITO and ZnO.

CHAPTER 1. INTRODUCTION

Based on the work in Reference 55, Chapter 2 will demonstrate the ability to replace ITO with hydrothermally deposited ZnO in the top cladding of a planar substrate, $(20\bar{2}1)$ laser. Chapter 3 will discuss the first demonstration of the LAE-TCO LD concept using ITO in the top cladding and 5% Al composition in the AlGaN bottom cladding. Chapter 4 will discuss an optimized LAE-TCO LD with ZnO in the top cladding and % Al composition in the AlGaN bottom cladding. This effort led to the first continuous wave (CW) $(20\bar{2}1)$ LD devices realized at UCSB.

Bibliography

[1] E.F. Schubert, *Light Emitting Diodes*, 1st ed. (Cambridge University Press, Cambridge, United Kingdom, 2003).

[2] A. Avramescu, T. Lermer, J. Müller, C. Eichler, G. Bruederl, M. Sabathil, S. Lutgen, and U. Strauss, Appl. Phys. Express **3**, (2010).

[3] K. Kojima, U.T. Schwarz, M. Funato, Y. Kawakami, S. Nagahama, and T. Mukai, Opt. Express **15**, 7730 (2007).

[4] K. Okamoto, T. Tanaka, and M. Kubota, Appl. Phys. Express **1**, 722011 (2008).

[5] S. Nakamura, T. Mukai, and M. Senoh, Japanese J. Appl. Physics, Part 2 Lett. **30**, (1991).

[6] S. Nagahama, Proc. SPIE **5738**, 57 (2005).

[7] S. Nakamura, N. Iwasa, T. Mukai, and M. Senoh, Jpn.J.Appl.Phys. **31**, 1258 (1992).

[8] F.A. Ponce and D.P. Bour, Nature **386**, 351 (1997).

[9] I. Akasaki and H. Amano, J. Electrochem. Soc. **141**, 2266 (1994).

[10] D. Sizov, R. Bhat, J. Wang, D. Allen, B. Paddock, and C.E. Zah, Phys. Status Solidi Appl. Mater. Sci. **210**, 459 (2013).

[11] L.Y. Kuritzky and J.S. Speck, MRS Commun. **5**, 463 (2015).

[12] A.E. Romanov, T.J. Baker, S. Nakamura, and J.S. Speck, J. Appl. Phys. **100**, (2006).

[13] E.T. Yu, X.Z. Dang, P.M. Asbeck, S.S. Lau, and G.J. Sullivan, J. Vac. Sci. Technol. B Microelectron. Nanom. Struct. **17**, 1742 (1999).

[14] A. Strittmatter, J.E. Northrup, N.M. Johnson, M. V. Kisin, P. Spiberg, H. El-Ghoroury, A. Usikov, and A. Syrkin, Phys. Status Solidi Basic Res. **248**, 561 (2011).

[15] D.F. Feezell, J.S. Speck, S.P. Denbaars, and S. Nakamura, 1 (2013).

[16] F. Bernardini, V. Fiorentini, and D. Vanderbilt, **56**, 4 (1997).

[17] D.A.B. Miller, D.S. Chemla, T.C. Damen, A.C. Gossard, W. Wiegmann, T.H. Wood, and C.A. Burrus, Phys. Rev. Lett. **53**, 2173 (1984).

[18] S. Chichibu, T. Azuhata, T. Sota, and S. Nakamura, MRS Proc. **449**, 14 (1996).

[19] N. Sharma, P. Thomas, D. Tricker, and C. Humphreys, Appl. Phys. Lett. **77**, 1274 (2000).

[20] A. Chakraborty, S. Keller, C. Meier, B. a. Haskell, S. Keller, P. Waltereit, S.P. DenBaars, S. Nakamura, J.S. Speck, and U.K. Mishra, Appl. Phys. Lett. **86**, 31901 (2005).

[21] K.M. Kelchner, S.P. Denbaars, and J.S. Speck, in *Adv. Semicond. Semimetals*, edited by J.J. Coleman, C.A. Bryce, and C. Jagadish (Elsevier, n.d.), pp. 149–182.

[22] J.S. Speck and S.F. Chichibu, MRS Bull. **34**, 304 (2009).

[23] W.G. Scheibenzuber, U.T. Schwarz, R.G. Veprek, B. Witzigmann, and a. Hangleiter, Phys. Rev. B - Condens. Matter Mater. Phys. **80**, 1 (2009).

[24] K. Kojima, M. Funato, Y. Kawakami, and S. Noda, J. Appl. Phys. **107**, (2010).

[25] T. Melo, Y.-L. Hu, C. Weisbuch, M.C. Schmidt, A. David, B. Ellis, C. Poblenz, Y.-D. Lin, M.R. Krames, and J.W. Raring, Semicond. Sci. Technol. **27**, 24015 (2012).

[26] D. Sizov, R. Bhat, and C.E. Zah, J. Light. Technol. **30**, 679 (2012).

[27] M.T. Hardy, D.F. Feezell, S.P. DenBaars, and S. Nakamura, Mater. Today **14**, 408 (2011).

[28] Y. Zhao, R.M. Farrell, Y. Wu, and J.S. Speck, Jpn. J. Appl. Phys. **53**, 100206 (2014).

[29] M.H. Crawford, J.J. Wierer, a J. Fischer, G.T. Wang, D.D. Koleske, G.S. Subramania, M.E. Coltrin, J.Y. Tsao, R.F. Karlicek, and J. Rensselaer, **3**, (2013).

[30] J.J. Wierer, J.Y. Tsao, and D.S. Sizov, Laser Photonics Rev. **7**, 963 (2013).

[31] A. Pourhashemi, R.M. Farrell, D.A. Cohen, J.S. Speck, S.P. DenBaars, and S. Nakamura, Appl. Phys. Lett. **106**, 111105 (2015).

[32] H. Ohta, S.P. DenBaars, and S. Nakamura, J. Opt. Soc. Am. B **27**, B45 (2010).

[33] J.J. Coleman, A. Bryce, Catrina, and C. Jagadish, editors , *Advances in Semiconductor Lasers*, 1st ed. (Elsevier, 2012).

[34] C. Lee, C. Shen, H.M. Oubei, M. Cantore, B. Janjua, T.K. Ng, R.M. Farrell, M.M. El-Desouki, J.S. Speck, S. Nakamura, B.S. Ooi, and S.P. DenBaars, Opt. Express **23**, 29779 (2015).

[35] C. Lee, C. Zhang, M. Cantore, R. Farrell, S.H. Oh, T. Margalith, J.S. Speck, S. Nakamura, J.E. Bowers, and S.P. DenBaars, 2015 IEEE Summer Top. Meet. Ser. SUM 2015 **23**, 228 (2015).

[36] H. Burchardt, N. Serafimovski, D. Tsonev, S. Videv, and H. Haas, IEEE Commun. Mag. **52**, 98 (2014).

[37] D.C. O'Brien, L. Zeng, H. Le-Minh, G. Faulkner, J.W. Walewski, and S. Randel, IEEE Int. Symp. Pers. Indoor Mob. Radio Commun. PIMRC 1 (2008).

[38] D. O'Brien, Univ. Oxford. Retrieved from Http// … (2011).

[39] C. Lee, (n.d.).

[40] V. Bhatia, A.S. Bauco, H.M. Oubei, and D.A.S. Loeber, Proc. SPIE **7582**, 758205 (2010).

[41] U. Strauβ, S. Brüninghoff, M. Schillgalies, C. Vierheilig, N. Gmeinwieser, V. Kümmler, G. Brüderl, S. Lutgen, A. Avramescu, D. Queren, D. Dini, C. Eichler, A. Lell, and U.T. Schwarz, Integr. Optoelectron. Devices 2008 **6894**, 689417 (2008).

[42] M.L. Nakarmi, K.H. Kim, J. Li, J.Y. Lin, and H.X. Jiang, Appl. Phys. Lett. **82**, 3041 (2003).

[43] Z. Xiaowei, L. Peixian, X. Shengrui, and H. Yue, J. Semicond. **30**, 43002 (2009).

[44] S.-N. Lee, J. Son, T. Sakong, W. Lee, H. Paek, E. Yoon, J. Kim, Y.-H. Cho, O. Nam, and Y. Park, J. Cryst. Growth **272**, 455 (2004).

[45] T. Kinoshita, T. Obata, H. Yanagi, and S.I. Inoue, Appl. Phys. Lett. **102**, 2013 (2013).

[46] A. Castiglia, J.F. Carlin, and N. Grandjean, Appl. Phys. Lett. **98**, 96 (2011).

[47] Y. Chen, H. Wu, E. Han, G. Yue, Z. Chen, Z. Wu, G. Wang, and H. Jiang, Appl. Phys. Lett. **106**, 162102 (2015).

[48] H. Yu, E. Ulker, and E. Ozbay, J. Cryst. Growth **289**, 419 (2006).

[49] J. Kim, H. Kim, and S.N. Lee, Curr. Appl. Phys. **11**, S167 (2011).

[50] D.H. Yoon, K.S. Lee, J.B. Yoo, and T.Y. Seong, Japanese J. Appl. Physics, Part 1 Regul. Pap. Short Notes Rev. Pap. **41**, 1253 (2002).

[51] M.S. Oh, M.K. Kwon, I.K. Park, S.H. Baek, S.J. Park, S.H. Lee, and J.J. Jung, J. Cryst. Growth **289**, 107 (2006).

[52] D. Bour, C. Chua, Z. Yang, M. Teepe, and N. Johnson, Appl. Phys. Lett. **94**, (2009).

[53] B. Cheng, C.L. Chua, Z. Yang, M. Teepe, C. Knollenberg, A. Strittmatter, and N. Johnson, IEEE Photonics Technol. Lett. **22**, 329 (2010).

[54] C. Chua, Z. Yang, C. Knollenberg, M. Teepe, B. Cheng, A. Strittmatter, D. Bour, and N.M. Johnson, Proc. SPIE 7939 **7939**, 793918 (2011).

[55] M.T. Hardy, C.O. Holder, D.F. Feezell, S. Nakamura, J.S. Speck, D. a. Cohen, and S.P. DenBaars, Appl. Phys. Lett. **103**, 81103 (2013).

[56] A.E. Romanov and J.S. Speck, **2569**, 2001 (2009).

[57] F. Wu, A. Tyagi, E.C. Young, A.E. Romanov, K. Fujito, S.P. Denbaars, S. Nakamura, and J.S. Speck, **33505**, 0 (2014).

[58] E.C. Young, A.E. Romanov, C.S. Gallinat, A. Hirai, G.E. Beltz, and J.S. Speck, **41913**, 0 (2013).

[59] A.E. Romanov, E.C. Young, F. Wu, A. Tyagi, C.S. Gallinat, S. Nakamura, S.P. Denbaars, and J.S. Speck, J. Appl. Phys. **109**, (2011).

[60] A.E. Romanov, E.C. Young, F. Wu, A. Tyagi, C.S. Gallinat, S. Nakamura, S.P. Denbaars, and J.S. Speck, J. Appl. Phys. **109**, 1 (2011).

[61] A.E. Romanov, T.J. Baker, S. Nakamura, J.S. Speck, E. Jst, and U. Group, **23522**, 0 (2012).

[62] J.W. Matthews and A.E. Blakeslee, J. Cryst. Growth **27**, 118 (1974).

[63] R. Goldhahn, a. T. Winzer, a. Dadgar, a. Krost, O. Weidemann, and M. Eickhoff, Phys. Status Solidi Appl. Mater. Sci. **204**, 447 (2007).

[64] M.T. Hardy, Stress Engineering for Semipolar ($20\bar{2}1$) Blue and Green InGaN Based Laser Diodes, 2013.

[65] E.A. Fitzgerald, G.P. Watson, R.E. Preano, and D.G. Ast, **65**, 2220 (1989).

[66] E.A. Fitzgerald, P.D. Kirchner, R. Proano, G.D. Pettit, J.M. Woodall, D.G. Ast, E.A. Fitzgerald, P.D. Kirchner, R. Preana, G.D. Pettit, and J.M. Woodall, **1496**, 1 (1996).

[67] E.A. Fitzgerald, T.B. Laboratories, and M. Hill, (1991).

[68] M.T. Hardy, F. Wu, P. Shan Hsu, D.A. Haeger, S. Nakamura, J.S. Speck, and S.P. Denbaars, J. Appl. Phys. **114**, 0 (2013).

[69] M.T. Hardy, S. Nakamura, J.S. Speck, S.P. Denbaars, M.T. Hardy, S. Nakamura, J.S. Speck, and S.P. Denbaars, **241112**, (2012).

2

Zinc oxide top cladding planar substrate laser design

2.1 Introduction

THIS chapter introduces the planar substrate – transparent conducting oxide (TCO) laser design that was used to demonstrate the use of ZnO as a top cladding layer for semipolar III-nitride lasers. This design demonstration is important because finding an alternative TCO to the current industry standard is the first step towards realizing the limited area epitaxy (LAE) – TCO laser design. The current industry standard TCO, Sn-doped In_2O_3 (ITO), has an undesirable contribution to the internal loss of an edge emitting laser due to its high optical

absorption. This chapter presents the evaluation and implementation of ZnO as an attractive alternative to ITO. The evaluation metrics used to compare ZnO to ITO are considered in Chapter 2.2. The ZnO deposition method is presented in Chapter 2.2.1. The design space offered by the planar substrate-TCO laser design is explored through optical modeling and discussed in Chapter 2.3. The necessary processing and fabrication developments and device results are discussed in Chapter 2.4 and 2.5, respectively. As a first attempt, ZnO was incorporated onto a planar $(20\bar{2}1)$ laser structure to avoid processing complications that may arise from LAE pre-growth patterning of the device. This effort led to the demonstration of a $(20\bar{2}1)$ laser, operating at 8.6 kA/cm^2 and a threshold voltage of 10.3 V with a lasing wavelength of 453 nm.

2.2 ZnO: an attractive alternative to ITO

ITO has been the industry standard TCO choice, but its future use may be unsustainable given the high price of indium[1–3]. In addition, ITO has relatively high optical absorption, with literature values reported at 1000-2000 cm^{-1},[4–7] which is undesirable when designing low internal loss laser diodes (LDs). ZnO is an alternative TCO that can be used as the top cladding layer in III-nitride LDs.

ZnO is a wurtzite semiconductor, with a direct bandgap of 3.37 eV at room temperature,[8] whose *a* and *c* lattice parameters are 3.25Å and 5.20Å, respectively.[9]

CHAPTER 2: ZINC OXIDE TOP CLADDING PLANAR SUBSTRATE LASER DESIGN

Considering that the *c* lattice parameter of GaN is 5.18Å, the lattice mismatch between ZnO and GaN is only ~2%. This facilitates high quality single-crystal growth of ZnO on GaN, which is expected to result in higher carrier mobility. Such properties enable the implementation of ZnO for optoelectronic applications in the blue and UV regions such as LDs, light emitting diodes (LEDs) and photodectors. These applications are limited to n-type ZnO due to the lack of high quality and reproducible p-type ZnO, despite reports of p-type ZnO.[10,11]

ZnO is distinguished from other TCOs and semiconductors due to a wide list of optical, electrical and structural properties. ZnO has a high free-exciton binding energy of 60 meV, which indicates efficient excitonic emission in ZnO at room temperature, making it a promising material for optical devices utilizing excitonic effects.[12] ZnO has large piezoelectric constants and high sensitivity of surface conductivity in the presence of adsorbed species, making it optimal for implementation in sensors, actuators and transducers.[13] ZnO has strong luminescence [14] and large non-linear optical coefficients,[15] making it suitable for integrated non-linear optical devices. While the conductivity of crystalline ZnO is in the same order of magnitude as ITO,[5] polycrystalline ZnO has nonlinear resistance and non-ohmic current-voltage characteristics.[13] Structurally, ZnO has high thermal conductivity, giving it heat-sinking capabilities for optoelectronic devices.[13] Its various growth techniques, which will be listed subsequently, provide

both large bulk crystals and relatively thick current spreading layers, giving ZnO wide device application versatility. Additionally, ZnO is the least toxic TCO,[3] has high radiation hardness,[16] and is amenable to low-temperature wet chemical etching.[13]

To evaluate the feasibility of ZnO as an alternative TCO to ITO for LD top cladding, we looked at several performance metrics, some of which are summarized in Table 2.1. These metrics regard electrical characteristics, optical absorption, deposition method, fabrication process, and the cost of the TCO. The electrical properties shown in Table 2.1 were measured using the circular transmission line (CTLM) method, as described in Chapter 3 of Reference 9. For these comparisons *c*-plane GaN LEDs with TCO current spreading layer (CSLs) were fabricated. ITO was electron beam evaporated using a heated stage, while ZnO was deposited using the hydrothermal deposition method, which will be discussed in Chapter 2.2.1. As shown in Table 2.1, ITO has lower resistivity and specific contact resistivity than ZnO, but ZnO's values are on the same order of magnitude and comparable in

TCO	R_{SH} (kΩ/sq)	ρ_C (Ω-cm^2)	ρ (Ω-cm)	α_{opt} (cm^{-1})	n
ITO	972	1.9×10^{-3}	1.5×10^{-3}	2000	2.0
ZnO	331	6.6×10^{-3}	4.5×10^{-3}	100	2.0

Table 2.1 Electrical and optical properties of ITO and ZnO current spreading layers characterized by CTLM method. Electrical property data curtesy of Asad Mughal. The absorption coefficients and refractive indices for ITO and ZnO at 450 nm were taken from References 4 and 9, respectively.

performance. The results compared in Table 2.1 are limited to thoroughly hydrothermally deposited unintentionally doped (UID) ZnO and heated electron beam evaporated ITO, which were the two TCO growth methods utilized for all the work presented in this thesis. ZnO electrical properties are expected to improve with the iterative improvement of hydrothermal growth solution chemistry as well as through introducing dopants in ZnO, such as Ga, Al or In,[9,13] and/or through hybrid growth techniques such as combined atomic layer deposition (ALD) and hydrothermal growth of ZnO.

ZnO is an n-type semiconductor and forms a p-n heterojunction at the interface with the p-type GaN contact of optoelectronic devices. In this case, ohmic current flow requires high concentration of carriers in both n- and p- materials and an abrupt junction interface, enabling carriers to tunnel through the junction. As the LED or LD is under forward bias, with current flowing from n-GaN to the p-GaN layer, the n-ZnO – p^+GaN interface is placed under reverse bias and forms a tunnel junction.[9] Recent improvements in annealing conditions of hydrothermally deposited ZnO have also demonstrated that specific contact resistances of Ti/Au contacts to ZnO and ITO are comparable.[5] In addition, external quantum efficiency (EQE), luminous efficacy and series resistance were improved in LEDs with ZnO current spreading layers relative to ITO, indicating that ZnO layers had both lower absorption and lower contact resistance to p-GaN.[17] Introducing dopants has also

been used to demonstrate ZnO ohmic contacts to p-GaN.[18]

The biggest selling point for ZnO application to optoelectronic devices is its optical absorption coefficient, which is considerably lower than ITO in the blue and green regions of the visible spectrum.[4,9] The ITO absorption coefficient and refractive index shown in Table 2.1 were taken from Ref. 4. The ZnO absorption coefficient and refractive index were taken from Reference 9. The optical absorption coefficient in Reference 9 was calculated from UV-visible transmission spectra of UID ZnO hydrothermally deposited on spinel substrates. The calculation method developed by Cisneros[19] was used to evaluate the measured spectra. The UID ZnO film had an absorption coefficient of ~200 cm^{-1} in the violet region which dropped to ~100 cm^{-1} in the blue region and less than 100 cm^{-1} in the green region of the visible spectrum.[5,9] This is a marked improvement over the absorption coefficient of 2000 cm^{-1} measured in our ITO.[4]

Just like ITO, the measured refractive index of ZnO at 450 nm had a value of 2. The refractive index was calculated by fitting variable angle spectroscopic ellipsometry (VASE) data, as detailed in Appendix A of Reference 9. This is important for our proposed design, because ZnO having the same refractive index in the wavelength of interest means that the mode overlap with the TCO and optical confinement should not be affected by replacing ITO with ZnO in the top cladding, provided the rest of the laser structure is identical.

2.2.1 Hydrothermal deposition of ZnO

As stated above, the ZnO top clad laser designs presented in this thesis utilized hydrothermally deposited ZnO. When implemented in GaN optoelectronic devices, it is vital that the underlying p-GaN contact layer is not exposed to solutions or environments that would compensate or damage the p-GaN electrically or structurally. Therefore, the ZnO deposition method must provide highly conductive and high transparency ZnO, without compromising the epitaxial structure. ZnO can be grown through a series of methods, including bulk, epitaxial and physical deposition methods.

Bulk growth provides high quality bulk crystals with different impurity concentrations and varying levels of electro-optical performance, depending on the growth mechanism. Such mechanisms include gas or vapor transport, seeded chemical vapor transport and pressurized melt growth. While these methods provide excellent electrical properties for large ZnO boules, they often require either very high growth or annealing temperatures (up to 1600 K), pressures and long growth times,[20–23] which makes them impractical for ZnO thin film implementation into optoelectronic devices. Ideally, heteroepitaxial growth of ZnO thin films onto an LED or an LD would be preferred for reduced concentrations of extended defects, reduced impurity contamination and a seamless device fabrication process. ZnO thin film reactor growth has been demonstrated

using both metal organic chemical vapor deposition (MOCVD) and molecular beam epitaxy (MBE). High crystalline ZnO has been demonstrated using MOCVD, with growth temperatures ranging between 400 ^{o}C – 950 ^{o}C.[24–26] These ZnO temperatures are higher than the quantum well (QW) growth temperatures in our LD structures, thus defeating the purpose of TCO top cladding. In addition, the MOCVD precursors tend to pre-react outside the boundary layer, causing formation of powder residue in the growth chamber, which facilitates higher impurity incorporation in the TCO.[9] In addition, MOCVD growth rates can be very slow, thus increasing the device cost and fabrication time. MBE on the other hand offers good thickness control and in-situ monitoring of single crystalline ZnO thin films,[27] but while these films were highly conductive, they had very poor transparency,[28] rendering MBE grown ZnO non-suitable as LD top cladding.

In addition to epitaxial methods, a series of other methods including chemical spray pyrolysis, screen painting, electrochemical deposition, sol-gel synthesis and oxidation of Zn films can be used to grow varying qualities of polycrystalline ZnO, which is not applicable to our LD top cladding design.[13,29] Non-epitaxial techniques used for single-crystalline ZnO include physical vapor deposition methods, such as RF sputtering,[30,31] RF magnetron sputtering,[32] electron beam evaporation,[33] pulsed laser deposition,[34] and thermal evaporation.[35]

Sputtering can cause oxygen plasma damage, which will compensate the

underlying p-GaN layer. The other techniques require solid source materials with fixed composition and the ZnO films' electro-optic properties are highly dependent on deposition rates, chamber contamination and require frequent and costly system maintenance. Atomic layer deposition (ALD) provides conformal ZnO thin films with precise thickness and film quality control, but at the expense of very slow deposition rates.[36]

The ZnO growth techniques discussed so far are limited by growth rate, film quality, electro-optic properties, deposition temperature, vacuum conditions, system maintenance and cost. Hydrothermal growth of ZnO, which is also referred to as aqueous solution deposition, allows for the deposition of high conductivity and high transparency thin films, by mitigating the system, chemical sources and cost limitations of other methods. Hydrothermal growth is a well-established high temperature and pressure bulk single crystal ZnO growth method,[37] whose principles can be adapted to low temperature and atmospheric pressure growth conditions. Lange and co-workers have demonstrated single crystal ZnO growth capability using low temperature (90 ^{o}C) aqueous solution deposition.[38–41] Richardson *et. al.*[42,43] have provided insight into the mechanisms that dictate the growth conditions of ZnO in low temperature hydrothermal growth. These studies have shown how to control ZnO nucleation conditions to result either in a high

CHAPTER 2: ZINC OXIDE TOP CLADDING PLANAR SUBSTRATE LASER DESIGN

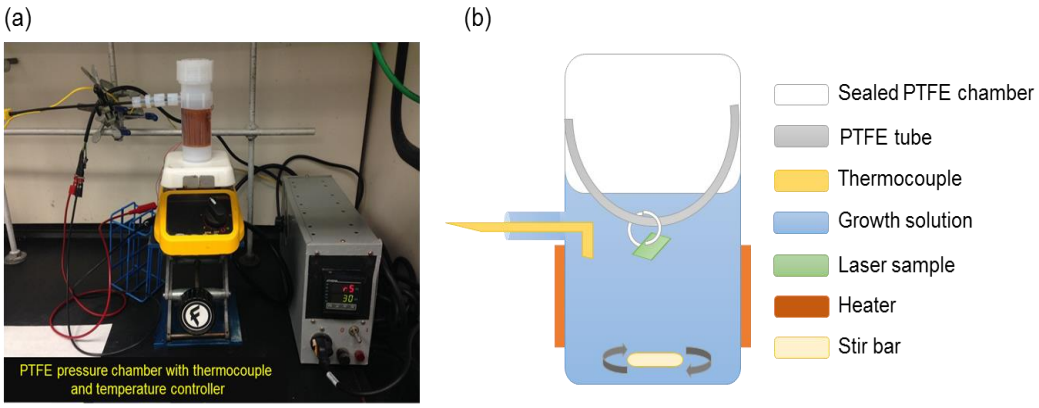

Figure 2.1 Low temperature hydrothermal deposition reactor design and setup: (a) photo of the actual experimental setup (b) cross sectional representation of the hydrothermal growth chamber. The solution for both ZnO layers is heated and maintained at 90 ^{o}C.

density of crystallites or a fully coalesced ZnO film on existing ZnO surfaces.

In this work, we used a hydrothermal deposition reactor design like the PTFE reactor used in Reference 9 to deposit ZnO top cladding on semipolar LDs. An image of the actual deposition vessel is shown in Fig. 2.1 (a). A cross-section of the reactor is shown in Fig. 2.1 (b): the reaction chamber's uniform temperature gradient is ensured by heating tape and monitored by a thermocouple which feeds into the heating tape's temperatures controller. The sample is held in place by in-house PTFE tubing design, with the growth surface facing downwards. A magnetic stir bar ensures uniform mixing of the growth solution and mitigates the formation of air bubbles on the growth surface.

Low temperature hydrothermal deposition synthesizes ZnO using a nitrate salt as the Zn source, ammonium hydroxide as the mineralizer and sodium citrate

Precursor	Seed layer	2nd layer
18 MΩ DI H_2O	90 mL	90 mL
Trisodium citrate $Na_3C_6H_5O_7$	0.1875 g	0.1875 g
Zinc nitrate hexa-hydrate $Zn(NO_3)_2{:}6H_2O$	0.75 g	0.75 g
Ammonium hydroxide NH_4OH 29% concentration	4.67 mL	4.67 mL
N_2 anneal	500 °C	250 °C

Table 2.2 List of precursors for low temperature hydrothermal ZnO two-layer deposition, including precursor amount and anneal temperatures. Both anneal times are 15 minutes.

as a crystal growth modifier, which affects preferential growth along certain crystal orientations.[38] The mineralizer modifies the pH of the solution and changes the solubility of the dissolved ions, thus controlling the thermodynamic driving force for the formation of the ZnO precipitates. Furthermore, a large amount of hydrogen is incorporated into the ZnO films during this growth method,[9] which acts as an interstitial donor[13] and results in high n-type carrier concentrations. All the precipitation reactions take place at 90 °C, which is crucial to our design, as we are trying to mitigate thermal damage to the active region that occur from extended high temperature top cladding and p-contact layer growth.

The hydrothermal deposition of ZnO as an LD top cladding consists of a two-layer sequence: a non-coalesced seed layer of ZnO crystallites and a fully coalesced second layer. Table 2.2 lists the precursors and their respective amounts

for each ZnO layer. Each layer is annealed in a nitrogen environment for improved ZnO film quality and adhesion to the underlying p-GaN. The annealing temperatures were investigated and optimized in Reference 9. Fig. 2.2 (a) conceptually shows the non-coalesced ZnO seed layer crystals. The SEM of seed layer crystals, shown in Fig. 2.2 (b) shows that their shape is irregular, but their height is ~250 nm. This result was similar to the seed layer thickness attained in Reference 9. ZnO grows preferentially on exposed GaN and tends to grow quicker along the $c+$ crystallographic direction, which is why ZnO will grow on $(20\bar{2}1)$ planes but not on $(20\bar{2}\bar{1})$.[9] Figs. 2.2 (c) and (d) show the growth concept and the

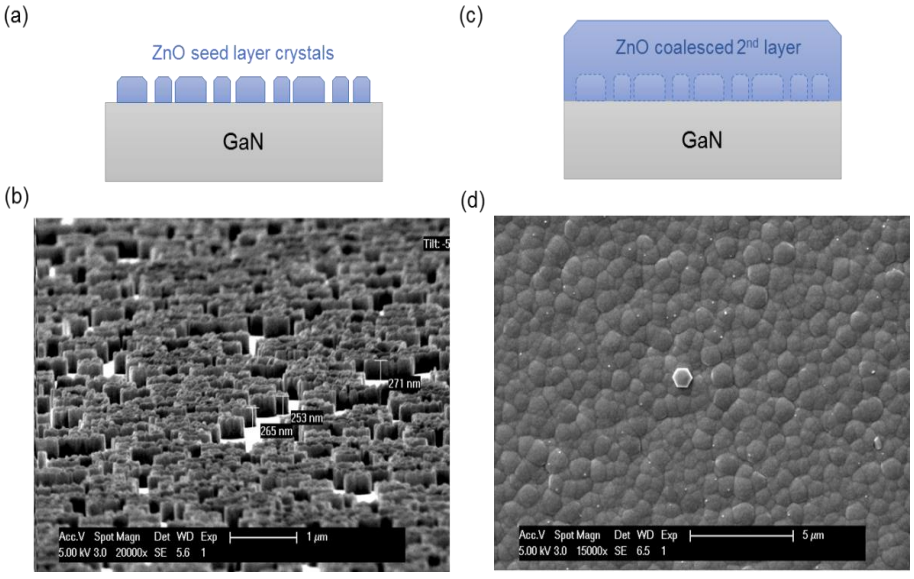

Figure 2.2 Low temperature hydrothermal deposition of bilayer ZnO: (a) Depiction of the seed ZnO layer, consisting of irregular ZnO crystals. (b) Side view SEM image of the seed ZnO layer, showing the varying crystal heights, shapes and spatial distribution. (c) Depiction of the second layer of ZnO, which is fully coalesced. (d) Top view image of the second layer of ZnO, which is fully coalesced and has irregular surface grain boundaries.

top view SEM of a fully coalesced second layer of ZnO. The SEM image shows well developed, relatively uniform grain size but irregular grain boundaries.

2.3 Optical modeling

Much like other designs that use non-epitaxial cladding layers, one benefit of using ZnO as a TCO layer is that it makes it possible to avoid the use of thick p-AlGaN layers and use thinner p-GaN layers in the top cladding. However, it is important to understand how the thickness of the p-GaN layers and the choice of TCO affects device performance. To investigate the effect of varying the thickness of the p-GaN layers, 2D optical modeling of the proposed laser structure were simulated using FIMMWAVE software. [44].

Fig. 2.3 outlines the laser structure used in the optical modeling. The modeled device III-nitride layer sequence consisted of a $(20\bar{2}1)$ free-standing GaN substrate, a Si_2H_6 doped GaN n-cladding, an InGaN n-waveguide (WG), a three quantum well active region, followed by a p-AlGaN electron blocking layer (EBL), an InGaN p-WG, and an Mg-doped GaN p-cladding and a TCO layer. The optical modeling evaluated both ITO and ZnO were evaluated as a TCO layer in the top cladding.

For each device layer, FIMMWAVE requires its thickness, refractive index

and absorption coefficient. The layer thicknesses used for the FIMMWAVE modeling structure were the same as the layers in the demonstrated device and are listed in Table 2.3. It is important to note that our GaN p-cladding has an Mg doping grade, therefore it is broken up into four different GaN layers. Absorption loss increases with increased doping levels;[45] we therefore gradually increase the Mg doping to minimize the material loss contribution of the p-cladding to the overall structure. The doping grade used for the demonstration of this device is not optimized and merits further investigation. The GaN, InGaN and AlGaN refractive indices were taken from Goldhahn *et. al.*[46] The ZnO used in the devices discussed

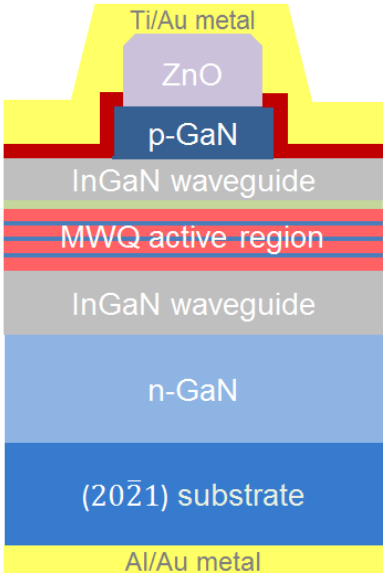

Figure 2.3 Laser structure used for optical modeling. The TCOs compared were ITO and ZnO, using ZnO for this illustration. The green layer above the quantum wells is the p-AlGaN EBL layer. The layer thicknesses and compositions used for optical modeling are detailed in Table 2.3.

Layer	Material	Thickness (nm)	Doping (cm^{-3})	Layer specific confinement factor (%)	Layer specific loss (cm^{-1})	Percentage of total loss (%)
TCO	ZnO	780	-	0.02	0.02	0.18
p^+ contact	GaN	11	3.74E+20	0.02	0.09	0.70
p^+ cladding	GaN	192	1.72E+19	3.52	0.92	**7.17**
p cladding	GaN	120	9.61E+18	13.92	1.95	**15.25**
p^- cladding	GaN	2	7.69E+18	0.44	0.05	0.41
p-waveguide	$In_{0.08}Ga_{0.92}N$	30	1.00E+19	7.79	1.40	**10.98**
p-EBL	$Al_{0.21}Ga_{0.79}N$	10	3.76E+19	2.42	1.19	**9.27**
QB 4	GaN	8.8	-	2.63	0.00	0.00
QW 3	$In_{0.2}Ga_{0.8}N$	4.8	2.45E+19	1.64	1.80	**14.10**
QB3	GaN	7.6	-	2.45	0.00	0.00
QW 2	$In_{0.2}Ga_{0.8}N$	4.8	2.45E+19	1.76	1.93	**15.12**
QB2	GaN	7.6	-	2.61	0.00	0.00
QW 1	$In_{0.2}Ga_{0.8}N$	4.8	2.45E+19	1.85	2.03	**15.91**
QB1	GaN	8.8	-	3.18	0.00	0.00
n-waveguide	$In_{0.08}Ga0_{.92}N$	70	2.92E+18	25.88	0.78	**6.07**
n-buffer	GaN	18	1.20E+18	4.78	0.10	0.75
n-cladding	GaN	378	1.20E+18	25.15	0.50	3.94
n-contact	GaN	630	2.24E+18	0.68	0.02	0.16
substrate	GaN	2000	-	0.002	0.000	0.00

Table 2.3 Layer sequence of LD used for optical modeling. The p-GaN top cladding thickness was varied from 10 nm to 900 nm; the example listed in this table has 325 nm p-GaN. The layers with the highest individual loss contribution are highlighted in bold in the last column. For this p-GaN thickness, the quantum wells, the electron blocking layer and the p-cladding contribute significantly to the overall internal loss, accounting for ~45 %, ~10% and ~22% of the total device loss, respectively. Doping optimization is expected to mitigate these layers' loss contribution.

in this work as well as in the optical modeling was unintentionally doped. The UID ZnO refractive index was measured using transmission spectroscopy, as detailed in Appendix A of reference 9. The ITO refractive index was taken from Hardy *et. al.*[4] The refractive index of both ITO and ZnO at 450 nm, which is the wavelength used in the optical modeling, is 2.[4,9] The absorption coefficient of ITO of 2000 cm^{-1} and the absorption coefficient of UID ZnO of 100 cm^{-1} were taken from Hardy *et. al.*[4] and Reading *et. al.*[5], respectively. As discussed in Chapter 2.2, the ITO absorption coefficient values reported in literature range from 1000 – 2000 cm^{-1} for blue wavelengths; we used the more conservative value of 2000 cm^{-1} from Reference 4 because this was ITO grown and characterized by MES AFTY corporation which has a more repeatable deposition quality than our in-house heated stage electron-beam deposited ITO.

The optical modeling in this work considers free carrier absorption to be the main significant contribution to internal loss. The absorption coefficients for the III-nitride layers were adapted from Kioupakis *et. al.*[47]: we used the layer loss values reported in Table 2 of Reference 47 and scaled them for our laser structure's secondary ion mass spectroscopy (SIMS) measured carrier densities. Mg-doped material loss was assumed to range from 10-15 cm^{-1} per 10^{19} cm^{-1} carrier concentration and Si-doped material loss was assumed to range from 1-2 cm^{-1} per 10^{18} cm^{-3} carrier concentration. We did not interpolate based on In content or any

other factor besides carrier concentration, so the calculated alloy scattering in our QWs, was a slight overestimate. Considering the low confinement factor of the active region, though, we believe this presented a minimal difference in internal loss. We considered calculating each component of the overall absorption loss per layer using the values in Table 1 of Kioupakis *et. al.*[47], but we did not know the defect concentrations of our LD's layers. Therefore, assuming our non-QW layers to have no alloy scattering, we estimated layer losses based on Table 2 of Reference 47, as described above.

The carrier concentration in the individual layers in the LD structure, excluding the QWs was taken from SIMS measurements. SIMS gives doping values per each layer and we are assuming 100% activation for these optical mode simulations. The assumed QW carrier concentration was calculated by adapting published estimates to our device's threshold conditions.[48]

FIMMWAVE calculates the confinement factor (Γ) and the internal loss (α_i) and then those values are used to calculate threshold material gain (g_{th}) and differential efficiency (η_d) using Equations 2.1 and 2.2, respectively.[49] In Eqn. 2.1, α_m is the facet mirror loss and in Eqn. 2.2 η_i is the injection efficiency. In this work we assumed uncoated laser facets and an η_i value of 65%.[48] All the modeling results presented in this thesis use the fundamental TE mode values calculated using the real FMM solver in FIMMWAVE.

CHAPTER 2: ZINC OXIDE TOP CLADDING PLANAR SUBSTRATE LASER DESIGN

$$g_{th} = \frac{1}{\Gamma}\left(\langle \alpha_i \rangle + \alpha_m\right), \tag{2.1}$$

$$\eta_d = \eta_i \frac{\alpha_m}{\alpha_m + \langle \alpha_i \rangle}, \tag{2.2}$$

Given that a TCO top cladding allows for thinner p-GaN layers, it was first important to determine how thin the p-GaN layer in the top cladding can be without compromising the lateral confinement of the optical mode. We determined this thickness limit by evaluating the dependence of Γ and α_i on p-GaN thickness ranging from 10 nm to 900 nm, for both ITO and ZnO, as shown in Fig. 2.4, using the LD structure shown in Fig. 2.3 and detailed in Table 2.3 as a baseline. We have poor control over the thickness of the hydrothermally deposited ZnO, therefore we also evaluated the Γ and α_i dependence on p-GaN thickness for different ZnO

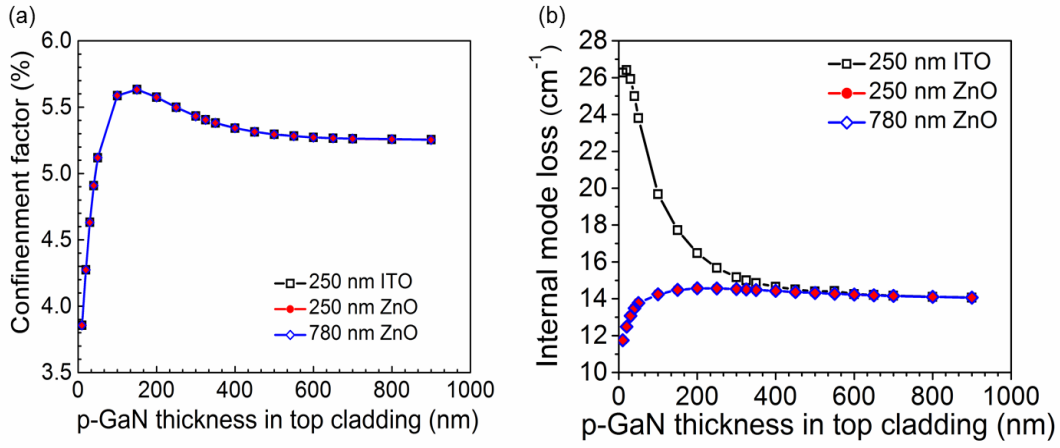

Figure 2.4 Dependence on varying p-GaN thickness in the top cladding for various TCO compositions and thicknesses of (a) confinement factor and (b) internal mode loss.

thicknesses: 250 nm for a direct ITO comparison and 780 nm, which was the deposited ZnO thickness on the demonstrated device, as will be discussed in detail in Chapter 2.5.

The immediate observations attained from the dependence of Γ and α_i on p-GaN thickness are that Γ does not depend on the TCO composition nor on the thickness of ZnO and that ZnO top cladding results in lower internal loss than ITO, independent of ZnO thickness. α_i also doesn't depend on the thickness of ZnO layer. The value of the confinement factor for both TCOs experiences a sharp decrease for p-GaN thicknesses of lower than 100 nm. This behavior relates to the minimum thickness of p-GaN in the TCO top cladding that ensures lateral and transverse confinement of the optical mode. Fig. 2.5 shows the 2D mode profiles for a ZnO clad ridge waveguide LD, showing the lateral confinement of the mode for p-GaN thicknesses varying from 50 nm to 200 nm in the top cladding layer. The distance between the bottom of the ridge waveguide and the top of the active region is fixed at 100 nm for all three structures, so the ridge depth decreases as the p-GaN thickness decreases. For p-GaN thicknesses of less than 100 nm, the optical mode has poor lateral confinement due to the shallow etched ridge waveguide and Γ decreases significantly. This is observed through the mode contours extending

CHAPTER 2: ZINC OXIDE TOP CLADDING PLANAR SUBSTRATE LASER DESIGN

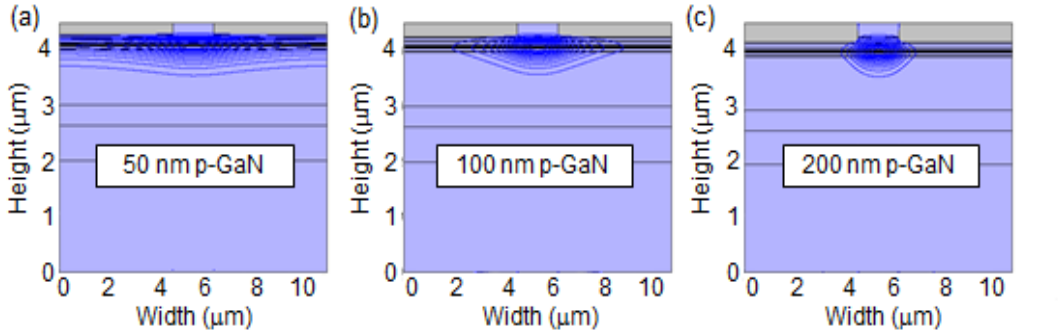

Figure 2.5 2D mode profiles for varying p-GaN thicknesses in the top cladding (a) 50 nm, (b) 100 nm and (c) 200 nm.

throughout the active region width as well as reaching the edge of the simulation window, as shown in Fig. 2.5(a). Such mode contours render numerical results unreliable and indicate the lack of a well confined mode.

Γ does not depend on the TCO composition, which is expected as ZnO and ITO have almost identical refractive indices in the blue and green regions of the spectrum. For p-GaN thicknesses of greater than 500 nm, the ZnO and ITO cladding layers have a negligible effect on the optical mode and Γ and α_i show little dependence on p-GaN thickness. This happens because the mode overlap with the TCO progressively decreases as the p-GaN thickness increases.

For p-GaN thicknesses between 100 and 500 nm, for both ITO and ZnO top claddings, Γ increases as the p-GaN thickness decreases because the peak intensity of the optical mode is increasing near the QWs as the mode is compressed by the thinner p-GaN. In this p-GaN thickness range, for the device with ITO cladding, α_i

increases as the p-GaN thickness decreases, while for the device with ZnO cladding, α_i does not increase as the p-GaN thickness decreases. The mode overlap with the TCO layer is the same for a given p-GaN thickness. The loss contribution due to the mode overlap with the TCO is higher for ITO than ZnO because of the absorption coefficients used in the modeling, which were 2000 cm^{-1} for ITO and 100 cm^{-1} for ZnO. This reduction in α_i is a key advantage of replacing ITO with ZnO in a TCO clad design.

To further investigate the difference in the loss contribution of the two different TCOs as a function of decreasing p-GaN thickness, we evaluated the layer specific losses of the structure from Table 2.3 for a 150 nm layer of p-GaN in the top cladding, keeping all the other layer thicknesses and compositions the same. The modeling results, shown in Table 2.4, show that the TCO layer specific confinement factor increases to 0.15%. The layer specific confinement factor of the TCO for 325 nm of p-GaN in the top cladding, shown in Table 3.2 was 0.02 %. This means that the mode sees more of the TCO as the p-GaN layer thickness decreases in the top cladding. The simulation results in Tables 2.3 and 2.4 indicate that the observed difference in the loss contribution of ITO and ZnO for p-GaN thicknesses between 100 nm and 500 nm is dictated by the mode overlap with the

Layer	Material	Thickness (nm)	Doping (cm^{-3})	Layer specific confinement factor (%)	Layer specific loss (cm^{-1})	Percentage of total loss (%)
TCO	ZnO	780	-	0.15	0.15	**1.19**
p^+ contact	GaN	11	3.74E+20	0.11	0.59	**4.68**
p^+ cladding	GaN	85	1.72E+19	3.60	0.94	**7.42**
p cladding	GaN	53.1	9.61E+18	7.33	1.03	**8.13**
p^- cladding	GaN	0.9	7.69E+18	0.18	0.02	0.17
p-waveguide	$In_{0.08}Ga_{0.92}N$	30	1.00E+19	7.36	1.32	**10.50**
p-EBL	$Al_{0.21}Ga_{0.79}N$	10	3.76E+19	2.36	1.16	**9.18**
QB 4	GaN	8.8	-	2.61	0.00	0.00
QW 3	$In_{0.2}Ga_{0.8}N$	4.8	2.45E+19	1.64	1.80	**14.28**
QB3	GaN	7.6	-	2.47	0.00	0.00
QW 2	$In_{0.2}Ga_{0.8}N$	4.8	2.45E+19	1.78	1.96	**15.54**
QB2	GaN	7.6	-	2.66	0.00	0.00
QW 1	$In_{0.2}Ga_{0.8}N$	4.8	2.45E+19	1.90	2.09	**16.59**
QB1	GaN	8.8	-	3.30	0.00	0.00
n-waveguide	$In_{0.08}Ga0_{.92}N$	70	2.92E+18	27.64	0.83	**6.57**
n-buffer	GaN	18	1.20E+18	5.26	0.11	0.83
n-cladding	GaN	378	1.20E+18	29.51	0.59	4.68
n-contact	GaN	630	2.24E+18	1.01	0.03	0.24
substrate	GaN	2000	-	0.00	0.00	0.00

Table 2.4. LD layer sequence used to evaluate the mode overlap with the TCO layer for a 150 nm thick p-GaN layer in the top cladding. The TCO layer specific confinement factor increases as the p-GaN thickness decreases. This increased mode overlap with the TCO coupled with ITO's much higher absorption loss account for the different behaviors observed from ITO and ZnO for p-GaN thicknesses between 100 nm and 500 nm in Fig. 2.4 (b). Even for a reduced p-GaN thickness, most of the contribution to the overall internal mode loss comes from the quantum wells, the electron blocking layer and p-cladding.

should be reflected for the full p-GaN thickness range modeled in Fig. 2.4(b). Fig. 2.6 examines the transverse mode profile and mode overlap with the TCO for p-GaN thicknesses of 50 nm, 100 nm, 350 nm and 700 nm. Correlating with Fig. 2.5(a), the mode intensity for 50 nm of p-GaN in the top cladding is very low for both TCOs. As the p-GaN thickness increases, the ridge waveguide height increases and the mode intensity increases as the mode has improved lateral confinement, correlating to Figs. 2.5(b)-(c). As the p-GaN thickness increases to 700 nm, the mode overlap with the TCO is minimal and the type of TCO has negligible effect on the internal mode loss, which correlates with the loss behavior observed in Fig. 2.4(b).

The higher contribution of ITO to the overall device internal mode loss can then be attributed to the higher ITO absorption coefficient (2000 cm^{-1}) if the mode profile is unaffected by the type of TCO. In Fig. 2.7 we evaluated the full width half max (FWHM) of the transverse mode profile for p-GaN thicknesses of 100 nm, 350 nm and 700 nm for 250 nm of TCO in the top cladding. As can be seen in Fig. 2.7(b), the FWHM is independent of the TCO composition, meaning that the mode profile is independent of the type of TCO in the top cladding. Furthermore, the FWHM decreases with decreasing p-GaN thickness for p-GaN thicknesses between 100 nm and 400 nm, as the mode is compressed by the thinner p-GaN.

CHAPTER 2: ZINC OXIDE TOP CLADDING PLANAR SUBSTRATE LASER DESIGN

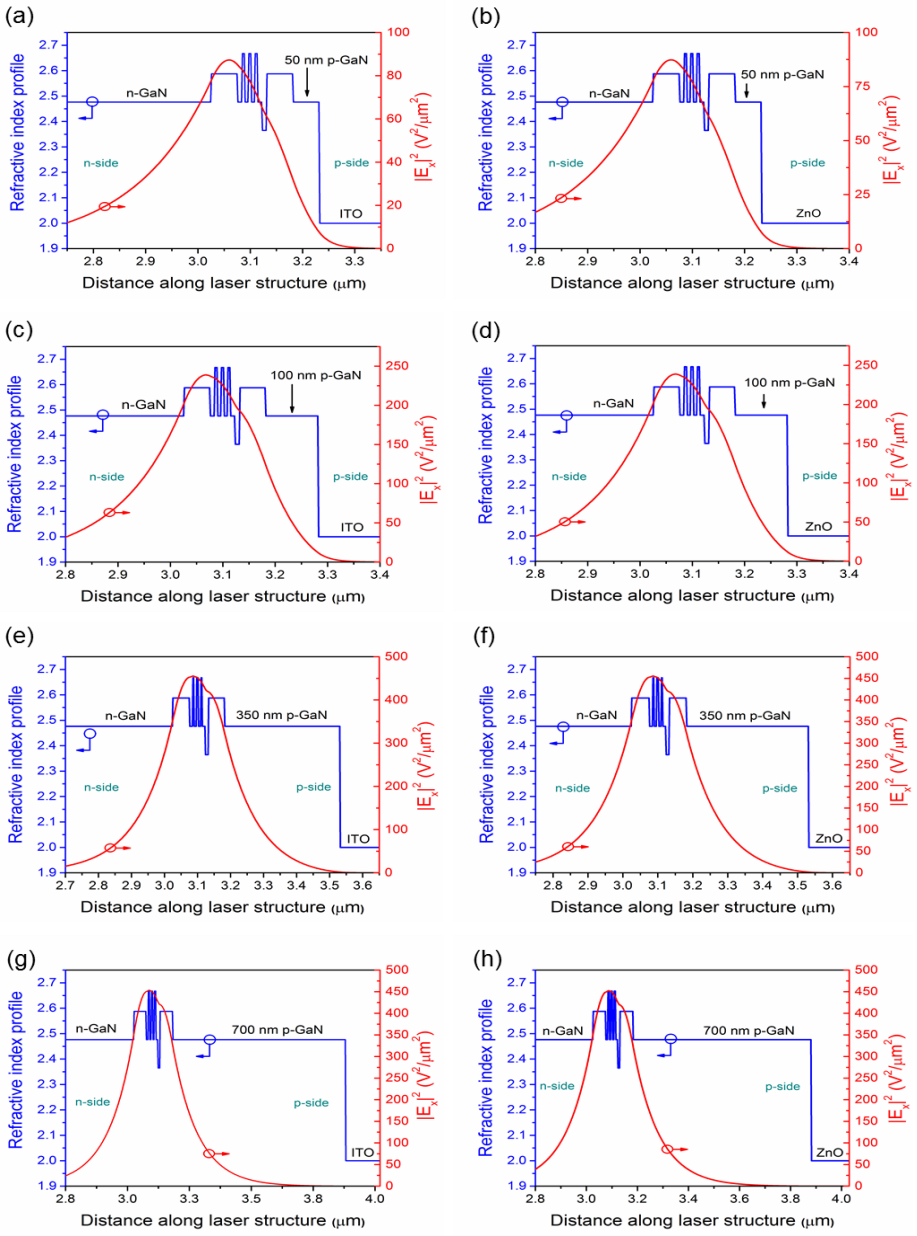

Figure 2.6 Transverse mode profile and refractive index as a function of distance in the growth direction, showing mode overlap with the TCO for 50 nm of p-GaN and 250 nm of (a) ITO and (b) ZnO; for 100 nm of p-GaN and 250 nm of (c) ITO and (d) ZnO; for 350 nm of p-GaN and 250 nm of (e) ITO and (f) ZnO; for 700 nm of p-GaN and 250 nm of (g) ITO and (h) ZnO in the top cladding.

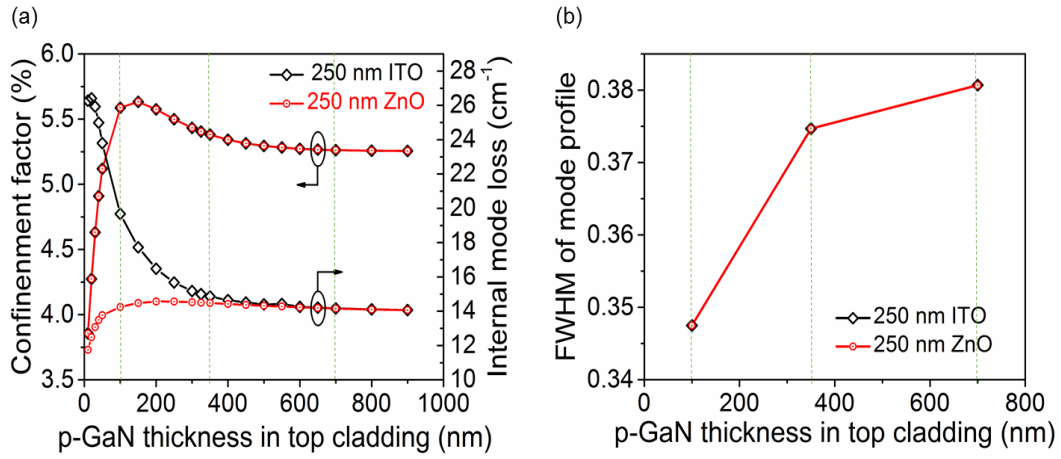

Figure 2.7 (a) Confinement factor and internal mode loss dependence on p-GaN thickness in the top cladding plotted simultaneously to show the p-GaN thicknesses for which the full width half max (FWHM) of the transverse mode profile was evaluated. (b) FWHM of the transverse mode profile dependence on p-GaN thickness, evaluated for ITO and ZnO. The FWHM is independent of the type of TCO.

This corresponds to the p-GaN thickness range for which the choice of TCO has the bigger impact on α_i in Fig. 2.2(b), reaffirming that the ZnO results in lower internal mode loss than ITO for the same confinement factor. Thus, considering that the mode overlap with the TCO layer is the same for ITO and ZnO, and that the ITO absorption coefficient used for these FIMMWAVE calculations is 20 times higher than that of ZnO, the loss for the device with ITO will be higher than the loss of the device with ZnO for p-GaN thicknesses between 100 nm and 500 nm in the top cladding.

The dependence of g_{th} and η_d on p-GaN thickness and TCO composition are shown in Figs. 2.8(a) and 2.8(b), respectively. Since α_i doesn't depend on the thickness of ZnO, only the results for 250 nm of ZnO are included in this figure. For these

calculations, the cavity length and the mean mirror reflection coefficient (R)[49] were assumed to be 1200 μm and 0.18, respectively, corresponding to a mirror loss, α_m, of 14.3 cm^{-1}. For p-GaN thicknesses of greater than 500 nm, the ZnO and ITO cladding layers have a negligible effect on the optical mode, so g_{th} and η_d show little dependence on p-GaN thickness and are equal for both TCOs.

For p-GaN thicknesses between 100 and 500 nm, for the device with ITO cladding, g_{th} increases slightly and η_d decreases significantly as the p-GaN thickness decreases because Γ increases slightly and α_i increases significantly with decreasing p-GaN thickness. In contrast, for the device with ZnO cladding, g_{th} decreases slightly and η_d decreases slightly as the p-GaN thickness decreases because Γ increases slightly and α_i does not increase with decreasing p-GaN thickness. This behavior holds for different ZnO thicknesses because α_i is

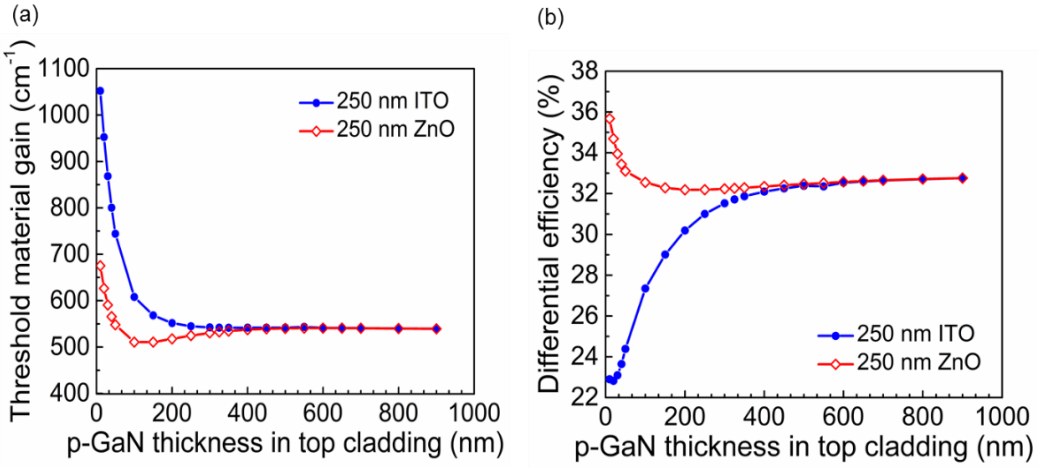

Figure 2.8 Dependence of (a) threshold material gain and (b) differential efficiency on p-GaN thickness for a structure with 250 nm of ITO or ZnO in the top cladding.

independent of ZnO thickness, as shown in Fig. 2.2 (b). The effects of the cladding layer TCO material on η_d is particularly marked and should be even more apparent for lower loss LD designs.

The use of a TCO in the top cladding creates an asymmetrical waveguide.[4] As discussed earlier, as the p-GaN gets thinner the modal overlap with the TCO increases and the peak of the mode shifts towards the n-side. The placement of the QWs in the InGaN waveguide therefore affects the confinement factor and the internal mode loss of the device. We investigated the tradeoff between Γ and α_i for a fixed p-GaN thickness and a fixed total InGaN waveguide thickness by rastering the position of the QWs in the InGaN WG from the n-side to the p-side in 10 nm increments. The simulated LD structure had a 630 nm Si-doped GaN template, a 380 nm n-GaN cladding layer, a 100 nm thick $In_{0.08}Ga_{0.92}N$ waveguide, an active region consisting of three 4.8nm $In_{0.2}Ga_{0.8}N$ QWs and four 7.6 nm GaN quantum barriers (QBs), a 10 nm $Al_{0.21}Ga_{0.79}N$ EBL, a 325 nm p-GaN layer, a 10 nm p^+ GaN contact layer and 250 nm of ZnO. The transverse mode profile and refractive index for each QW placement was plotted as a function of the distance along the laser structure, in the growth direction. The confinement factor and internal mode loss were plotted as a function of the n-waveguide thickness. The results are shown in Figs. 2.9 through 2.11.

CHAPTER 2: ZINC OXIDE TOP CLADDING PLANAR SUBSTRATE LASER DESIGN

FIMMWAVE simulations showed that for a fixed p-GaN thickness the Γ and α_i decrease as the fraction of the $In_{0.08}Ga_{0.92}N$ waveguide on the n-side increases. This happens due to the reduced overlap of the mode with the QWs, the EBL and the p-GaN layers, all of which have relatively high absorption. The transverse mode profile graphs in Fig. 2.9 (a)-(c), Fig. 2.10 (a)-(c) and Fig. 2.11 (a)-(c) show how the mode peak moves to the n-side as the n-waveguide thickness increases, thus reducing the mode overlap with the high absorption layers mentioned above.

Placing the QWs symmetrically in the waveguiding layer (i.e. 50/50 nm n-/p- $In_{0.08}Ga_{0.92}N$ WG) results in the highest optical confinement, but also results in a relatively high internal loss. However, as a higher fraction of the InGaN waveguiding layer is placed on the n-side, internal loss decreases more rapidly than optical confinement. Therefore, Γ can be minimally sacrificed to achieve much lower α_i. The design chosen for the laser demonstration that is discussed in Chapter 2.5 was a 70/30 nm n-/p-$In_{0.08}Ga_{0.92}N$ WG, which had 3% lower Γ and 12 % lower α_i, compared to the 50/50 nm n-/p-$In_{0.08}Ga_{0.92}N$ WG.

The dependence of the confinement factor and internal mode loss on the fraction of the InGaN waveguiding layer that is placed on the n-side is similar for a laser structure that has an ITO layer in the top cladding. Fig. 2.12 highlights the

CHAPTER 2: ZINC OXIDE TOP CLADDING PLANAR SUBSTRATE LASER DESIGN

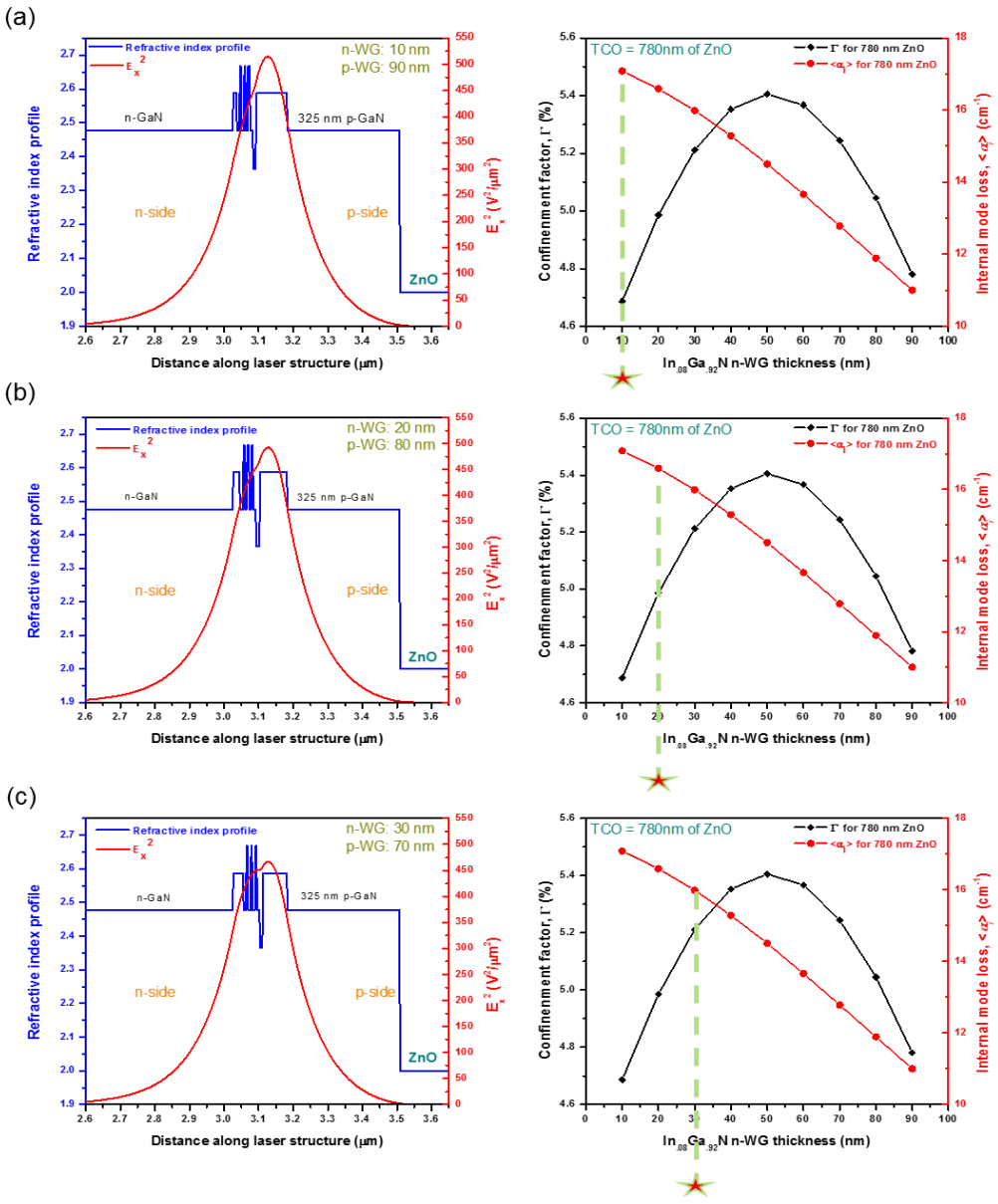

Figure 2.9 Transverse mode profile and refractive index as a function of distance in the growth direction and confinement factor and internal mode loss as a function of n-waveguide thickness for n-waveguide thicknesses of (a) 10 nm, (b) 20 nm and (c) 30 nm. The dotted green lines highlight the changing confinement factor and internal mode loss values as the mode overlap with the active region changes. The LD top cladding consisted of 325 nm of p-GaN and 250 nm of ZnO.

CHAPTER 2: ZINC OXIDE TOP CLADDING PLANAR SUBSTRATE LASER DESIGN

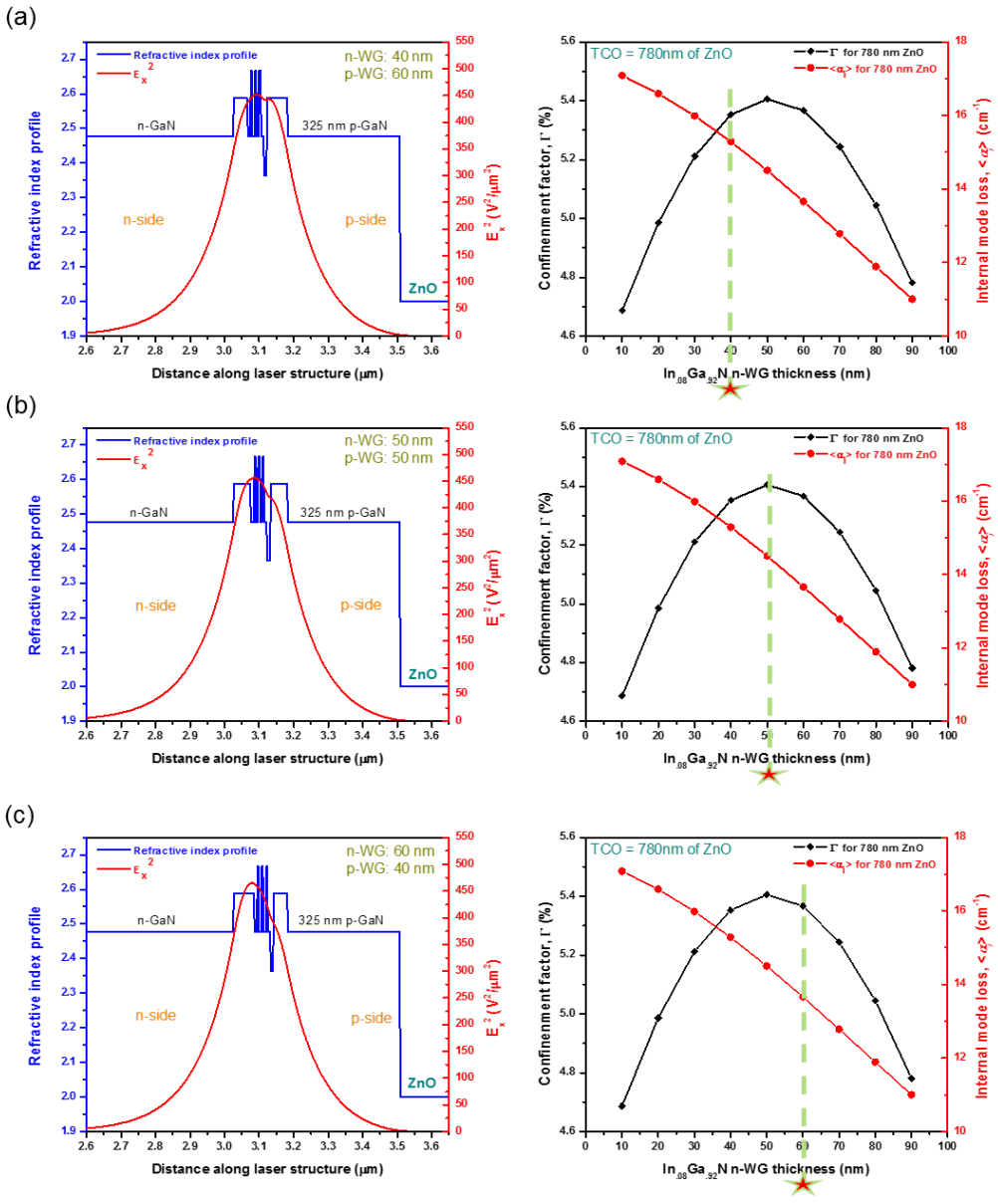

Figure 2.10 Transverse mode profile and refractive index as a function of distance in the growth direction and confinement factor and internal mode loss as a function of n-waveguide thickness for n-waveguide thicknesses of (a) 40 nm, (b) 50 nm and (c) 60 nm. The dotted green lines highlight the changing confinement factor and internal mode loss values as the mode overlap with the active region changes. The LD top cladding consisted of 325 nm of p-GaN and 250 nm of ZnO.

CHAPTER 2: ZINC OXIDE TOP CLADDING PLANAR SUBSTRATE LASER DESIGN

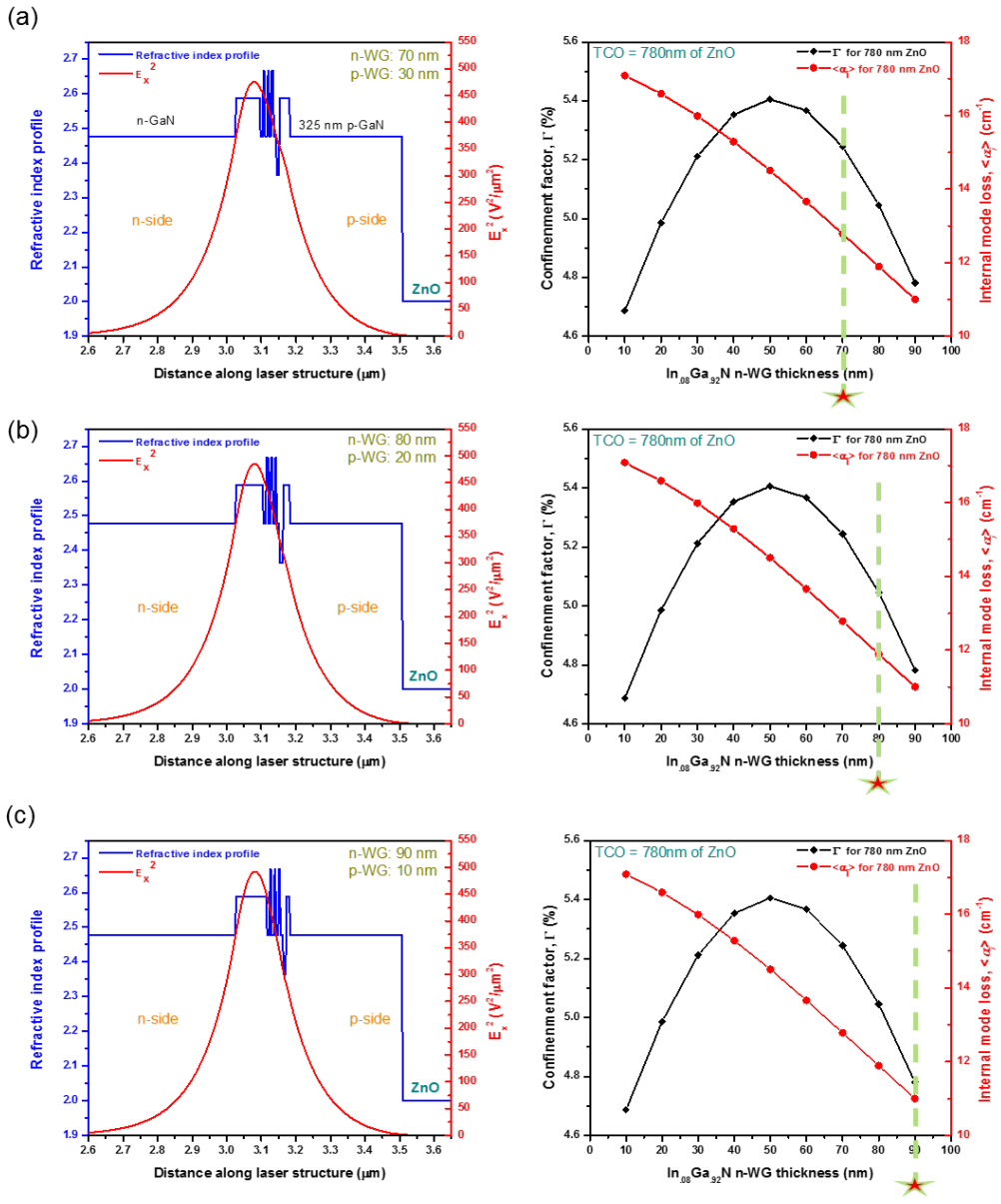

Figure 2.11 Transverse mode profile and refractive index as a function of distance in the growth direction and confinement factor and internal mode loss as a function of n-waveguide thickness for n-waveguide thicknesses of (a) 70 nm, (b) 80 nm and (c) 90 nm. The dotted green lines highlight the changing confinement factor and internal mode loss values as the mode overlap with the active region changes. The LD top cladding consisted of 325 nm of p-GaN and 250 nm of ZnO.

CHAPTER 2: ZINC OXIDE TOP CLADDING PLANAR SUBSTRATE LASER DESIGN

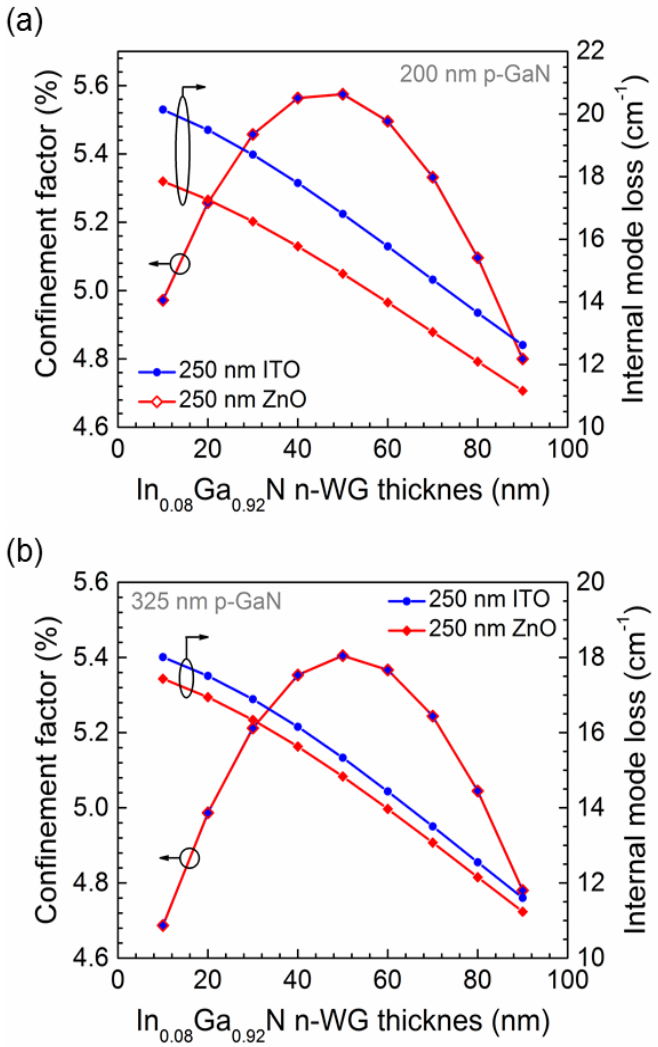

Figure 2.12 Confinement factor and internal mode loss as a function of n-waveguide thickness comparing ITO and ZnO top cladding for (a) 200 nm and (b) 325 nm of p-GaN in the top cladding. ZnO results in lower internal mode loss than ITO for all n-waveguide thicknesses for both p-GaN thicknesses considered.

effects of increasing p-GaN thickness from 200 nm to 325 nm and replacing ITO with ZnO in the top cladding for a laser structure like the one detailed in pages 28 – 29. As expected, the confinement factor is independent of the TCO material

in the top cladding for all n-WG thicknesses. It is important to note, that as suggested by the dependence of α_i on p-GaN thickness in Fig. 2.4, the reduction in α_i that results by replacing ITO with ZnO in a TCO clad design is higher for thinner p-GaN. The device with ITO top cladding has on average an α_i value of 11.4 % and 3.2 % higher than the device with ZnO top cladding for 200 nm and 325 nm of p-GaN thickness in the top cladding, respectively, for the all n-WG thickness permutations. These simulations were done for just two p-GaN thickness; a full set of simulations for p-GaN thicknesses between 100 nm to 500 nm and for different InGaN waveguide thicknesses and In compositions will give more insight on how to achieve high optical confinement with low internal mode loss.

2.4 Device Processing

The polished facet (PF) laser process developed by Hsu *et. al.*[50] was used to fabricate all three TCO top clad semipolar laser designs reported in Chapters 2-4 of this thesis. The currents chapter discusses the development of planar substrate TCO clad semipolar LDs, and I will refer to the adapted PF process used to fabricate these devices as the planar-TCO PF process, hereafter. The aforementioned original PF process provides better quality facets then the etched facet (EF) process,[51] and higher yield than the cleaved facet (CF) process,[52] which have been used for semipolar GaN-based lasers.

CHAPTER 2: ZINC OXIDE TOP CLADDING PLANAR SUBSTRATE LASER DESIGN

The EF process facets are formed using a reactive ion etch (RIE) that results in different angles for the *c*+ and *c*- facets due to surface polarity effects. EF facet inclinations can be > 5°, which results in low mirror reflectivity and quality.[51] The CF process has also proven unsuitable for semipolar GaN lasers because the large energy cost associated with forming new *c*-plane surfaces results in cracked and generally poor surface morphology LD facets.[52] Contrarily, the PF process LD facet angle is 2-3° for both facets as the facet inclination angle depends on the way the LD chip is mounted for polishing.[50] The atomic force microscope (AFM) RMS roughness of PF mirrors is ~ 5 nm, which results in higher reflectivity facets and improved mirror quality for semipolar edge-emitting laser designs.[50] The PF process has a higher yield than the CF process and the improved TCO PF process has comparable yield to the EF process.

The planar-TCO PF process traveler is based on the PF process detailed in Appendix A.3 of Reference 52. Our LD samples are electrically and optically screened using an In dot quick test prior to any processing, therefore the preliminary step is In dot removal and solvent cleaning of the sample. In is removed using a standard aqua regia acid etch, consisting of a 1:3 HNO_3:HCl mixture. Following the aqua regia clean, the samples are reactivated at 600 °C to drive out any H that may have gotten incorporated in the p-GaN during the acid clean. The p-GaN reactivation is followed by a thorough solvent clean consisting of 3 min Acetone, Isopropanol and DI water dips.

CHAPTER 2: ZINC OXIDE TOP CLADDING PLANAR SUBSTRATE LASER DESIGN

The planar-TCO PF LDs were fabricated using a self-aligned ridge waveguide process, which provides higher confinement factor than broad area laser due to the index contrast between the semiconductor and the insulating sidewall dielectric. The lithography mask set for this process consisted of varying widths (1.6, 1.8, 2.0, 4.0 and 8.0 μm) and varying lengths (600 μm, 900 μm and 1200 μm). The main process steps are detailed in Fig. 2.13. The lithography used to define the laser mesas serves also as a mask for the dielectric liftoff. As depicted in Fig. 2.13(a), it consists of ~250 nm of non-photosensitive photoresist (PR) to provide the dielectric liftoff undercut (LOL 2000) and ~1.8 μm of positive resist (SPR 955 CM-1.8) for mesa definition. The ridge waveguides were defined using a BCl_3/Cl_2 reactive ion etch, which stops 100 nm above the QWs. Following the waveguide etch. 250 nm of SiO_2 was deposited via sputtering for electrical isolation, as shown in Fig. 2.13 (c). The SiO_2 on top of the ridges was then lifted off to expose the top surface of the laser stripes for the deposition of ZnO, shown in Fig. 2.13 (d).

Following the SiO_2 liftoff, the samples were cleaned in two-step process to remove organic and oxide residue- thorough cleaning of the sample is critical to high quality aqueous solution deposition of ZnO. The organic residue was removed with a 10 min RCA standard clean (1:1:5 $NH_4OH:H_2O_2$) solution heated to 80 ^oC, which leaves an oxide residue.[53] The oxide residue was removed with a 10 min etch in a 1:1 $HCl:H_2O$ solution. A 780 nm thick undoped ZnO layer was then

CHAPTER 2: ZINC OXIDE TOP CLADDING PLANAR SUBSTRATE LASER DESIGN

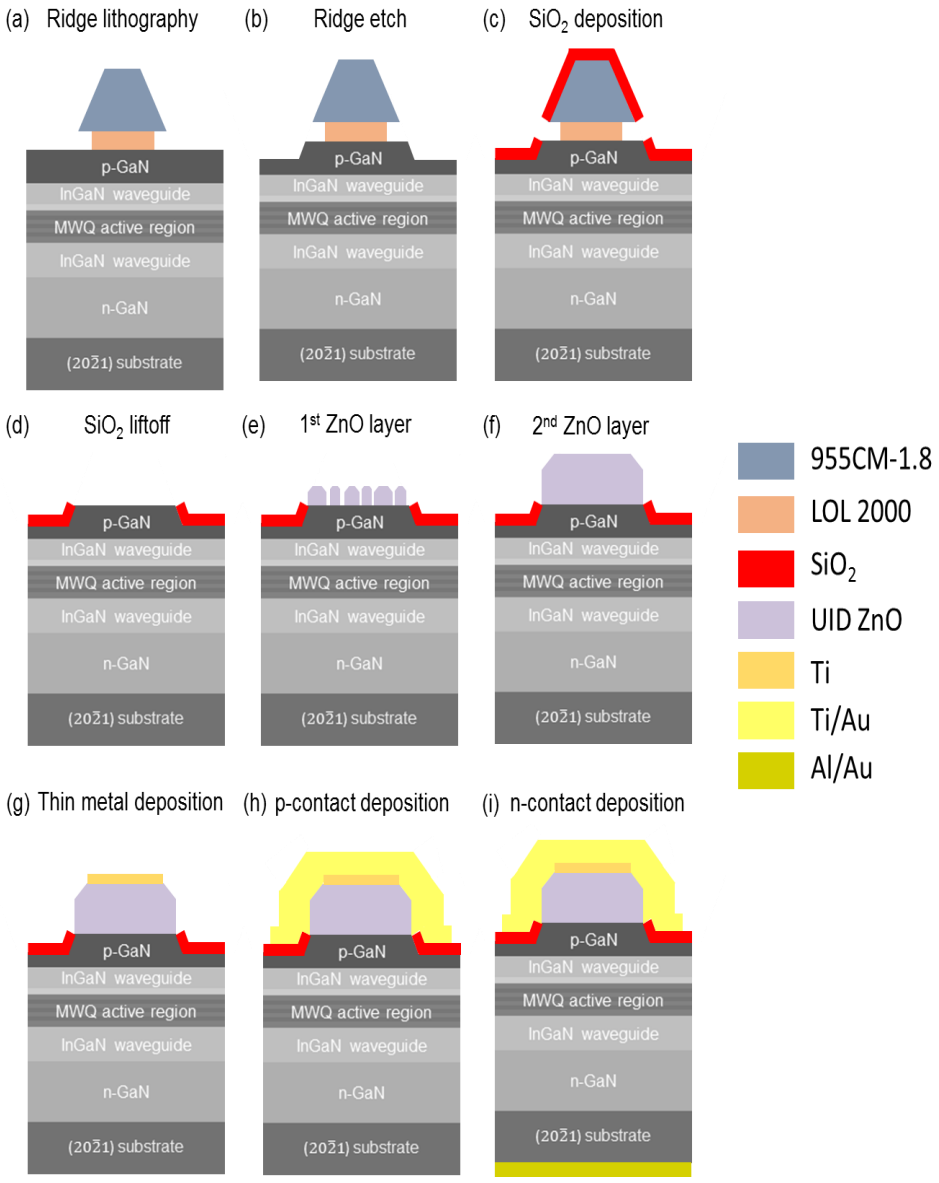

Figure 2.13 Step by step fabrication sequence for the TCO PF process, showing an individual ridge's profile for (a) ridge lithography, (b) RIE ridge etch, (c) sputter deposition of dielectric, (d) dielectric liftoff, exposing top of the ridge for TCO deposition, (e) aqueous deposition of ZnO seed layer, (f) aqueous deposition of fully coalesced ZnO second layer, (g) thin metal deposition, (h) p-contact pad deposition and (i) n-contact deposition after dicing and polishing of the laser chip.

deposited on the exposed p-GaN surface using low temperature aqueous solution deposition, the details of which are discussed in Chapter 2.2.1 The first ZnO layer consisted of a 200 nm thick, partially coalesced ZnO seed layer. The seed layer growth was catalyzed at 90 ^{o}C by adding ammonium hydroxide (NH_4OH) to a zinc nitrate hexa-hydrate ($Zn(NO_3)_2{:}6H_2O$) and ammonium nitrate (NH_4NO_3) solution. To ensure good electrical contact and adhesion, the fully-coalesced ZnO layer was deposited using a 90 ^{o}C solution of zinc nitrate hexa- then annealed at 500 ^{o}C in N_2 for 15 minutes in a rapid thermal anneal (RTA) system. A second 580 nm thick, hydroxide ($Zn(NO_3)_2{:}6H_2O$), trisodium citrate ($NaC_6H_5O_7$) and ammonium hydrate (NH_4OH).

The small sample chip size and face-down sample alignment during hydrothermal deposition ensured uniform ZnO solution concentrations over the deposition area. Fig. 2.14 (a)-(b) show optical micrographs of how aqueously deposited ZnO only grows on the exposed GaN on top of the LD mesas. Further investigations by scanning electron microscopy (SEM) showed that although there is no deposition of ZnO on the SiO_2 covered field, there are ZnO residue particles that remain on the dielectric, as can be seen in Fig. 2.14 (c)-(d). The amount of residue is related to how well the LD sample is cleaned prior to the ZnO aqueous deposition.

After the ZnO deposition, 30 nm of Ti was deposited by electron beam

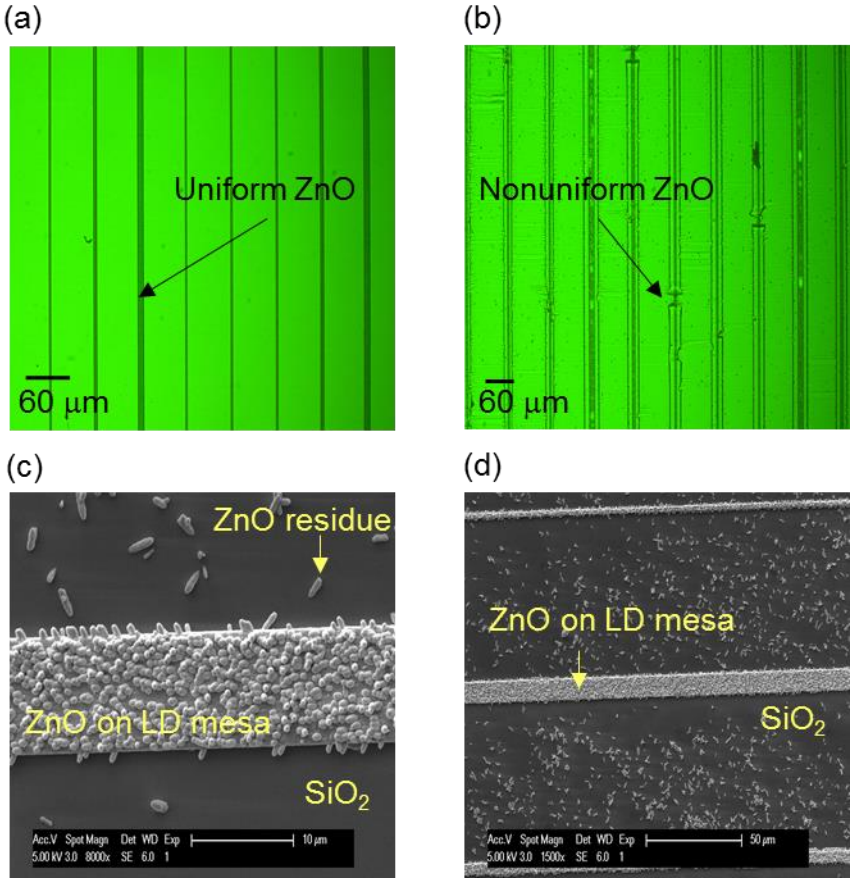

Figure 2.14 Hydrothermally grown ZnO grows preferentially on exposed p-GaN. Optical microscope images show (a) uniform ZnO ridge coverage and (b) discontinued ZnO ridge coverage due to possible air bubbles in the growth solution or surface impurities. SEM images of the (c) seed ZnO layer and (d) second ZnO layer show that while ZnO doesn't grow on SiO_2, there is ZnO residue and particulates that can deposit on the dielectric. The residue density can be mitigated by extensive pre-deposition cleaning and sonication.

evaporation along the entire length of the laser ridges and then 30/1000 nm Ti/Au was deposited also by electron beam evaporation to form a 60 μm wide p-contact pad, as shown in Fig. 2.13 (g)-(h). The thin Ti layer extended beyond the p-contact pad lengthwise on the LD ridges to ensure uniform current injection. The thin Ti layer also serves to avoid the metal peeling off the ZnO during the polishing

of the facets. The thin metal lithography uses negative resist (AZ n-LOF 2020) while the p-contact pad lithography uses a thick bilayer resist (OCG 825/SPR 955 CM-1.8) to enable clean liftoff of ~1 μm of metal. One key development of the TCO PF process is the elimination of the HCl acid cleaning step between the thin metal lithography and metal deposition. HCl attacks TCOs, especially ZnO, and strips them off the LD mesas, therefore the UV ozone is the only cleaning step for this lithography, meant to remove any organic contamination prior to electron beam metal evaporation.[54]

The LD sample was then diced to form laser bars with a cavity length of 600 μm, 900 μm and 1200 μm. The dicing sequence was another improvement on the baseline PF process. The original PF process yield was limited by the dicing step because several ridge p-contacts would get chipped and damaged by the dicing

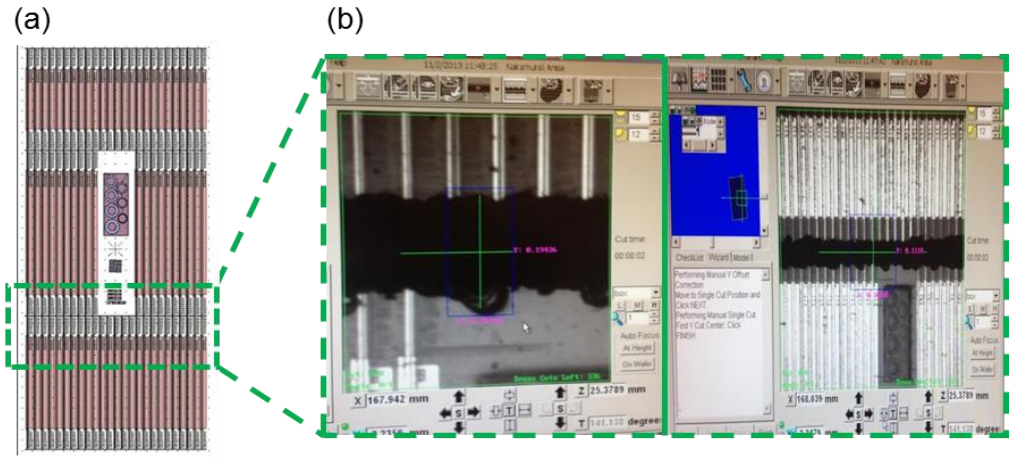

Figure 2.15 (a) The dicing via of the polished facet mask set, zoomed in in (b) to show how the two-cut dicing sequence reduces dicing damage to the LD ridges and their respective p-metal pads. The two-cute sequence results in a dicing gap that is ~ 200 μm wide.

blade due to the narrow dicing via (a little over 350 μm wide via). Without changing the mask's dicing via dimensions and without changing the ADT Dicing Saw's dicing blade cut and spindle speed, we reduced dicing damage by introducing a double-cut dicing sequence. Using a diamond coated 2.187-4C-30RU-3 blade, the first cut was made 150 μm deep with a cut speed of 3mm/sec and spindle speed of 35 kRPM. The second cut used the same blade and settings and cut all the way through the sample and tape. This two-cut dicing method increased the overall device yield of the planar-TCO PF process. As can be seen in Fig. 2.15, the cut gap resulting from the double-cut dicing was on average ~150 μm and ~200 μm at the most chipped regions. most chipped regions. This is a marked improvement over the original single-cut dicing sequence which resulted in cut gaps as wide as 350 μm.

An Allied High Tech MultiPrep 8" system and 3M polishing films were used for polishing the laser facets. The planar-TCO PF process incorporated a different sample mounting setup than the original PF process. As can be seen in Fig. 2.16 (a)-(b), the diced sample is mounted at the edge of a cross-sectional chuck. The parallelity of the sample's edge with respect to the chuck's edge affects the facet's inclination angle, LD ridge yield and overall mirror quality. In the PF process, the LD sample was sandwiched between two glass slides, but in the planar-TCO PF process, the sample was corralled with double side polished (DSP)

sapphire (Al_2O_3) pieces using hot crystal wax. Instead of placing the sapphire piece underneath the LD sample, it was placed behind the sample, as seen in Fig. 2.16 (a). This allowed better leverage and maneuverability while aligning the sample to the chuck's edge. The edges of the top sapphire corral are rough from scribing. To eliminate the debris that results while first polishing the sapphire, the top corral overhangs the LD sample edge. The polishing direction also affects the amount of debris that can be accumulated between the sample and the top corral. In the counter-clockwise (CCW) polishing direction, the polishing film hits the top of the ridges of the sample first and any polished material is removed away from the LD-corral interface. In the clockwise (CW) direction, the polishing film hits the

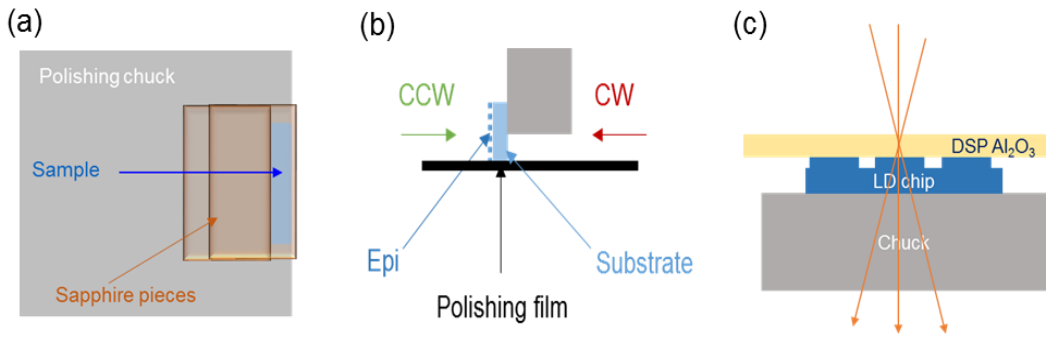

Figure 2.16 (a) Top view of the facet polish setup, showing the LD bar corralled by DSP sapphire and aligned parallel to the edge of the polishing chuck. (b) side view of the chuck position during polishing. The platen rotation, CW or CCW determines which side of the LD bar the polishing film sees first and well as the direction of polishing residue removal. (c) side view of the corralled LD chip, mounted for polishing. The arrows indicate how polishing residue is removed away from the LD chip-DSP corral interface. The CCW rotation facilitates lower residue buildup at on the polishing surface.

Polishing film grit size (μm)	Polishing film material	Polish depth (μm)	Polishing time
6.0	Diamond	40	As needed
3.0	Diamond	18	As needed
1.0	Diamond	9	As needed
0.3	Diamond	2	2 min
0.1	Diamond	2	2 min
0.05	Al_2O_3	2	2 min
0.02	Al_2O_3	2	4 min

Table 2 .5 Polishing sequence detailing the grit size grade, polishing film material, and polishing depth and time per grit size. The polish depth is measured with respect to the edge of the thin Ti contact layer on the LD ridges and is annotated on the PF mask set to monitor the polishing depth during polishing. The transparency of the top DSP sapphire corral and wax bond used to mount the sample allow for continuous monitoring of the polishing depth.

sample substrate first and polished material is removed towards the LD-corral interface, which facilitates debris accumulation on the ridges or on the facet during polishing. Such additional debris can damage the LD facet or delaminate the TCO and/or the p-contact metal. This is undesired, so for the laser device discussed in Chapter 2.5, the CCW polishing direction, shown in Fig. 2.16 (b)-(c), was used. Each facet was polished using diamond polishing films, with film grit size graded from 6.0 μm to 0.1 μm. Facet polishing was completed using 0.05 μm alumina and 0.02 μm silica polishing films. Table 2.6 lists all the polishing films' material, grit size and polishing parameters. All polishing was done at 60 RPM with a spindle load of 5-6. If the final polish is closer than ~20 μm from the thin metal edge on the ridge, the p-metal and TCO can get damaged or delaminated. The parallelity of

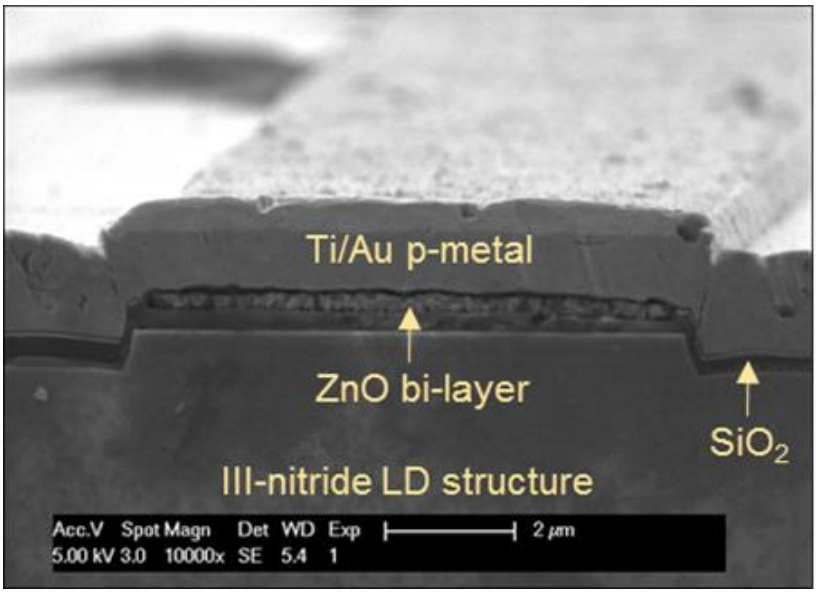

Figure 2.17 SEM side view of the polished facet of a planar $(20\bar{2}1)$ LD with ZnO top cladding. The hydrothermally deposited bilayer ZnO, the p-contact and dielectric are clearly visible. There are no striations or polishing-induced scratches on the ridge facet, indicating good polishing quality. The whole facet is also in focus, which indicates acceptable alignment parallelity of the laser bar to the edge of the polishing chuck.

the sample's alignment to the chuck greatly affects the polish depth uniformity across the length of the sample's facets. The laser fabrication was completed with the deposition of a 50/300 nm Al/Au common back side contact via electron beam evaporation, illustrated in Fig. 2.13(i). Fig. 2.17 shows an SEM image of the facet of a fully processed laser, where the epitaxial layers, SiO_2, ZnO bilayer and p-contact pad are clearly visible. This is a good example of facet that doesn't suffer any TCO or p-contact delamination.

2.5 Device results

The laser device discussed in this section was grown on a free standing $(20\bar{2}1)$ semipolar GaN substrate provided by Mitsubishi Corporation using atmospheric pressure metalorganic chemical vapor deposition (MOCVD). The LD structure had a 630 nm Si-doped GaN template, a 380nm n-GaN cladding layer, a 70 nm thick n-$In_{0.08}Ga_{0.92}N$ WG, an active region consisting of three 4.8 nm $In_{0.2}Ga_{0.8}N$ QWs and four 7.6 nm GaN QBs, a 30 nm thick p- $In_{0.08}Ga_{0.92}N$ WG, a 10 nm $Al_{0.21}Ga_{0.79}N$ EBL, a 325 nm p-GaN layer, and a 10 nm p+ GaN contact layer. The WG design chosen for this work, which was a 70/30 nm n-/p-$In_{0.08}Ga_{0.92}N$ WG, had 3% lower Γ and 12 % lower α_i, compared to the 50/50 nm n-/p-$In_{0.08}Ga_{0.92}N$ WG. The simulated optical mode profile of the LD is shown in Fig. 2.18(a) and corresponded to a Γ and α_i, of 5.2 % and 12.8 cm^{-1}, respectively.

Figure 2.18(b) shows the light-current-voltage (*L-I-V*) characteristic for a 1.6 μm wide by 1200 μm long blue LD. The current dependent spectra, which exhibit a peak wavelength of 453 nm above threshold, are depicted in Fig. 2.18(c), while Fig. 2.18(d) shows the far field pattern above threshold. The device was tested under pulsed electrical injection with a pulse width of 1.0 μs and a duty cycle of 1%. Lasing was achieved at a threshold current (I_{th}) of 166 mA, a threshold current density (J_{th}) of 8.6 kA/cm^2 and threshold voltage (V_{th}) of 10.3 V. The differential resistance (R_d) was 9 Ω at currents greater than 166 mA. The single

facet slope efficiency (η_{sl}) was 0.37 W/A which corresponds to a single facet η_d of 13.5%. Assuming equal power output from both facets, the experimental η_d for both facets was 27%.

The experimental η_d value is lower than the 32% η_d predicted by optical modeling for this p-GaN thickness. We partly attribute the lower experimental η_d to interface scattering loss,[55] contributed by the roughness of the interface between p-GaN and the ZnO seed layer. The ZnO seed layer doesn't fully coalesce so there are gaps at this interface, whose average size was estimated to be ~ 33 nm from SEM analysis. Improvements in the aqueous solution chemistry are expected to increase the coalescence of the ZnO seed layer and thus reduce interface scattering loss contributions.

CTLM analysis of ZnO on p-GaN (data courtesy of Asad Mughal) resulted in a specific contact resistivity, ρ_c, value of 0.0066 Ω/cm^2 for hydrothermally deposited UID ZnO. At the threshold current of the LD whose *L-I-V* is shown in Fig. 2.18, this ρ_c indicates that the ZnO layer contributes ~1.52 V to the LD operating voltage. The threshold voltage of 10.3 V of our laser is 1.4 V higher than the threshold voltage of a similar structure planar $(20\bar{2}1)$ LD with had ITO top

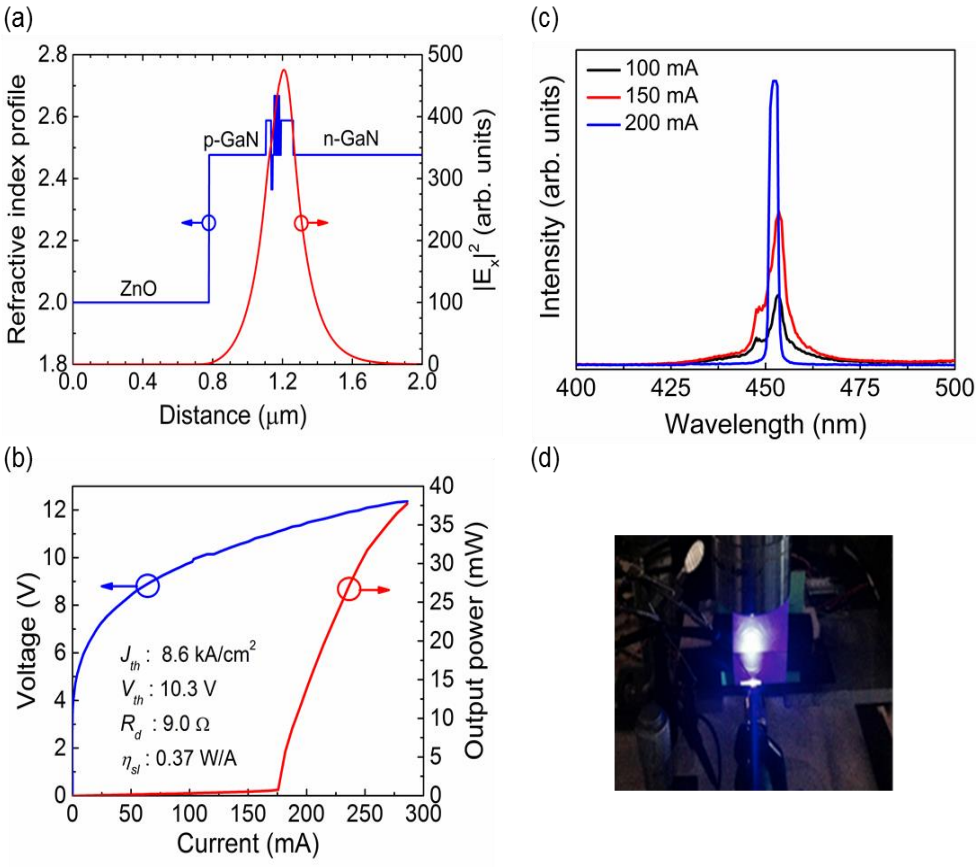

Figure 2.18 (a) Transverse mode profile and refractive index as a function of distance in the growth direction. (b) Pulsed *L-I-V* characteristics. (c) current dependent spectra and (d) the far field pattern

cladding.[4] This comparison suggests that some of the extra voltage in our ZnO top clad device is due to the electrical properties of ZnO. Therefore, further optimizations hydrothermal deposition solution chemistry and annealing conditions should be done to reduce the ZnO ρ_c. of a 1.6 μm wide by 1200 μm long LD. Introducing dopants and optimizing their concentrations during ZnO hydrothermal deposition could improve the electrical properties of ZnO and lower its contribution

to the overall device operating voltage.[18] Compared to the same similar planar substrate LD structure with ITO top cladding mentioned above,[4] this ZnO top clad laser showed a marked improvement in single facet slope efficiency and optical power output power. This result in agreement with the optical modeling prediction that a planar substrate LD with ZnO top cladding would have lower internal mode loss and higher differential efficiency compared to a planar substrate LD with ITO top cladding.

3.6 Summary

In summary, we have investigated replacing ITO with ZnO as TCO is the the top cladding layer in planar substrate, semipolar $(20\bar{2}1)$ III-nitride LDs. Numerical modeling indicated that replacing ITO with ZnO reduces the internal loss and threshold gain and increases the differential efficiency for a transparent conducting oxide clad LD design due to the relatively low optical absorption in ZnO. Lasing was achieved at 453 nm with a threshold current density of 8.6 kA/cm^2 and a threshold voltage of 10.3 V in a ZnO clad $(20\bar{2}1)$ III-nitride LD. This was the first demonstration of using ZnO as a top cladding layer and further optimizations of the ZnO quality are expected to result in improved LD performance.

Bibliography

[1] T. Minami, Thin Solid Films **516**, 5822 (2008).

[2] H. Zervos, *The Market for Touch Screens and ITO Replacement* (2012).

[3] R.G. Gordon, MRS Bull. **25**, 52 (2000).

[4] M.T. Hardy, C.O. Holder, D.F. Feezell, S. Nakamura, J.S. Speck, D. a. Cohen, and S.P. DenBaars, Appl. Phys. Lett. **103**, 81103 (2013).

[5] A.H. Reading, J.J. Richardson, C.-C. Pan, S. Nakamura, and S.P. DenBaars, Opt. Express **20**, A13 (2012).

[6] L. Meng and M.. dos Santos, Thin Solid Films **322**, 56 (1998).

[7] J.-H. Lee, J. Electroceramics **23**, 554 (2008).

[8] A. Mang, K. Reimann, and S. Rübenacke, Solid State Commun. **94**, 251 (1995).

[9] A.H. Reading, Aqueous Synthesis of Zinc Oxide Films for GaN Optoelectronic Devices, University of California Santa Barbara, 2014.

[10] A. Tsukazaki, A. Ohtomo, T. Onuma, M. Ohtani, T. Makino, M. Sumiya, K. Ohtani, S.F. Chichibu, S. Fuke, Y. Segawa, H. Ohno, H. Koinuma, and M. Kawasaki, Nat. Mater. **4**, 42 (2004).

[11] D.C. Look, Mater. Sci. Eng. B Solid-State Mater. Adv. Technol. **80**, 383 (2001).

[12] D.C. Reynolds, D.C. Look, and B. Jogai, Solid State Commun. **99**, 873 (1996).

[13] A. Janotti and C.G. Van de Walle, Reports Prog. Phys. **72**, 126501 (2009).

[14] S. Shionoya and W.H. Yen, editors , *Phosphor Handbook by Phosphor Research Society* (CRC Press, Boca Raton, FL, 1997).

[15] M.C. Larciprete, D. Haertle, A. Belardini, M. Bertolotti, F. Sarto, and P. Günter, Appl. Phys. B Lasers Opt. **82**, 431 (2006).

[16] C. Tonon, C. Duvignacq, G. Teyssedre, and M. Dinguirard, J. Phys. D. Appl. Phys. **34**, 124 (2000).

[17] A.J. Mughal, S. Oh, A. Myzaferi, S. Nakamura, J.S. Speck, and S.P. Denbaars, Electron. Lett. **52**, 304 (2016).

[18] E. Kaminska, A. Piotrowska, K. Golaszewska, M. Guziewicz, R. Kruszka, A. Kudla, T. Ochalski, A. Barcz, T. Dietl, F. Matsukura, M. Sawicki, A. Wawro, M. Zielinski, J. Jasinski, and Z. Liliental-Weber, MRS Proc. **693**, (2001).

[19] J.I. Cisneros, Appl. Opt. **37**, 5262 (1998).

[20] H. Heiland, E. Mollwo, and F. Stoeckmann, Solid State Phys. **8**, 191 (1959).

[21] E. Scharowsky, Zeitschrift F??r Phys. **135**, 318 (1953).

[22] D.C. Reynolds, C.W. Litton, D.C. Look, J.E. Hoelscher, B. Claflin, T.C. Collins, J. Nause, and B. Nemeth, J. Appl. Phys. **95**, 4802 (2004).

[23] J. Nause and B. Nemeth, Semicond. Sci. Technol. **20**, S45 (2005).

[24] T. Ben-Yaacov, T. Ive, C.G. Van de Walle, U.K. Mishra, J.S. Speck, and S.P. Denbaars, J. Electron. Mater. **39**, 608 (2010).

[25] T. Ive, T. Ben-Yaacov, A. Murai, H. Asamizu, C.G. Van De Walle, U. Mishra, S.P. DenBaars, and J.S. Speck, Phys. Status Solidi Curr. Top. Solid State Phys. **5**, 3091 (2008).

[26] C. Neumann, S. Lautenschl??ger, S. Graubner, J. Sann, N. Volbers, B.K. Meyer, J. Bl??sing, A. Krost, F. Bertram, and J. Christen, Phys. Status Solidi Basic Res. **244**, 1451 (2007).

[27] H. Ju Ko, Y. Chen, S. Ku Hong, and T. Yao, J. Cryst. Growth **209**, 816 (2000).

[28] K. Tamura, K. Nakahara, M. Sakai, D. Nakagawa, N. Ito, M. Sonobe, H. Takasu, H. Tampo, P. Fons, K. Matsubara, K. Iwata, A. Yamada, and S. Niki, Phys. Status Solidi C Conf. **1**, 2704 (2004).

[29] E. Arca, K. Fleischer, and I. V. Shvets, Appl. Phys. Lett. **99**, 15 (2011).

[30] X.A. Cao, S.J. Pearton, A.P. Zhang, G.T. Dang, F. Ren, R.J. Shul, L. Zhang, R. Hickman, and J.M. Van Hove, Appl. Phys. Lett. **75**, 2569 (1999).

[31] Y. Igasaki and H. Saito, Thin Solid Films **199**, 223 (1991).

[32] S.W. Shin, S.M. Pawar, T.-W. Kim, J.-H. Moon, and J.H. Kim, J. Mater.

Res. **24**, 441 (2009).

[33] D.C. Agarwal, R.S. Chauhan, A. Kumar, D. Kabiraj, F. Singh, S.A. Khan, D.K. Avasthi, J.C. Pivin, M. Kumar, J. Ghatak, and P. V. Satyam, J. Appl. Phys. **99**, (2006).

[34] D.J. Rogers, F.H. Teherani, C. Sartel, V. Sallet, F. Jomard, P. Galtier, and M. Razeghi, Zinc Oxide Mater. Devices Iv **7217**, SPIE (2009).

[35] J.R. Bellingham and W. a. Phillips, J. Mater. Sci. Lett. **11**, 263 (1992).

[36] T. Tynell and M. Karppinen, Thin Solid Films **551**, 23 (2014).

[37] R.A. Laudise and A.A. Ballman, J. Phys. Chem. **64**, 688 (1960).

[38] J.H. Kim, E.M. Kim, D. Andeen, D. Thomson, S.P. DenBaars, and F.F. Lange, Adv. Funct. Mater. **17**, 463 (2007).

[39] H.Q. Le, S.K. Lim, G.K.L. Goh, S.J. Chua, and J. Ong, J. Electrochem. Soc. **157**, H796 (2010).

[40] D. Andeen, L. Loeffler, N. Padture, and F.F. Lange, J. Cryst. Growth **259**, 103 (2003).

[41] D. Andeen, J.H. Kim, F.F. Lange, G.K.L. Goh, and S. Tripathy, Adv. Funct. Mater. **16**, 799 (2006).

[42] J.J. Richardson and F.F. Lange, Cryst. Growth Des. **9**, 2576 (2009).

[43] J.J. Richardson and F.F. Lange, Cryst. Growth Des. **9**, 2570 (2009).

[44] FIMMWAVE version 5.3.2, Photon Design (2011).

[45] E. Kioupakis, P. Rinke, A. Schleife, F. Bechstedt, and C.G. Van de Walle, Phys. Rev. B **81**, 241201 (2010).

[46] R. Goldhahn, a. T. Winzer, a. Dadgar, a. Krost, O. Weidemann, and M. Eickhoff, Phys. Status Solidi Appl. Mater. Sci. **204**, 447 (2007).

[47] E. Kioupakis, P. Rinke, and C.G. Van De Walle, Appl. Phys. Express **3**, 82101 (2010).

[48] R.M. Farrell, D.A. Haeger, P.S. Hsu, K. Fujito, D.F. Feezell, S.P. Denbaars,

J.S. Speck, and S. Nakamura, Appl. Phys. Lett. **99**, 17 (2011).

[49] L.A. Coldren, S.W. Corzine, and M.L. Masanovic, *Diode Lasers and Photonic Integrated Circuits* (John Wiley & Sons, Inc., 2012).

[50] P.S. Hsu, Stress-Relaxation in III-Nitride Based Semipolar Lasers, University of California Santa Barbara, 2013.

[51] R. Farelll, UNIVERSITY of CALIFORNIA Santa Barbara Growth, Fabrication, and Characterization of Continuous-Wave AlGaN-Cladding-Free, 2010.

[52] M.T. Hardy, Stress Engineering for Semipolar ($20\bar{2}1$) Blue and Green InGaN Based Laser Diodes, 2013.

[53] W. Kern, *Handbook of Semiconductor Wafer Cleaning Technology* (Noyes Publications, 1993).

[54] J.R. Vig, J. Vac. Sci. Technol. A Vacuum, Surfaces, Film. **3**, 1027 (1985).

[55] P.K. Tien, Appl. Opt. **10**, 2395 (1971).

3

Indium tin oxide top cladding limited area epitaxy laser design

3.1 Introduction

THIS chapter introduces the limited area epitaxy (LAE) - transparent conducting oxide (TCO) laser design that resulted in the demonstration of a $(20\bar{2}1)$ laser with AlGaN bottom cladding and Sn-doped In_2O_3 (ITO) top cladding. Having demonstrated that ZnO can be used as an alternative TCO to ITO in a planar substrate semipolar $(20\bar{2}1)$ laser in Chapter 2, the next development milestone was the simultaneous incorporation of LAE-enabled

CHAPTER 3. INDIUM TIN OXIDE TOP CLADDING LIMITED AREA EXPITAXY LASER DESIGN

AlGaN bottom cladding and a TCO top cladding in a semipolar laser diode (LD). This chapter presents the LAE-TCO concept in Chapter 3.2 and its benefits are studied through optical modeling in Chapter 3.3. The fabrication process development and the device results and analysis are presented in Chapter 3.4 and 3.5, respectively, to complete the chapter. As is discussed in Chapter 3.5, incorporating ITO top cladding onto an LAE $(20\bar{2}1)$ laser structure resulted in lasing being achieved at 446 nm with a threshold current density of 8.5 kA/cm^2 and a threshold voltage of 8.4 V.

3.2 Design concept

As discussed in Chapter **1.XX**, the bottom cladding design of semipolar III-nitride laser diodes is limited by stress relaxation through misfit dislocations that form via the glide of pre-existing threading dislocations (TDs),[1,2] whereas the top cladding is limited by the growth time and temperature of the p-type layers.[3–5] These design limitations have individually been addressed by using limited area epitaxy (LAE) to block TD glide in n-type AlGaN bottom cladding layers,[6] and by using transparent conducting oxide (TCO) top cladding layers to reduce the growth time and temperature of the p-type layers.[7] In addition, a TCO-based top cladding should have significantly lower resistivity than a conventional p-type

(Al)GaN top cladding.[8] The goal of this work is the simultaneous incorporation of both these methods to demonstrate an LAE-enabled n-AlGaN bottom clad semipolar laser that has TCO top cladding. Fig. 3.1 shows the LAE-TCO semipolar laser design concept with ITO in the top cladding layer. By enabling the use of n-AlGaN in the bottom cladding, LAE makes it possible to use thinner p-GaN in the top cladding, which reduces thermal damage to the quantum wells (QWs) and the contribution from the top cladding to the overall device resistance. In addition, the design increases the index contrast in the laser waveguide, which increases the confinement factor of the lasing mode. We consider both ITO and ZnO as options for the top cladding TCO, even though ITO is depicted in Fig. 3.1. The LAE-TCO LD design facilitates numerous Al composition values in the AlGaN bottom cladding in addition to design knobs such as the InGaN waveguide

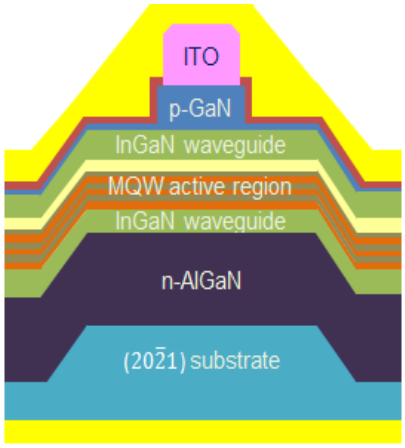

FIG. 3.1. The LAE-TCO semipolar laser design concept. The TCOs considered for this design were ITO and ZnO, with ITO shown in this figure. The yellow layer is p-AlGaN EBL layer. The layer thicknesses and compositions used for optical modeling are detailed in Table 3.1

(WG) layer asymmetry and p-GaN thickness in the top cladding. The next section will explore the semipolar LAE-TCO design space and benefits through optical modeling of the LAE-TCO LD and evaluate the benefits of replacing ITO with ZnO in the top cladding layer.

3.3 Optical modeling

The optical modeling for the LAE-TCO device builds on the optical modeling performed for the planar TCO device discussed in Chapter 2.3. Incorporating LAE-enabled n-AlGaN bottom cladding allows for thinner p-GaN in the top cladding and higher index contrast in the laser waveguide. The index contrast is affected by the AlN fraction in the AlGaN bottom cladding. Additionally, as seen in Chapter 2.3, the choice of TCO in the top cladding affects the internal mode loss (α_i) of the device. All these parameters and their effect on the confinement factor (Γ) and α_i were investigated through FIMMWAVE software simulations.[9]

Fig. 3.1 outlines the baseline laser structure used in the optical modeling with layer specific details tabulated in Table 3.1. The modeled device layer sequence consisted of a $(20\bar{2}1)$ free-standing GaN substrate, a Si_2H_6-doped GaN template, followed by an n-cladding comprised of an AlGaN/GaN modulation-

doped short period superlattice (SPSL), having a total thickness of ~1 μm. Following the n-cladding, the structure consisted of an InGaN n-waveguide (WG) layer, an undoped three QW active region, a p-AlGaN electron blocking layer (EBL), an InGaN p-WG, an Mg-doped GaN p-cladding and a TCO layer.

The n-AlGaN bottom cladding's overall AlN fraction is a geometric average between the AlN fraction of the AlGaN and GaN layers in the SPSL, with each layer being 2.5 nm thick for an SPSL period of 5 nm. To get an average Al composition of 5%, like the example listed in Table 3.1, the SPSL layers are $Al_{0.1}Ga_{0.9}N$ and GaN. Even with LAE, strain relaxation limits and dictates Al composition and AlGaN thickness, therefore Al composition is a parameter that merits optimization. In the FIMMWAVE simulations the AlN fraction was varied from 0-12% to see its effect on confinement factor and internal mode loss.

As detailed in Table 3.2, the AlGaN AlN fractions simulated were 1%, 3%, 5%, 6%, 8%, 10% and 12%. These values were based on the critical thickness calculations done by Young *et. al.*,[10] which showed that for our highest simulation Al composition value of 12%, the critical thickness of $Al_{0.24}Ga_{0.76}N$, which would be the AlN fraction required in the AlGaN layer of the SPSL, was over 10 nm on the $(20\bar{2}1)$ plane,[10,11] which is a thickness we expect to grow coherently with the LAE method using MOCVD. The AlGaN refractive index

Layer	Material	Thickness (nm)	Doping (cm^{-3})	Layer specific confinement factor (%)	Layer specific loss (cm^{-1})	Percentage of total loss (%)
TCO	ITO	250.0	-	0.15	2.90	**14.70**
p^+ contact	GaN	11.0	3.74E+20	0.10	0.57	2.88
p^+ cladding	GaN	120.0	1.72E+19	6.56	1.71	**8.63**
p cladding	GaN	67.2	9.61E+18	13.10	1.83	**9.28**
p^- cladding	GaN	2.0	7.69E+18	0.58	0.07	0.35
p-wavguide	$In_{0.08}Ga_{0.92}N$	50.0	1.00E+19	17.96	3.23	**16.37**
p-EBL	$Al_{0.21}Ga_{0.79}N$	9.1	3.76E+19	3.25	1.59	**8.06**
QB 4	GaN	8.8	-	3.41	0.00	0.00
QW 3	$In_{0.20}Ga_{0.80}N$	4.9	2.45E+19	2.06	2.26	**11.46**
QB 3	GaN	7.6	-	3.00	0.00	0.00
QW 2	$In_{0.20}Ga_{0.80}N$	4.9	2.45E+19	2.09	2.30	**11.65**
QB 2	GaN	7.6	-	3.02	0.00	0.00
QW 1	$In_{0.20}Ga_{0.80}N$	4.9	2.45E+19	2.09	2.30	**11.63**
QB 1	GaN	8.8	-	3.49	0.00	0.00
n-waveguide	$In_{0.08}Ga_{0.92}N$	50.0	2.92E+18	18.29	0.55	2.78
n-buffer	GaN	17.6	1.20E+18	4.49	0.09	0.45
n-cladding	$Al_{0.05}Ga_{0.95}N$	989.0	2.00E+18	17.33	0.35	1.76
n- contact	GaN	378.0	1.20E+18	0.00	0.00	0.00
n-contact	GaN	630.0	2.24E+18	0.01	0.00	0.00
substrate	GaN	2000.0	-	0.02	0.00	0.00

Table 3.1 Layer sequence example of LD used for optical modeling. The p-GaN top cladding thickness was varied from 10 nm to 900 nm; the example listed in this table has 200 nm p-GaN. The AlN mole fraction in the n-AlGaN bottom cladding was varied in the simulations with the values used being 0%, 1%, 3%, 5%, 6%, 8%, 10% and 12%. The layers with the highest individual loss contribution are highlighted in bold in the last column. For this p-GaN thickness, the quantum wells, the electron blocking layer and the p-cladding contribute significantly to the overall internal loss, accounting for ~45 %, ~10% and ~22% of the total device loss, respectively. Doping optimization is expected to mitigate these layers' loss contribution.

AlN fraction in AlGaN bottom cladding (%)	*n*
1	2.47
3	2.46
5	2.45
6	2.44
8	2.43
10	2.42
12	2.41

Table 3.2 The AlN fraction values and respective calculated refractive indices used for the LAE-enabled n-AlGaN bottom cladding in the FIMMWAVE simulations of the LAE-TCO LD design.

for each AlN fraction was calculated by taking a geometric average of the AlGaN and GaN refractive indices in the respective SPSL, using values from Goldhahn *et.al*.[12]

The layer thickness listed in Table 3.1 which were used for the FIMMWAVE modeling were also the same layer thicknesses in the demonstrated device, which will be discussed in Chapter 3.5. Like the planar-TCO LD design, the LAE-TCO design also uses an Mg-doping grade in the p-GaN layer of the top cladding. We use an increasing doping grade in the direction of growth because absorption loss increases with increased doping,[13,14] so the gradual Mg doping increase is intended to reduce the p-GaN layers' contribution to loss without compromising electrical properties. The p-GaN cladding layer is therefore tabulated as four different layers in Table 3.1.

CHAPTER 3. INDIUM TIN OXIDE TOP CLADDING LIMITED AREA EXPITAXY LASER DESIGN

The individual layer refractive indices and absorption coefficients for GaN, InGaN, and AlGaN that were used in the FIMMWAVE model were taken from Goldhahn *et. al.*[12] Both ITO and ZnO were investigated in the modeling even though the first LAE-TCO demonstration used ITO as the TCO in the top cladding. At 450 nm, which the wavelength used in the optical modeling, the refractive index of both ITO and ZnO is 2. The ITO refractive index was taken from Hardy *et. al.*[7] and the ZnO refractive index was taken from Reading *et. al.*[15] The absorption coefficient of ITO of 2000 cm^{-1} and the absorption coefficient of UID ZnO of 100 cm^{-1} were also taken from References 7 and 15, respectively.

In line with the previous modeling, the optical modeling of the LAE-TCO device assumes free carrier absorption to be the main contribution to internal loss. The absorption coefficients for the III-nitride layers were adapted from Kioupakis *et. al,*[13] using the same assumptions detailed in Chapter 2.3. Secondary ion mass spectroscopy (SIMS) measurements were used to determine the carrier concentration of the individual layer of the LD structure, excluding the QWs, whose carrier concentration was calculated from published estimates and adapted to our device's threshold conditions.[16] SIMS gives doping values per each layer and we are again assuming 100% activation for the purpose of these optical mode simulations.

FIMMWAVE calculates the confinement factor and the internal loss and

then those values are used to calculate threshold material gain (g_{th}) and differential efficiency (η_d), using Equations 2.1 and 2.2, detailed in Chapter 2.3. In this work, we assumed uncoated laser facets and an injection efficiency (η_i) value of 65%.[16] The modeling results presented here used the fundamental TE mode values calculated using the real FMM solver in FIMMWAVE.

Mirroring the investigation in Chapter 2.3, the first goal of the optical modeling was to determine how thin the p-GaN layer in the top cladding can be without infringing on the lateral confinement of the optical mode. We determined this thickness limit by evaluating the dependence of Γ and α_i on p-GaN thickness ranging from 20 nm to 550 nm, for both ITO and ZnO (TCO thickness kept fixed at 250 nm), using the LD structure shown in Fig. 3.1 and detailed in Table 3.1 as a baseline. A planar-TCO (n-GaN bottom cladding) semipolar design was included in the modeling in order to directly see how this design differed from the LAE-TCO (n-AlGaN bottom cladding) semipolar design. The n-GaN bottom cladding was simulated as a 0% AlN fraction layer in the FIMMWAVE modeling LD structure.

Fig. 3.2 shows the dependence of confinement factor on p-GaN thickness for the varying Al compositions in the n-AlGaN bottom cladding. The TCO material does not affect the confinement factor for a given Al composition value because ZnO and ITO have almost identical refractive indices in the blue and

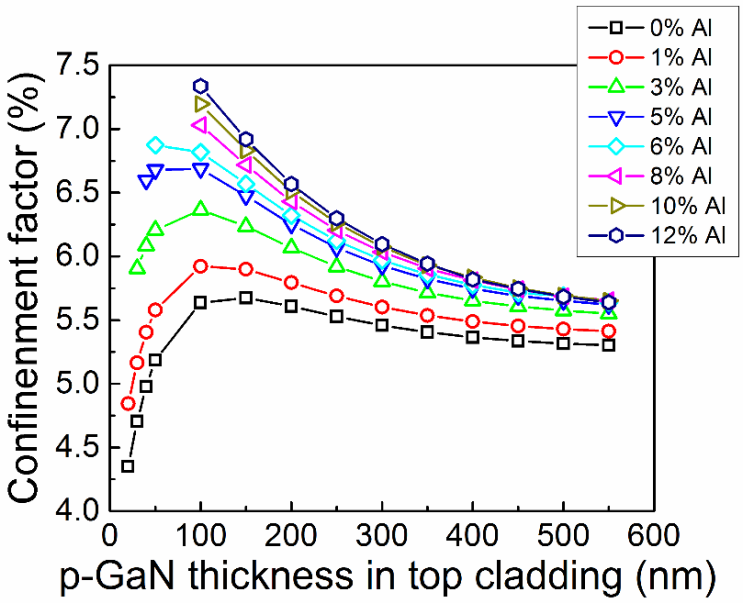

Figure 3.2 Dependence of confinement factor on p-GaN thickness in the top cladding for laser structures with various Al compositions in n-AlGaN bottom cladding. Confinement factor values are independent on the TCO choice in the blue region of the spectrum, so only the results for a device with ITO in the top cladding layer are included in this figure for clarity.

green regions of the spectrum. Only the Γ values of the ITO top clad LAE-TCO LD are shown in this figure, since the Γ values are identical for both ITO and ZnO top clad designs, for all p-GaN thicknesses and Al compositions. For all p-GaN thicknesses, the confinement factor increases with increasing Al composition in the n-AlGaN bottom cladding. This behavior is expected because as the AlGaN refractive index decreases with increasing Al composition, the index contrast of the waveguide increases, thus increasing the confinement factor.

The confinement factor increases as the p-GaN thickness in the top cladding decreases, before experiencing a sharp drop-off at a p-GaN thickness of

100 nm. This relates to the minimum p-GaN thickness in the top cladding which ensures lateral mode confinement. As the p-GaN gets thinner, the peak intensity of the optical mode has a higher spatial overlap with the QWs as well as more overlap with the high loss p-AlGaN EBL, p-InGaN WG, and p-GaN layers. Figure 3.3 shows the 2D mode profiles for device structures with $Al_{0.05}Ga_{0.95}$ bottom cladding and 50, 100 and 200 nm of p-GaN in the top cladding. The distance between the bottom of the ridge waveguide and the top of the active region is fixed at 100 nm for all three structures, so the ridge depth decreases as the p-GaN thickness decreases.

For p-GaN thicknesses of less than 100 nm, the optical mode has poor lateral confinement due to the shallow etched ridge waveguide and Γ decreases significantly, as depicted in Fig. 3.3(a). This behavior is valid for all Al compositions simulated, as can be seen in Fig. 3.2. For AlN fractions of 8% or

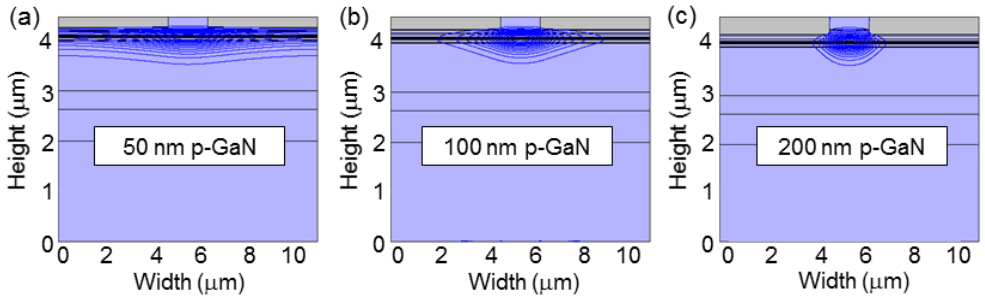

Figure 3.3 2D mode profiles showing the lateral confinement of the mode for p-GaN thicknesses of (a) 50 nm, (b) 100 nm, and (c) 200 nm in the top cladding layer for device structures with n-$Al_{0.05}Ga_{0.95}$ bottom cladding and ITO in the top cladding layer. The distance between the bottom of the ridge waveguide and the top of the active region is fixed at 100 nm for all three structures.

higher, there is no mode solution for p-GaN thickness of less than 100 nm. As the p-GaN thickness becomes greater than 100 nm, Γ increases as the lateral mode confinement initially increases, as illustrated in Fig. 3.3(c). However, as the p-GaN thickness increases, the mode profile full width half max (FWHM) increases as the mode spreads out to the thicker p-GaN. The mode shape doesn't change noticeably for p-GaN thicknesses above 450 nm, at which point Γ shows little dependence on varying p-GaN thickness.

The dependence of the internal mode loss on p-GaN thickness for the various Al compositions is shown in Fig. 3.4. Unlike its effect on the confinement factor, the choice of TCO in the top cladding layer has a pronounced effect on internal mode loss of the LAE-TCO LD design. For all AlN fractions, ZnO top

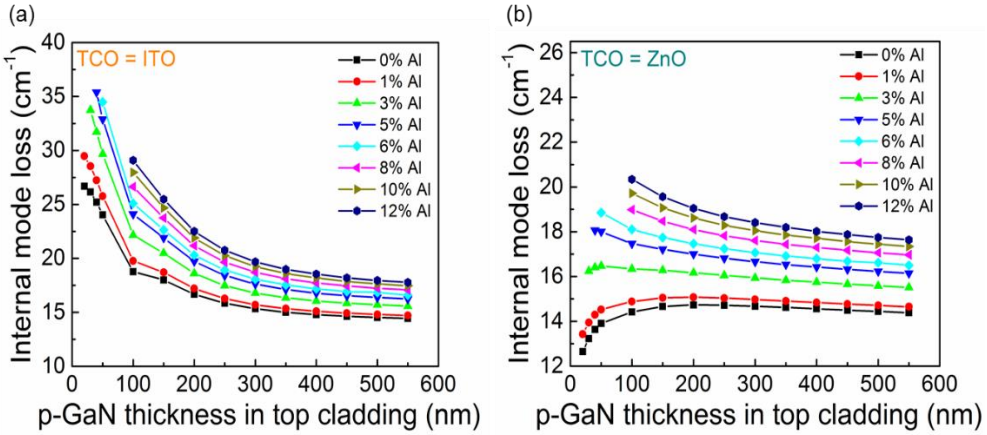

Figure 3.4 Dependence of internal mode loss on p-GaN thickness in the top cladding for laser structures with various AlN fractions in n-AlGaN bottom cladding with (a) 250 nm of ITO and (b) 250 nm of ZnO in the top cladding layer.

cladding results in lower internal mode loss values than ITO top cladding. These results are justified, considering that the absorption coefficient values used for the FIMMWAVE simulations for ZnO and ITO were 100 cm^{-1} and 2000 cm^{-1}, respectively.

The α_i dependence on p-GaN thickness for both ZnO and ITO are plotted simultaneously for all simulated Al compositions in Fig. 3.5(a). The difference between the ZnO and ITO contributions to the overall internal mode loss is most noticeable for p-GaN thicknesses between 100 nm and 300 nm. To better highlight this difference, Fig. 3.5(b) shows the internal mode loss dependence on p-GaN thickness for both TCOs only for a laser structure with $Al_{0.05}Ga_{0.95}N$

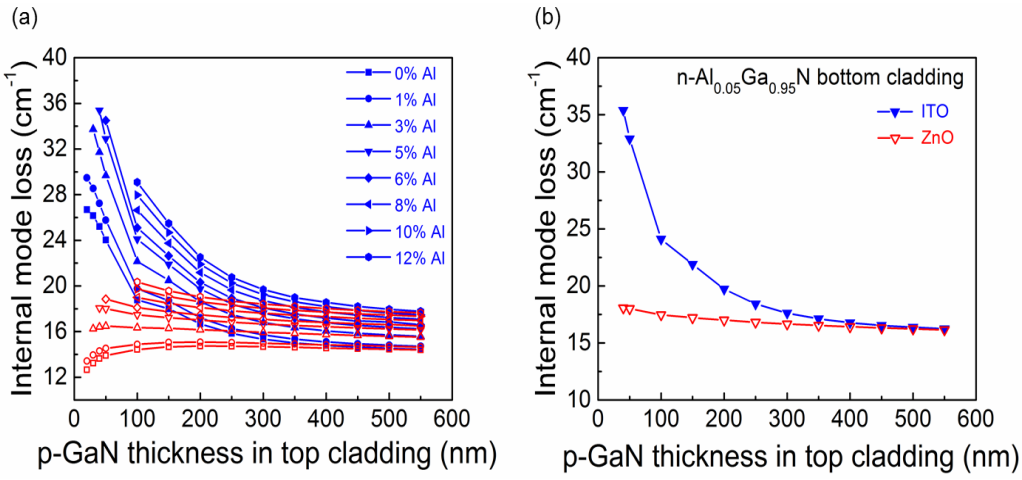

Figure 3.5 Effect of ITO and ZnO top claddings on the dependence of internal mode loss on p-GaN thickness in the top cladding for (a) laser structures with various Al compositions in n-AlGaN bottom cladding and (b) a laser structure with 5% Al composition in the bottom cladding. The filled blue symbol curves represent ITO top clad lasers while the open red symbol curves represent ZnO top clad lasers.

p-GaN thickness (nm)	ITO internal mode loss (cm^{-1})	ZnO internal mode loss (cm^{-1})	% difference
100	24.1	17.5	27.5
150	21.9	17.2	21.4
200	19.7	17.0	13.8
250	18.4	16.8	8.7
300	17.6	16.7	5.4
350	17.1	16.5	3.4
400	16.8	16.4	2.1

Table 3.3 Tabulated internal mode loss values for a laser structure with 5% Al composition in the bottom cladding comparing the effect of ZnO and ITO for various p-GaN thicknesses. The TCO thickness was fixed at 250 nm for both the ZnO and ITO top cladding variations. The rest of the simulated structure is the same as the LD tabulated in Table 31.

bottom cladding. For this Al composition in the bottom cladding, the FIMMWAVE simulations, tabulated in Table 3.3, show that for p-GaN thicknesses of 100 nm, 150 nm and 200 nm, the ITO top clad device has 27.5%, 21.4% and 13.8% higher internal mode loss than the same device has with ZnO top cladding, respectively. For p-GaN thicknesses between 100 nm and 200 nm, the difference between the effect of ZnO and ITO top cladding layers on α_i increases with increasing Al composition. But, for all Al compositions, this difference starts to decrease as the p-GaN thickness increases and becomes negligible for p-GaN thicknesses above 400 nm.

As can also be seen in Figs.3.4 and 3.5(a), in the p-GaN thickness range between 100 nm and 400 nm the internal mode loss increases for the device with ITO top cladding but is relatively unchanged for the device with ZnO top cladding. This behavior can be explained by looking at the dependence

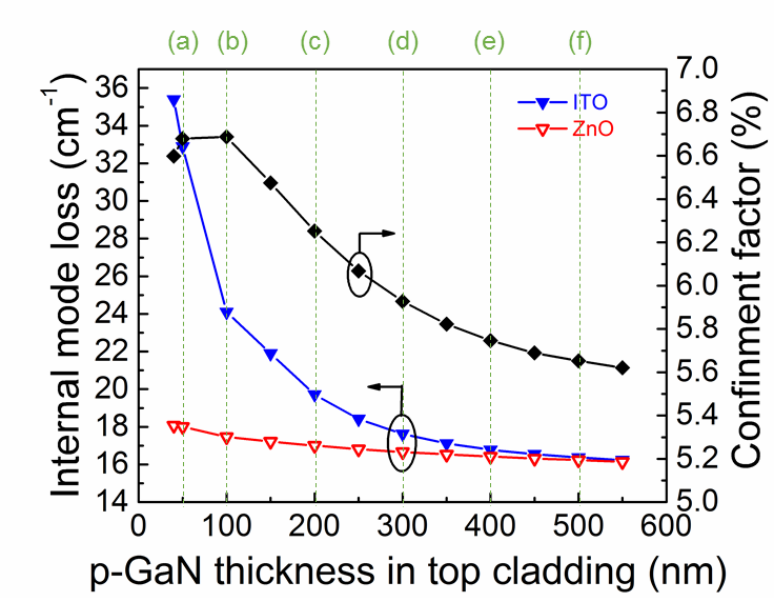

Figure 3.6 Dependence of Γ and α_i on p-GaN thickness for a laser structure with $Al_{0.05}Ga_{0.95}N$ bottom cladding, comparing 250 nm of ITO and ZnO in the top cladding. The dotted green lines denote the p-GaN thicknesses whose transverse mode profiles are plotted in Fig. 4.7(a) - (e).

of the mode overlap with the TCO on p-GaN thickness. Fig. 3.6 shows the dependence of the confinement factor and internal mode loss on p-GaN thickness and for a laser structure with $Al_{0.05}Ga_{0.95}N$ bottom cladding, while comparing 250 nm of ZnO and ITO in the top cladding. The transverse mode profiles for p-GaN thicknesses of 50 nm, 100 nm, 200 nm, 300 nm, 400 nm and 500 nm in the top cladding of this laser design are then plotted in Fig. 3.7. The plots in Fig. 3.7 include only the results for ITO top cladding because for a given p-GaN thickness, the mode profile and its overlap with the TCO layer is independent of the TCO in the blue region of the spectrum, given that the ZnO and ITO refractive

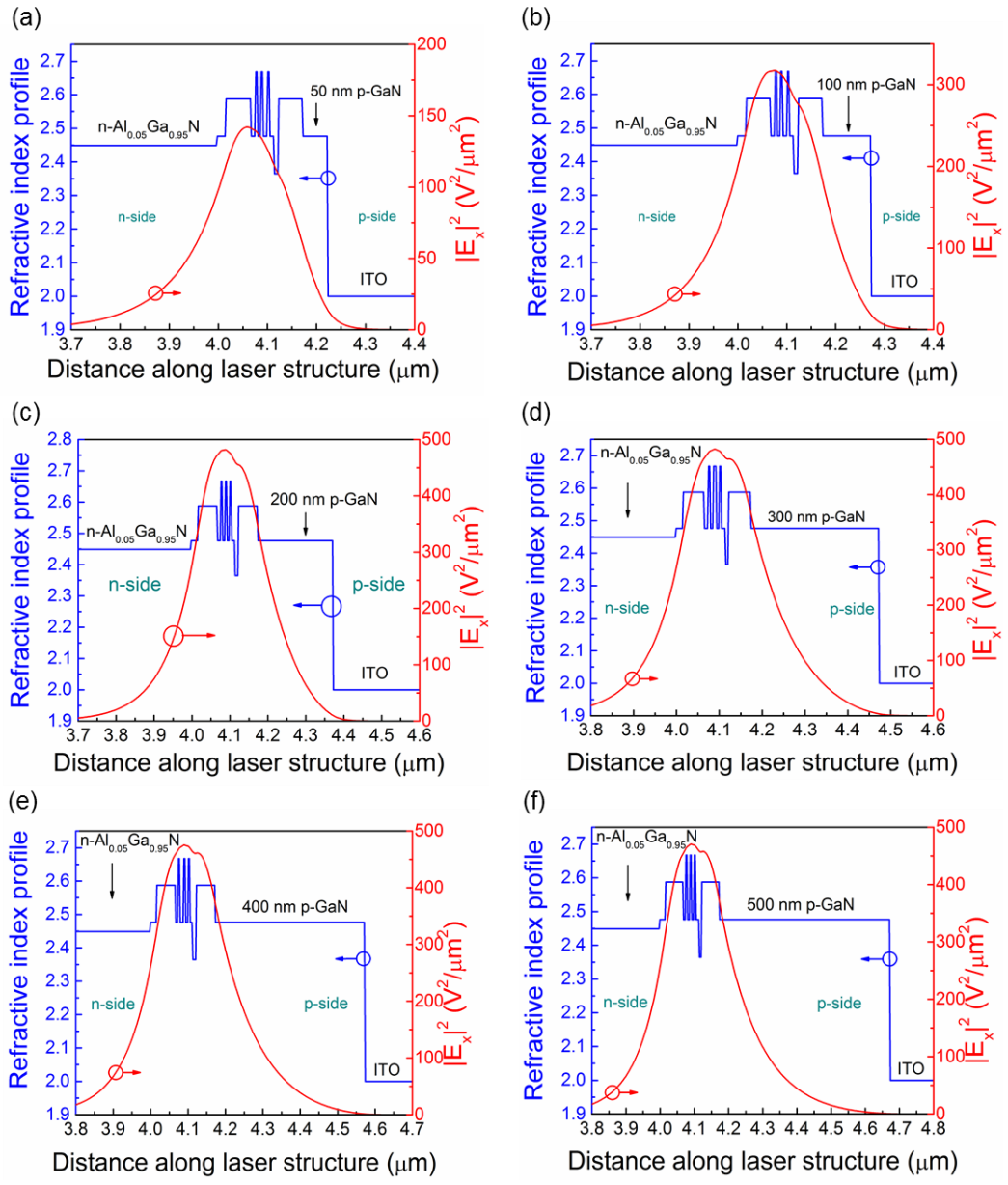

Figure 3.7 Transverse mode profile and refractive index as a function of distance in the growth direction, showing mode overlap with the TCO for 250 nm of ITO and (a) 50 nm of p-GaN (b) 100 nm of p-GaN (c) 200 nm of p-GaN (d) 300 nm of p-GaN (e) 400 nm of p-GaN and (f) 500 nm of p-GaN in the top cladding for a laser structure with n-$Al_{0.05}Ga_{0.95}N$ bottom cladding.

indices are identical for these wavelengths, resulting in the same confinement

factor for both TCO's for a given Al composition and a given p-GaN thickness. The mode intensity for 50 nm of p-GaN in the top cladding in Fig. 3.7(a) is very low as there is poor lateral mode confinement, which correlates with Fig. 3.3(a).

Recall that Figs. 3.3(b)-(c) show that the lateral mode confinement improves for p-GaN thicknesses between 100 nm and 400 nm. As the p-GaN thickness increases, the mode overlap with the TCO decreases, a behavior that holds for all Al compositions in the bottom cladding. This means that the higher contribution of ITO top cladding to the LD's internal mode loss is attributed to its assumed absorption coefficient (2000 cm^{-1}), which is much higher than that assumed of ZnO (100 cm^{-1}). As the p-GaN thickness increases beyond 400 nm, the mode overlap with the TCO is minimal and the choice of TCO has negligible effect on the internal mode loss. These results match the findings of Section 2.3

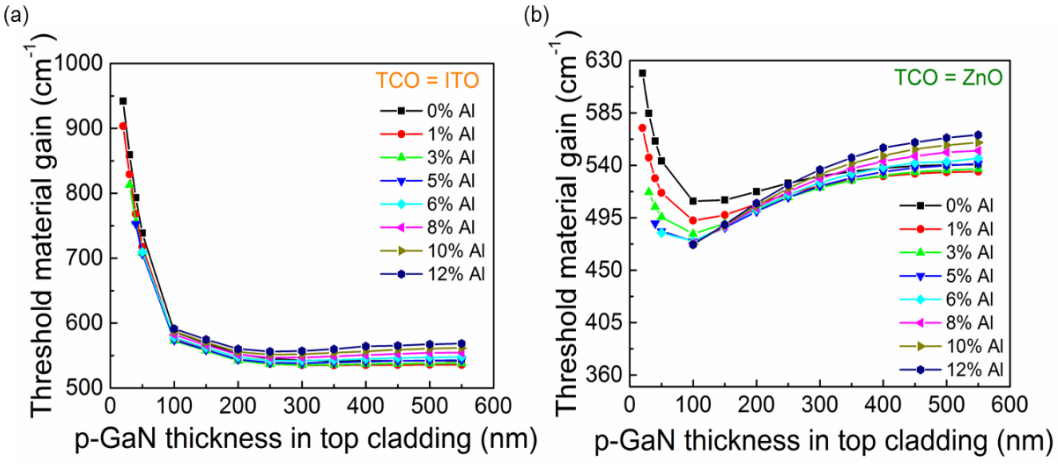

Figure 3.8 Dependence of threshold material gain on p-GaN thickness in the top cladding for laser structures with various Al compositions in the n-AlGaN bottom cladding for (a) 250 nm of ITO and (b) 250 nm of ZnO in the top cladding layer.

with regards to the difference between the contribution of the ZnO and ITO to the overall internal mode loss of a laser design for a given p-GaN thickness in the top cladding layer. The reduction in internal mode loss by replacing ITO with ZnO remains a key advantage of the LAE-TCO laser design.

The dependences of g_{th} and η_d on p-GaN thickness for both TCOs are shown in Figs. 3.8 and 3.10, respectively. For these calculations, the cavity length and mean reflection coefficient, R,[17] were assumed to be 1200 μm and 0.18, respectively, corresponding to a mirror loss of 14.3 cm^{-1}. The differences between the effects of ZnO and ITO top cladding on both g_{th} and η_d are compared for the various Al compositions in the bottom cladding and the simulation results for each parameter are tabulated for 5% Al in the bottom cladding in Tables 3.4 and 3.5, respectively.

In accordance with the Γ and α_i trends shown in Figs. 3.2 and 3.4, the mode has poor lateral confinement for p-GaN thicknesses of less than 100 nm, which means that g_{th} increases substantially for both ZnO and ITO top clad devices. Fig. 3.8(a) shows that for an ITO top clad LD, for a given Al composition in the bottom cladding, for all p-GaN thicknesses of greater than 100 nm, g_{th} exhibits little dependence on p-GaN thickness because both Γ and α_i increase with decreasing p-GaN thickness, roughly canceling the effects of one

another on g_{th}.

In slight contrast, Fig 3.8(b) shows that for a ZnO top clad LD, for p-GaN thicknesses greater than 250 nm, the threshold material gain increases for increasing Al composition in the bottom cladding. This is most prominent for Al compositions higher than 6% because the dependence of the confinement factor on p-GaN thickness for these Al compositions starts to converge for p-GaN thicknesses higher than 250 nm. Since g_{th} is inversely proportional to Γ and directly proportional to α_i and given that for each Al composition, the α_i for a device with ZnO top cladding is relatively unchanged for p-GaN thicknesses greater than 250 nm, the confinement factor has a higher impact on threshold

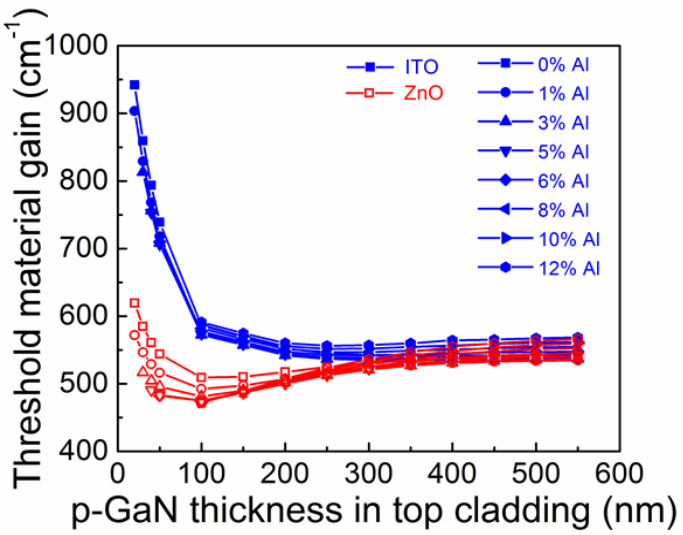

Figure 3.9 Effect of ITO and ZnO top claddings on the dependence of threshold material gain on p-GaN thickness in the top cladding for laser structures with various Al compositions in n-AlGaN bottom cladding. The filled blue symbol curves represent ITO top clad lasers while the open red symbol curves represent ZnO top clad lasers.

p-GaN thickness (nm)	ITO threshold material gain (cm^{-1})	ZnO threshold material gain (cm^{-1})	% difference
100	574.0	474.9	17.3
150	558.8	486.6	12.9
200	544.0	500.5	8.0
250	539.0	512.6	4.9
300	538.4	522.2	3.0
350	539.4	529.4	1.9
400	540.7	534.5	1.1

Table 3.4 Tabulated threshold material gain values for a laser structure with 5% Al composition in the bottom cladding comparing the effect of ZnO and ITO for various p-GaN thicknesses. The TCO thickness was fixed at 250 nm for both the ZnO and ITO top cladding variations. The rest of the simulated structure is the same as the LD structure tabulated in Table 3.1.

material gain than internal mode loss does for LAE devices with ZnO top cladding. Therefore, the tradeoff between higher Γ and higher g_{th} for increasing Al composition in the bottom cladding is important to consider when choosing the optimal p-GaN thickness for the LAE-TCO design.

The choice of TCO in the top cladding has a marked effect on threshold material gain for p-GaN thicknesses between 100 nm and 300 nm, independent of the Al composition in the bottom cladding. To better illustrate this difference, the dependence of g_{th} on p-GaN thickness for both ZnO and ITO top clad LDs was plotted for all Al compositions in the bottom cladding in Fig. 3.9. For p-GaN thicknesses between 100 nm and 300 nm, the g_{th} for the devices with ZnO top cladding is considerably lower than the g_{th} for the devices with ITO top cladding, for all Al compositions in the bottom cladding.

Table 3.4 tabulates the g_{th} dependence on p-GaN thickness for

devices with n-$Al_{0.05}Ga_{0.95}N$ bottom cladding and compares the g_{th} values for ZnO and ITO top claddings, both TCO shaving a thickness of 250 nm. For this bottom cladding Al composition, the calculated g_{th} values show that for p-GaN thicknesses of 100 nm, 150 nm, and 200 nm, the device with ITO top cladding has 17.3%, 12.9% and 8.0% higher g_{th} values than the same device would have with ZnO top cladding, respectively. Just like for the rest of the Al composition in the bottom cladding, the difference between the ZnO and ITO effect on g_{th} values starts to decreases for p-GaN thicknesses greater than 250 nm and becomes negligible for p-GaN thicknesses above 400 nm.

Fig. 3.10 shows the dependence of η_d on p-GaN thickness for the various Al compositions in the bottom cladding. η_d depends on α_i, which is highly affected by the TCO material in the top cladding, as seen in Figs. 3.4 and 3.5. As

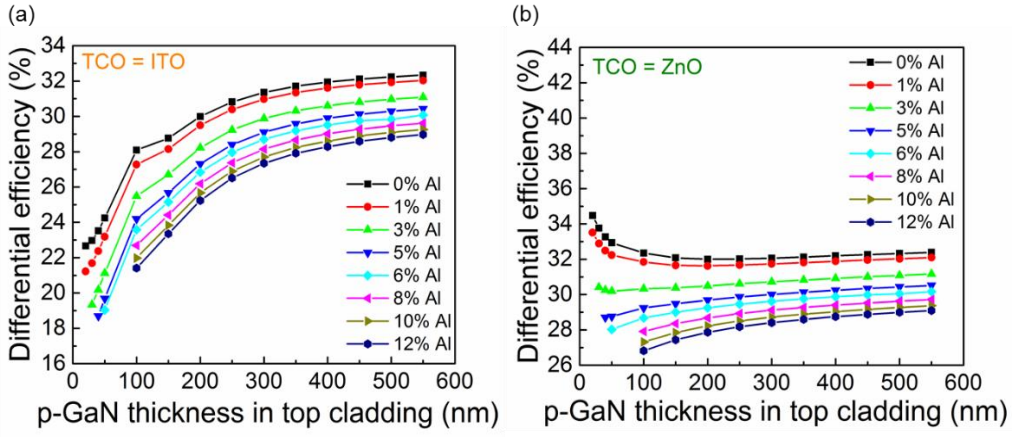

Figure 3.10 Dependence of differential efficiency on p-GaN thickness in the top cladding for laser structures with various Al compositions in the n-AlGaN bottom cladding for (a) 250 nm of ITO and (b) 250 nm of ZnO in the top cladding layer.

shown in Fig. 3.10(a), for all Al compositions in the bottom cladding, LD structures with ITO top cladding, have lower η_d than LD structures with ZnO top cladding. For p-GaN thicknesses between 100 nm and 300 nm, the η_d of ITO top clad devices decreases rapidly for decreasing p-GaN thicknesses because the α_i of ITO top clad devices increases rapidly for decreasing p-GaN thicknesses, for all n-AlGaN bottom cladding Al compositions. Contrarily, the α_i of the devices with ZnO top cladding remains relatively unchanged with decreasing p-GaN thickness, therefore the η_d values of devices with ZnO top cladding change less with decreasing p-GaN thickness, for all Al compositions in the bottom cladding.

The η_d dependence on p-GaN thickness for both ZnO and ITO are plotted simultaneously for all simulated Al compositions in Fig. 3.11(a). The difference between the ZnO and ITO top cladding effects on η_d is most prominent for p-GaN thicknesses between 100 nm and 300 nm. Fig. 3.11(b) emphasizes the benefits of replacing ITO with ZnO in the top cladding by showing the dependence of η_d on p-GaN thickness for only 5% Al in the bottom cladding.

Table 3.5 tabulates the calculated η_d values for this Al composition for both ZnO and ITO. As can be seen, for p-GaN thicknesses of 100 nm, 150 nm, 200 nm and 250 nm, the ZnO top clad device has 17.3%, 12.9%, 8.0%, and 4.9% higher differential efficiency than the ITO top clad device, respectively. For p-GaN thicknesses higher than 300 nm, for this Al composition as well as all

CHAPTER 3. INDIUM TIN OXIDE TOP CLADDING LIMITED AREA EXPITAXY LASER DESIGN

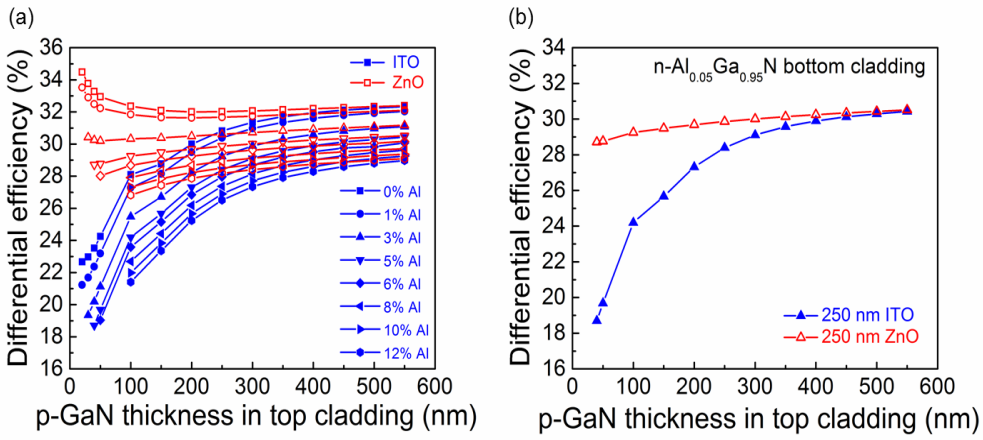

Figure 3.11 Effect of ITO and ZnO top claddings on the dependence of differential efficiency on p-GaN thickness in the top cladding for (a) laser structures with various Al compositions in n-AlGaN bottom cladding and (b) a laser structure with 5% Al composition in the bottom cladding. The blue filled symbol curves represent ITO top clad lasers while the red open symbol curves represent ZnO top clad lasers.

p-GaN thickness (nm)	ITO differential efficiency (%)	ZnO differential efficiency (%)	% difference
100	24.2	29.2	17.3
150	25.7	29.5	12.9
200	27.3	29.7	8.0
250	28.4	29.9	4.9
300	29.1	30.0	3.0
350	29.6	30.1	1.9
400	29.9	30.2	1.1

Table 3.5 Tabulated differential efficiency values for a laser structure with 5% Al composition in the bottom cladding comparing the effect of ZnO and ITO for various p-GaN thicknesses. The TCO thickness was fixed at 250 nm for both the ZnO and ITO top cladding variations. The rest of the simulated structure is the same as the LD structure tabulated in Table 3.1.

others, the ZnO and ITO cladding layers have negligible effect on α_i. Therefore, η_d shows little dependence on p-GaN thickness and is independent of the TCOs in the top cladding. Mirroring its effect on internal mode loss, the improvement of replacing ITO with ZnO in the top cladding is considerable and should have a higher impact for lasers designs that have lower internal mode loss.

3.4 Process development

The LAE-TCO semipolar lasers were fabricated through a modified polished facet (PF) process that built on the planar-TCO PF process discussed in Section 2.4, which will be referred to as LAE-TCO PF process henceforth. The merits of the PF process were discussed in Section 2.4. The LAE-TCO PF process for ITO top clad devices requires different steps than the LAE-TCO PF process for ZnO top clad devices. ITO was used in the top cladding of the first demonstrated LAE-TCO device, which will be discussed in Section 3.4, because electron beam deposition of ITO is a simpler process than the aqueous deposition of ZnO. Therefore, this section will focus on the LAE-ITO PF process. The full LAE-ITO PF process is based on Appendices A.3 and A.5 of Reference 3.

The first step of the LAE-TCO PF process for an ITO top clad semipolar LD is the pre-growth LAE patterning of the free standing $(20\bar{2}1)$ GaN substrate. The LAE patterning consists of a dry etching 1 μm deep mesas into the

substrate and an elaborate acid and solvent clean. The mesa height was optimized to block TD glide during MOCVD epitaxial growth.[3] For the lasers discussed in Chapter 3.5, the mask used to pattern the LAE mesas was Mask #2 from the PF mask set, which has 4 μm, 8μm, and 14 μm wide stripes.

The LAE stripes are patterned using a single SPR 220-3.0 photoresist (PR) mask. The mesas are etched using a BCl_3/Cl_2 reactive ion etch (RIE) and are ~1 μm deep, as mentioned above. LAE patterned samples must be rigorously cleaned to be epi-ready. To that end, designated glassware and tweezers are used for the LAE process as well as the following acid and solvent clean: the sample is first dipped in HCl for 5-6 min then it is solvent cleaned using ACE, ISO and DI while rotating at 500 RPM on a flat Teflon solvent spinner chuck. The cleanliness of the solvent spinner chuck was found to affect the quality of the MOCVD growth surface therefore a designated LAE-only solvent spinner chuck is used. The

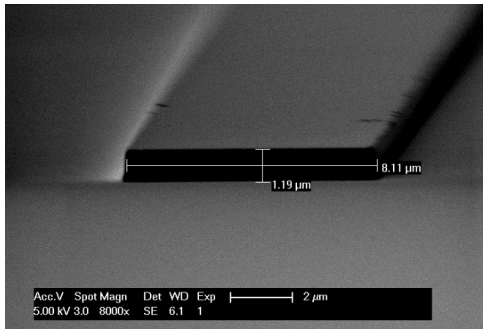

Figure 3.12 Processed LAE mesa on a $(20\bar{2}1)$ substrate prior to MOCVD device growth. The mesa shown is 8 μm wide and etched just a little over 1 μm.

sample is cleaned with each solvent for 45 seconds and DI rinsed for 1 minute. Fig. 3.12 shows an example 8 μm wide mesa from a finished LAE process on a $(20\bar{2}1)$ substrate. At this point the sample is vacuum sealed until the LAE-patterned substrate is ready to be grown on in the MOCVD reactor.

Similarly, to the TCO PF process, the LAE-ITO PF process fabricates LDs using a self-aligned ridge waveguide process. The lithography mask set for this process consisted of varying widths (1.6, 1.8, 2.0, 4.0 and 8.0 μm) and varying lengths (600, 900 and 1200 μm). The main process steps are detailed in Fig. 3.13. The first steps of this fabrication happen before the MOCVD growth of the LD structure, shown in Figs. 3.13(a)-(b). After growth and p-GaN activation, the LD fabrication continues with the ridge lithography, which was used to define the laser mesas and as a mask for the dielectric liftoff. As depicted in Fig. 3.13 (c), it consisted of ~250 nm of non-photosensitive photoresist (PR) to provide the dielectric liftoff undercut (LOL 2000) and ~1.8 μm of positive resist (SPR 955 CM-1.8) to define the LD ridges.

The ridge waveguides were defined using a BCl_3/Cl_2 reactive ion etch, which stops 100 nm above the QWs. Following the waveguide etch, 250 nm of SiO_2 was deposited via sputtering for electrical isolation, shown in Fig. 3.13 (e). The SiO_2 on top of the ridges was then lifted off to expose the top surface of the laser stripes for the blanket deposition of ITO, shown in Fig. 3.13 (f). 250 nm of

CHAPTER 3. INDIUM TIN OXIDE TOP CLADDING LIMITED AREA EXPITAXY LASER DESIGN

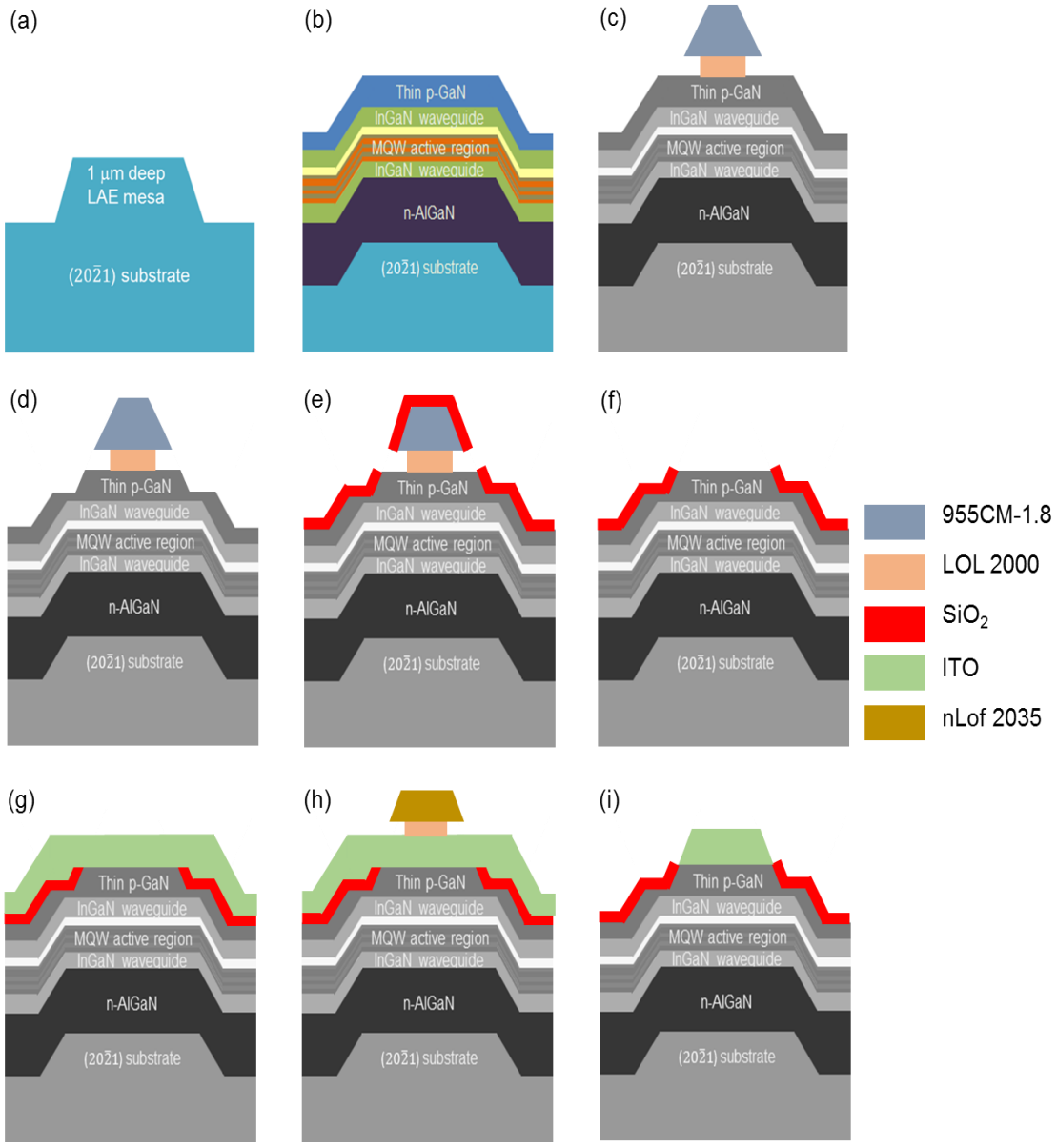

Figure 3.13 Step by step fabrication sequence for the LAE-ITO PF process, showing an individual ridge's profile for (a) LAE pre-growth mesa patterning (b) MOCVD growth of laser structure, (c) ridge lithography, (d) RIE ridge etch, (e) sputter deposition of dielectric, (f) dielectric liftoff, exposing top of the ridge for TCO deposition, (g) electron beam deposition of ITO (h) lithography for ITO MHA etch, and (i) MHA etch of ITO which removes ITO from the field.

ITO were deposited using electron beam evaporation, with the sample stage heated to 250 ^{o}C. Electron beam deposition of ITO is not preferential so the whole chip surface is covered in ITO. ITO top cladding requires longer processing than ZnO top cladding because and additional lithography and dry etch are required to remove the ITO from the field in between ridges. As shown in Fig. 3.13(h), the lithography consisted of a bilayer of LOL 2000 and n-LOF 2035.When using the PF mask set, this lithography requires a vertical pass shift so that a given ridge contains ITO along its whole length. This pass shift was optimized to be ± 185 μm from the center of the p-contacts' mask.

The ITO patterning was achieved through a methane-hydrogen-argon (MHA) RIE dry etch. The MHA etch had been problematic in previous ITO top clad laser devices because ITO residue redeposits during the ending O_2 cleaning step of the RIE etch. This issue was mitigated by breaking up the actual MHA etch and introducing a 50 second O_2 cleaning step for every 5 minutes of MHA etch. The details of the optimized MHA-O_2 cleaning RIE sequence are tabulated in Table 3.6.

After the ITO patterning, 30 nm of Ti was deposited by electron beam evaporation along the entire length of the laser ridge and then 30/1000 nm Ti/Au was deposited also by electron beam evaporation to form a p-contact pad, as is

Step	Gas	Individual gas flows (sccm)				Pressure (mTorr)	Bias (V)	Time	
		O_2	CH_4	H_2	Ar			*MHA etch*	*O_2 clean*
1	O_2	20				125	500		30 min
2	MHA		4	20	10	75	500	20 min	
3	MHA		4	20	10	75	350		5 min
4	O_2	20				125	170	50 sec	
5	MHA		4	20	10	75	350		5 min
6	O_2	20				125	170	50 sec	
7	MHA		4	20	10	75	350		6 min
8	O_2	20				125	300	5 min	

Table 3.6 Tabulated RIE etch conditions for the methane-hydrogen-argon (MHA) etch that removes ITO from the field and leaves it only on top the LD ridges. The oxygen cleaning in between the MHA etch steps proved crucial in reducing re-deposition of ITO on the sample during the RIE etch.

shown in Fig. 3.14(a)-(b). Just like in the TCO PF process, the thin Ti layer extended beyond the p-contact pad lengthwise on the LD ridges to ensure uniform current injection. The thin metal lithography uses negative resist (AZ n-LOF 2020) while the p-contact pad lithography uses a thick bilayer resist (OCG 825/SPR 955 CM-1.8) to enable clean liftoff of 1 μm of metal. Another similarity with the TCO PF process is the elimination of the HCl acid cleaning step between the thin metal lithography and metal deposition to preserve the quality of the ITO. The UV ozone is the only cleaning step for the thin metal lithography, which is used to remove any organic contamination prior to electron beam metal evaporation.[18]

The sample was then diced to form laser bars with a cavity length of 600

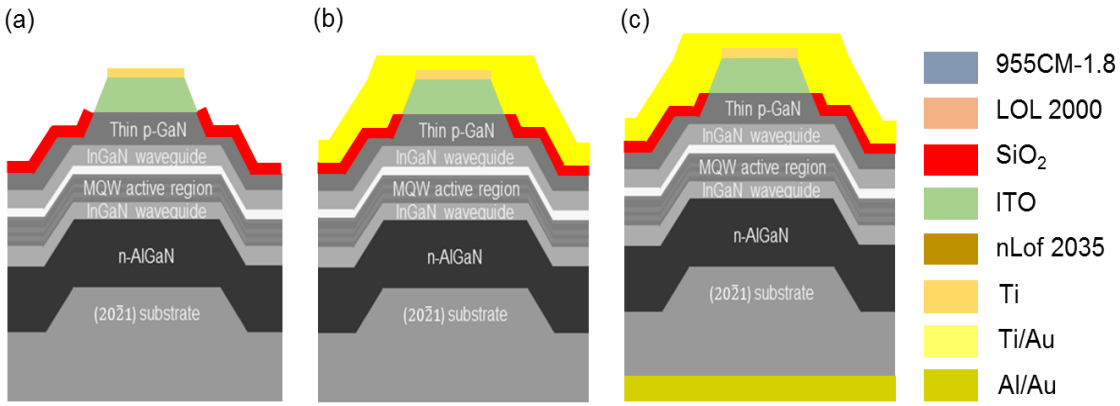

Figure 3.14 Continued step by step fabrication steps for the LAE-ITO PF process, showing (a) thin metal deposition, (b) p-contact deposition and (c) n-contact deposition after dicing and polishing of the laser chip.

μm, 900 μm and 1200 μm. The same double pass dicing sequence that was detailed in Section 2.3 was used for the LAE-ITO PF process. A diamond coated 2.187-4C-30RU-3 blade was used for dicing. Following dicing, the laser bars were polished with the same polishing films and sequence as discussed in Chapter 2.4 and detailed Table 2.5. The laser fabrication was completed with the deposition of a 50/300 nm Al/Au common back side contact via electron beam evaporation, illustrated in Fig. 3.14 (c). Fig. 3.15 shows an optical microscope top view image of a fully processed LAE-ITO laser bar.

3.5 Device results

The LD structure discussed in this section, whose structure is depicted in

CHAPTER 3. INDIUM TIN OXIDE TOP CLADDING LIMITED AREA EXPITAXY LASER DESIGN

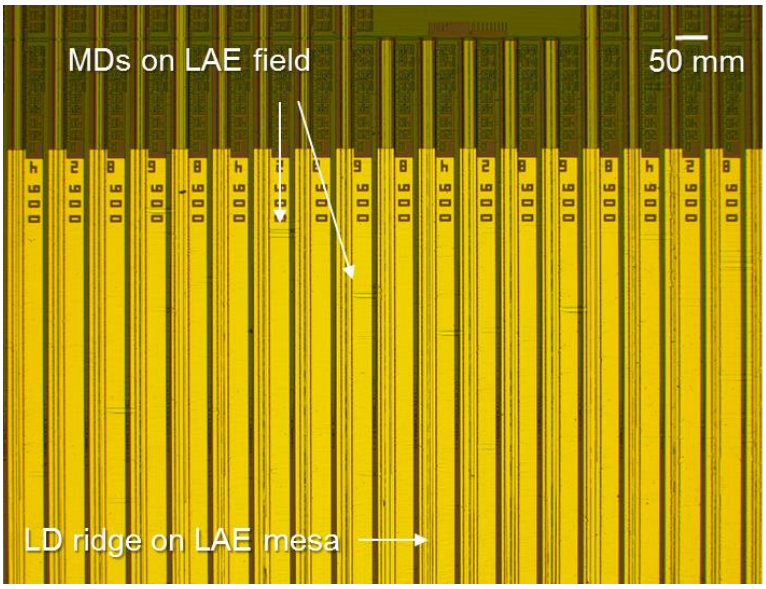

Figure 3.15 Optical microscope top view image of a finished LAE-ITO PF fabricated LD chip. Misfit dislocations (MDs) are visible in the field in between LAE mesas but no MDs are visible within LAE mesas. One of the ITO top clad LD ridges is pointed out to show how the LD ridges align on top of the LAE mesas. The thin metal clearly extends beyond the length of the p-contact pad to cover the full LD ridge, as can be seen for all ridges in this image.

Fig. 3.1, had a Γ of 6.3 % and α_i of 19.7 cm^{-1}. The simulated optical mode profile for the LD structure is shown in Fig. 3.16(a). The structure consisted of a 600 nm Si-doped GaN template, a 215 period $Al_{0.1}Ga_{0.9}N$/GaN modulation-doped short period superlattice (SPSL) n-cladding with a total thickness of ~1 μm and average AlN fraction of 5%, a 50 nm n-$In_{0.08}Ga_{0.92}N$ waveguiding layer, an undoped active region consisting of three 4.8 nm $In_{0.2}Ga_{0.8}N$ QWs and four 7.6 nm GaN QBs, a 10 nm p-$Al_{0.21}Ga_{0.79}N$ EBL, a 50 nm p-$In_{0.08}Ga_{0.92}N$ waveguiding layer, a 190 nm p-GaN layer, and a 10 nm p^+ GaN contact layer. The doping concentrations of the $Al_{0.5}Ga_{0.95}N$ n- cladding, $In_{0.08}Ga_{0.92}N$ n-waveguide,

$In_{0.08}Ga_{0.92}N$ p-waveguide, and GaN p-cladding measured by SIMS were 2 x 10^{18} cm^{-3}, 2.9 x 10^{18} cm^{-3}, 1 x 10^{19} cm^{-3}, and 1.3 x 10^{19} cm^{-3}, respectively.

200 nm was chosen considering the tradeoff between simulated Γ and α_i values of the LD and calculated p-GaN resistance values.[19] The p-GaN resistance calculations used our device geometry and assumed p-GaN resistivity of 0.4 Ω-cm, as reported from Castiglia *et. al.*[20] As discussed in Chapter 3.3, Γ decreases with increasing p-GaN thickness at a slower rate than α_i decreases with increasing p-GaN thickness. Our goal is to make p-GaN as thin as possible in the top cladding: given that optical simulations showed that a p-GaN thickness of 100 nm is the lower bound for ensuring mode confinement, we compared Γ, α_i and resistance values for p-GaN thicknesses of 100 nm, 200 nm and 300 nm, as shown in Table 3.7.

Quantitatively, Γ for 200 nm of p-GaN is 7.0 % lower than Γ for 100 nm, while Γ for 300 nm of p-GaN is 12.8 % lower than Γ for 100 nm. α_i for 200 nm of p-GaN is 22.2 % lower than α_i for 100 nm of p-GaN, while α_i for 300 nm of p-GaN is 36.8 % lower than α_i for 100 nm of p-GaN. While the rapid decrease in internal loss with thicker p-GaN is optically favorable, the resistivity of 300 nm of p-GaN is 50 % higher than the resistivity of 200 nm of p-GaN. Considering also p-GaN growth temperature and time with the tradeoff between Γ, α_i and p-GaN

Change in p-GaN thickness (nm)	Change in G (% decrease)	Change in a_i (% decrease)	Change in p-GaN resistance (% increase)
100 to 200	7	22.2	99.5
100 to 300	12.8	36.8	198.9
200 to 300	5.5	11.9	49.9

Table 3.7 Evaluation of the effect of increasing p-GaN thickness in the top cladding on LD confinement factor and internal mode loss and p-GaN resistance contribution, based on optical modeling values and resistance calculations done our device geometry, assuming a p-GaN resistivity of 0.4 Ω-cm.

resistance, we chose 200 nm for this demonstration, sacrificing a little higher α_i for higher Γ and lower p-GaN resistance contribution to the overall device.

Figure 3.16(b) shows the measured light-current-voltage (*L-I-V*) characteristic of a 1.8 μm wide by 1200 μm long ridge waveguide LD with uncoated facets. The device was tested under pulsed electrical injection with a pulse width of 1μs and 1% duty cycle. Lasing was achieved at a threshold current (I_{th}) of 184 mA, a threshold current density (J_{th}) of 8.5 kA/cm^2, and a threshold voltage (V_{th}) of 8.4 V. The differential resistance (R_d) was 9.9 Ω for currents corresponds to a single facet differential efficiency (η_d) of 7.53%. Assuming equal power output from both facets, the experimental η_d was 15.06 %. The current dependent spectra in Fig. 3.16(c) shows a single emission peak centered at 446 nm. The LD far field pattern is shown in the inset.

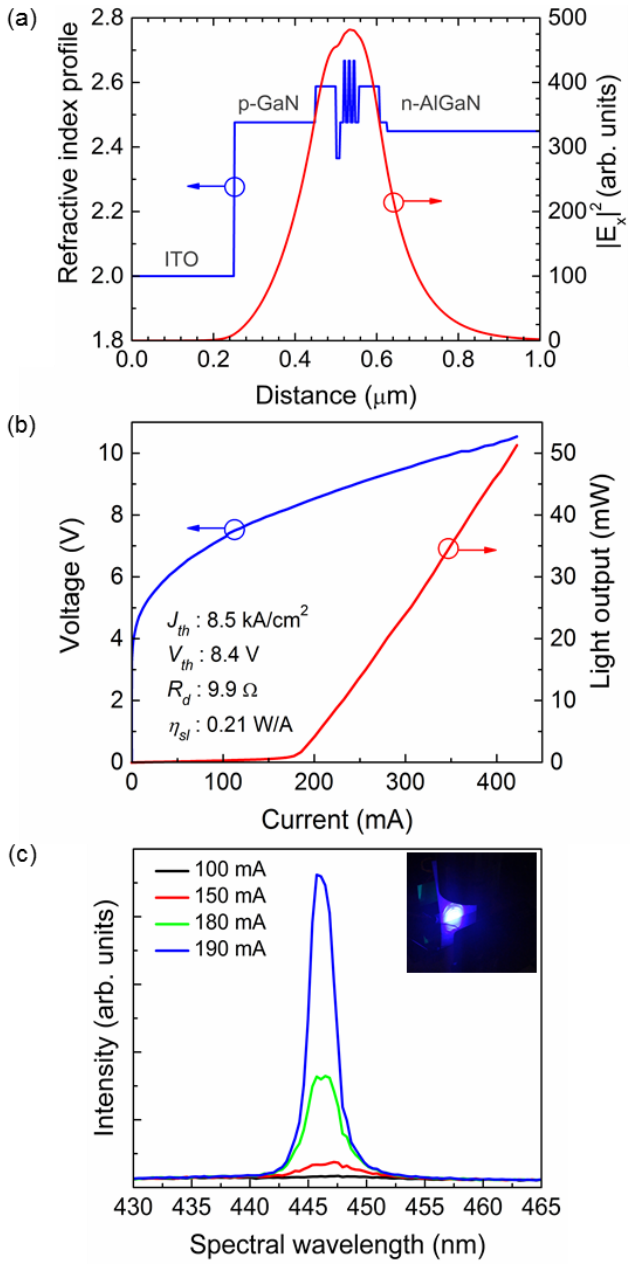

Figure 3.16 (a) Transverse mode profile and refractive index of the LD as a function of distance in the growth direction, (b) pulsed *L-I-V* characteristics and (c) current dependent spectra of a 1.8 μm wide by 1200 μm long LD. The far field patter is shown in the inset.

greater than 200 mA and single facet slope efficiency (η_{sl}) was 0.21 W/A, which

CHAPTER 3. INDIUM TIN OXIDE TOP CLADDING LIMITED AREA EXPITAXY LASER DESIGN

The experimental η_d of 15.06% is much lower than the simulation η_d value of 27.3 % that was predicted for this laser by FIMMWAVE modeling. Differential efficiency is highly dependent on laser mirror facet quality. We were unable to measure *L-I-V* characteristics from both facets because the device failed and got damaged after the current dependent spectra measurement, so we have no direct comparison of the laser's two facets polishing quality. We expect that improved facet polishing will result in higher differential efficiency. Another factor to consider, is the LD's experimental internal mode loss. This laser structure's mode loss could've been higher than expected due to possible poor quality of the ITO. The deposition conditions of the heated stage, electron beam deposited ITO used for this laser demonstration were not optimized. The deposition conditions in the e-beam system used to deposit ITO are sometimes non-repeatable, so it is possible that the ITO deposited on the LD chip was nonuniform and possibly a different thickness than that expected from our calibration ITO deposition.

A first-glance comparison of the optical modeling and device characteristics of this blue-emitting $(20\bar{2}1)$ LAE-ITO LD with those reported by Hardy *et.al.* in Reference 7 for a blue-emitting $(20\bar{2}1)$ planar substrate-ITO LD would suggest that n-GaN bottom cladding resulted in higher confinment factor than n-AlGaN for an ITO top clad device. However, the n-GaN clad LD reported

by Hardy *et. al.* had a different active region than the blue n-AlGaN clad LD demonstrated in this work. Specifically, Hardy *et. al.* had an active region consisting of a 3 period 4.5/10 nm InGaN/GaN QW/QB active region,[7] while our design has a 3 period 4.8/7.6 nm InGaN/GaN QW/QB region.[19] The active region design of our n-AlGaN clad design was also used for the n-GaN clad comparison LD in the optical modeling discussed in Chapter 3.3. The thinner barriers in the active region correspond to a higher confinement factor for the n-GaN clad design. It is noteworthy to point out that the threshold current density, J_{th} reported in Hardy *et. al.* for the n-GaN clad design is different than our n-AlGaN design because the two devices have different dimensions and different threshold currents, I_{th}. The blue n-GaN clad LD reported in Hardy *et. al.* was a 7.5 μm x 1800 μm long LD, which lased at I_{th} of 880 mA, while the blue n-AlGaN clad LD reported in this letter was a 1.8 μm x 1200 μm long LD, which lased at I_{th} of 184 mA. The laser stripe dimensions account for the lower threshold current density, J_{th}, reported by Hardy *et. al.*

3.6 Conclusions

In summary, we have investigated the LAE-TCO design for $(20\bar{2}1)$ III-nitride LDs for various Al compositions in the AlGaN bottom cladding layer and

CHAPTER 3. INDIUM TIN OXIDE TOP CLADDING LIMITED AREA EXPITAXY LASER DESIGN

ITO and ZnO top cladding layers. Numerical modeling indicated that increasing the Al composition in the bottom cladding increases the LD's confinement factor and internal mode loss, while replacing ITO with ZnO reduces the lasers' internal mode loss. The choice of TCO has negligible effect on the laser design for p-GaN thicknesses higher than 400 nm for all Al compositions simulated. Lasing was achieved at a threshold current of 184 mA, a threshold current density of 8.5 kA/cm^2, and a threshold voltage of 8.4 V for a 1.8 μm wide by 1200 μm long ridge waveguide LD with uncoated facets.

Bibliography

[1] D. Hull and D.J. Bacon, *Introduction to Dislocations*, 5th ed. (Elsevier, Burlington, MA, 2011).

[2] E.A. Fitzgerald, G.P. Watson, R.E. Preano, and D.G. Ast, **65**, 2220 (1989).

[3] M.T. Hardy, Stress Engineering for Semipolar (20 ¯ 21) Blue and Green InGaN Based Laser Diodes, 2013.

[4] D.H. Yoon, K.S. Lee, J.B. Yoo, and T.Y. Seong, Japanese J. Appl. Physics, Part 1 Regul. Pap. Short Notes Rev. Pap. **41**, 1253 (2002).

[5] J. Kim, H. Kim, and S.N. Lee, Curr. Appl. Phys. **11**, S167 (2011).

[6] M.T. Hardy, S. Nakamura, J.S. Speck, and S.P. Denbaars, Appl. Phys. Lett. **101**, 0 (2012).

[7] M.T. Hardy, C.O. Holder, D.F. Feezell, S. Nakamura, J.S. Speck, D. a. Cohen, and S.P. DenBaars, Appl. Phys. Lett. **103**, 81103 (2013).

[8] S.-N. Lee, J. Son, T. Sakong, W. Lee, H. Paek, E. Yoon, J. Kim, Y.-H. Cho, O. Nam, and Y. Park, J. Cryst. Growth **272**, 455 (2004).

[9](2011).

[10] E.C. Young, C.S. Gallinat, A.E. Romanov, A. Tyagi, F. Wu, and J.S. Speck, Appl. Phys. Express **3**, 111002 (2010).

[11] A.M. Smirnov, E.C. Young, V.E. Bougrov, J.S. Speck, and A.E. Romanov, APL Mater. **4**, (2016).

[12] R. Goldhahn, a. T. Winzer, a. Dadgar, a. Krost, O. Weidemann, and M. Eickhoff, Phys. Status Solidi Appl. Mater. Sci. **204**, 447 (2007).

[13] E. Kioupakis, P. Rinke, and C.G. Van De Walle, Appl. Phys. Express **3**, 82101 (2010).

[14] E. Kioupakis, P. Rinke, A. Schleife, F. Bechstedt, and C.G. Van de Walle, Phys. Rev. B **81**, 241201 (2010).

[15] A.H. Reading, J.J. Richardson, C.-C. Pan, S. Nakamura, and S.P. DenBaars,

Opt. Express **20**, A13 (2012).

[16] R.M. Farrell, D.A. Haeger, P.S. Hsu, K. Fujito, D.F. Feezell, S.P. Denbaars, J.S. Speck, and S. Nakamura, Appl. Phys. Lett. **99**, 17 (2011).

[17] L.A. Coldren, S.W. Corzine, and M.L. Masanovic, *Diode Lasers and Photonic Integrated Circuits* (John Wiley & Sons, Inc., 2012).

[18] J.R. Vig, J. Vac. Sci. Technol. A Vacuum, Surfaces, Film. **3**, 1027 (1985).

[19] A. Myzaferi, A.H. Reading, D.A. Cohen, R.M. Farrell, S. Nakamura, J.S. Speck, and S.P. DenBaars, Appl. Phys. Lett. **109**, 61109 (2016).

[20] A. Castiglia, J.F. Carlin, and N. Grandjean, Appl. Phys. Lett. **98**, 96 (2011).

4

Zinc oxide top cladding limited area epitaxy laser design

4.1 Introduction

THIS chapter discusses the design used to demonstrate a $(20\bar{2}1)$ limited area epitaxy-transparent conducting oxide (LAE-TCO) laser design using a ZnO layer in the top cladding. This laser had a high yield with pulsed lasing achieved for various mesa widths and lengths in the blue region of the spectrum. Furthermore, continuous wave (CW) operation was achieved for several 4 μm x 1200 μm uncoated laser diodes (LDs). This was the first blue emitting CW LD demonstration on the $(20\bar{2}1)$ plane at UCSB.

CHAPTER 4. ZINC OXIDE TOP CLADDING LIMITED AREA EPITAXY LASER DESIGN

The chapter introduces additional optical modeling of the LAE-TCO design which investigates the minimum thickness of the n-AlGaN bottom cladding that would provide mode confinement without mode leakage into the substrate. The optimization of the solution chemistry for hydrothermal deposition of ZnO is an ongoing process: Chapter 4.3 details the new solution chemistry and structural characterization of ZnO films. The LAE-ZnO PF processing required additional development of the polishing sequence, which is discussed in Chapter 4.4. Chapter 4.5 presents all the pulsed and CW light-current-voltage (LIV) characteristics of the devices that lased as well as their current dependent spectra and far field patterns. The results are summarized in Chapter 4.6 and Chapter 4.7 lists possible future work for the semipolar LAE-TCO LD design.

4.2 Device Optical Modeling and Design

In Chapter 3.2 the LAE-TCO LD FIMMWAVE optical modeling mapped out the tradeoff between confinement factor (Γ) and internal mode loss (α_i) by investigating the dependence of Γ and α_i on the following parameters: Al composition in the bottom cladding, p-GaN thickness, and TCO choice in the top cladding. One of the main LAE-TCO structure design goals is to reduce the overall internal loss of the device. One way to do that is to lower the loss contribution of individual layers. Loss increases with increasing alloy

composition,[1] and since higher Al compositions result in higher confinement factor for this design,[2] the thickness of the AlGaN bottom cladding should be optimized to both reduce the thickness of higher absorbing bottom cladding (compared to GaN bottom cladding) and reduce the relaxation in the overall epitaxial structure during MOCVD growth.

LAE pre-growth patterning of the substrate enables the incorporation of AlGaN bottom cladding in semipolar III-nitride laser design, as described in Chapter 1.4 and Chapter 3.3. The LAE stripe mesas are aligned parallel to the $[\bar{1}014]$ direction to block threading dislocation (TD) glide that results in *c*-plane slip.[3] This stripe mesa alignment is concurrently beneficial for $(20\bar{2}1)$ LD design due to in-plane gain anisotropy.[4] The LAE stripe geometry and AlGaN thickness used for the device in Chapter 3 was based on the work done in Chapter 7 of Reference 3. The AlGaN bottom cladding in those devices, which was grown using a modulated doping short period superlattice (SPSL), had a total thickness of ~1 μm.[3,5] Even though LAE enables the growth of AlGaN well past its critical thickness for relaxation, it is still strained material therefore the thickness of the bottom cladding layer should be optimized. To this end, the dependence of Γ and α_i on varying n-AlGaN thickness and Al composition was modeled for both TCOs. This modeling study explored how thin the AlGaN bottom cladding can be for a given Al composition without compromising the mode confinements and

benefits of the LAE-TCO design.

The optical modeling performed in Chapter 4.2 utilized the LAE-TCO LD structure depicted in Fig. 3.1 and detailed in Table 3.1 as a baseline. Contrary to the simulations in Chapter 3.3, in this chapter's subsequent simulations the p-GaN and TCO layer thicknesses in the top cladding were fixed at 200 nm and 250 nm, respectively. All simulations were done at a wavelength of 450 nm, for a symmetric 8% In composition InGaN waveguide (WG), i.e. 50 nm/50nm n-/p-$In_{0.08}Ga_{0.92}N$ WG. The AlGaN bottom cladding thickness was varied from 0 nm to 1000 nm, for 5% and 12% Al composition, and compared replacing ITO with ZnO in the top cladding layer.

The refractive index values, parameters and coefficients necessary for setting up the FIMMWAVE simulations were obtained and estimated in the same manner as was done for Chapters 2.3 and 3.3. Namely, the refractive indices for the III-nitride layers of the LD structure were taken or calculated from Goldhahn *et. al.*[6] The absorption coefficients for the III-nitride layers were adapted from Kioupakis *et. al.*[7], using the same assumptions detailed in Chapter 2.3.The refractive indices of ITO and ZnO were taken from Hardy *et.al.*[8] and Reading *et.al.*[9], respectively. The absorption coefficient of ITO of 2000 cm^{-1} and the absorption coefficient of UID ZnO of 100 cm^{-1} were also taken from References 8 and 9, respectively.

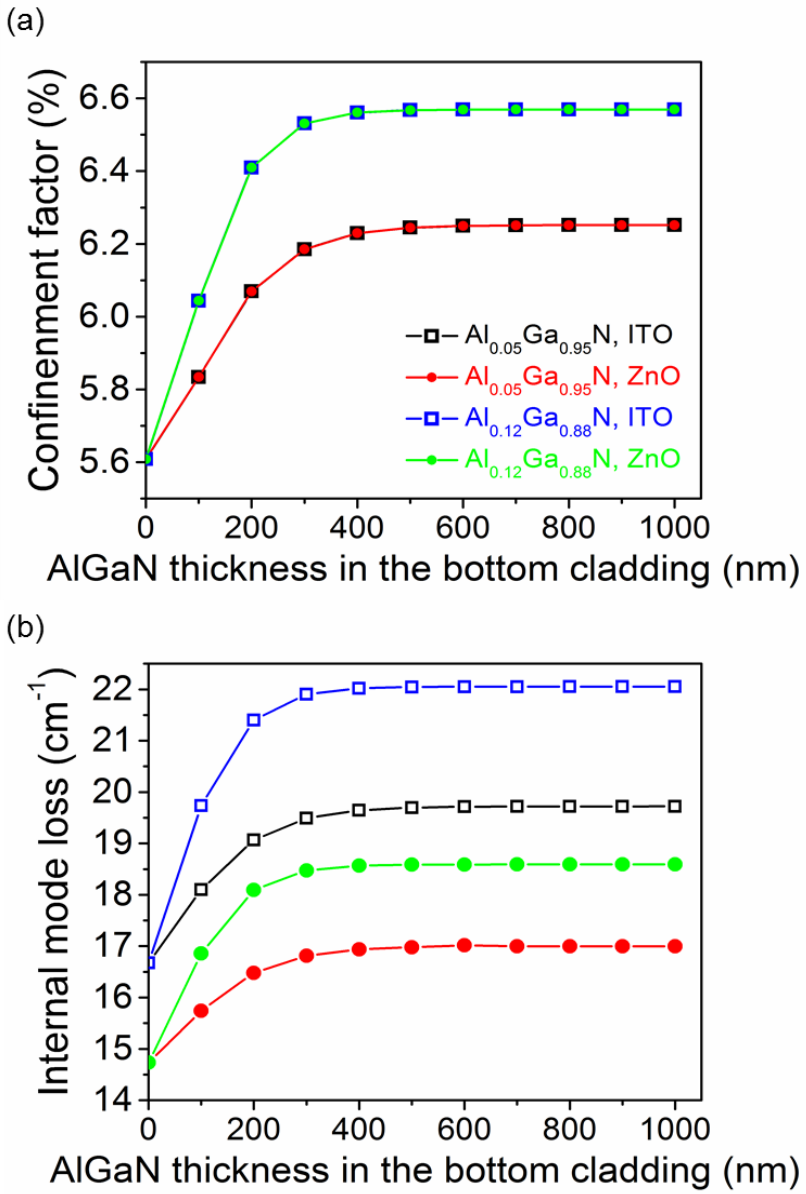

Figure 4.1 Dependence of (a) confinement factor and (b) internal mode loss on the AlGaN bottom cladding for devices with 5% and 12 % Al composition in the bottom cladding and 250 nm of ITO or ZnO in the top cladding. For both Al compositions, the change confinement factor and internal mode loss is negligible for AlGaN thicknesses between 500 nm and 1000 nm.

CHAPTER 4. ZINC OXIDE TOP CLADDING LIMITED AREA EPITAXY LASER DESIGN

Fig. 4.1 shows the dependence of confinement factor and internal mode loss on the AlGaN thickness in the bottom cladding for Al compositions of 5% and 12%, for fixed p-GaN and TCO thicknesses of 200 nm and 250 nm, respectively, in the top cladding. We chose this p-GaN thickness because the modeling results in Chapter 3.3 suggested it offers a favorable tradeoff between Γ and α_i. As expected, Fig. 4.1(a) shows that the confinement factor is independent of the TCO material in the top cladding for all AlGaN bottom cladding thicknesses for each Al compositions. This is expected, as the refractive index value for both ITO and ZnO in the blue region is 2, therefore the TCO choice doesn't affect the overall index contrast profile of the structure. The refractive index decreases with increasing Al composition, so another expected result is the increasing confinement factor with increasing Al composition in the bottom cladding.

Fig. 4.1(a) shows that the confinement factor value is relatively unchanged for n-AlGaN thicknesses between 500 nm and 1000 nm, for both Al compositions modeled. This is important for optimizing the LAE-TCO design because it indicates that we can reduce the overall strain in the structure by growing a thinner n-AlGaN bottom cladding without sacrificing the confinement factor of the optical mode. For n-AlGaN thicknesses between 0 nm and 400 nm, the confinement factor decreases with decreasing AlGaN thickness in the bottom

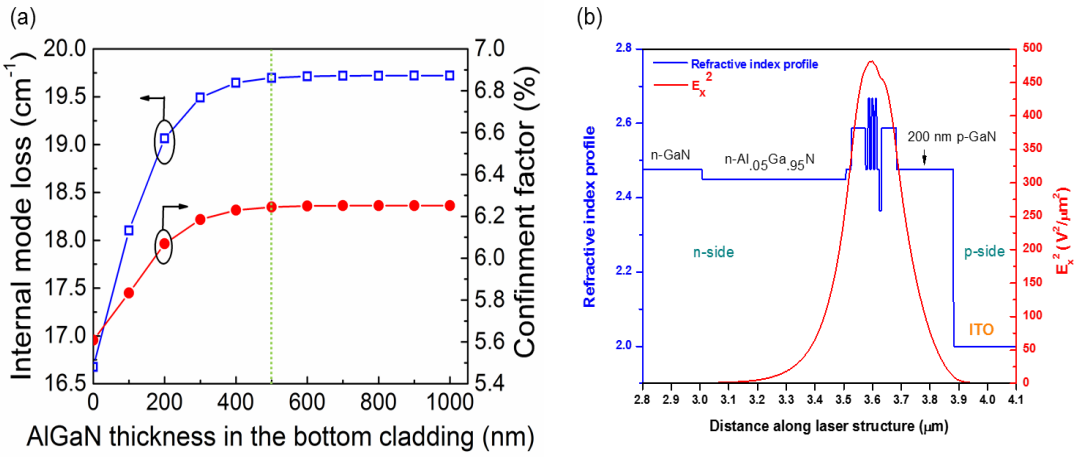

Figure 4.2 (a) Dependence of confinement factor and internal mode loss on the AlGaN bottom cladding for devices with 5% Al composition in the bottom cladding and 200 nm of p-GaN and 250 nm of ITO in the top cladding. The green dotted line denotes the n-AlGaN thickness of the structure whose transverse mode profile is shown in (b). An $Al_{0.05}Ga_{0.95}N$ thickness of 500 nm doesn't result in any mode leakage into the substrate.

cladding, making these bottom cladding thicknesses unfavorable for the LAE-TCO design.

Fig. 4.1(b) shows that the dependence of internal mode loss on AlGaN bottom cladding thickness follows a similar pattern to the dependence of the confinement factor. For n-AlGaN thicknesses between 500 nm and 1000 nm, the internal mode loss value is relatively unchanged. As expected, the devices with ITO top cladding have higher internal mode loss than the devices with ZnO top cladding for all AlGaN thickness and both Al compositions, because the assumed absorption coefficients of ITO and ZnO are 2000 cm^{-1},[8] and 100 cm^{-1},[9] respectively. For AlGaN thicknesses between 0 nm and 400 nm, the internal mode

loss decreases with decreasing bottom cladding thickness. While this can be favorable, it comes with a reduction in confinement factor, although α_i decreases faster than Γ for both ITO and ZnO so design tradeoffs are possible.

Although the dependence of Γ and α_i on AlGaN thickness suggests that the mode confinement should be unaffected by thinning the bottom cladding, it is important to make sure the mode doesn't leak into the substrate. Since Γ is relatively unchanged for AlGaN thicknesses down to 400 nm, as indicated by the green dotted line in Fig. 4.2(a), the transverse mode profile of the mode of a structure with 500 nm of AlGaN in the bottom cladding is plotted in Fig. 4.2(b). As can be seen in Fig. 4.2(b) the mode tail dies off in the GaN buffer layer, before it can see the substrate. This further supports an LAE-TCO design with thinner n-AlGaN bottom cladding.

To tests the effects of a thinner bottom cladding on device performance, a 750 nm thick n-AlGaN layer was chosen to be experimentally tested. We chose this thickness based on the modeling results from Fig. 4.2 as a stable point for both confinement factor and internal mode loss. The waveguide asymmetry for a device with 750 nm of n-AlGaN and 200 nm of p-GaN and 250 nm of ZnO in the top cladding was investigated by modeling the dependence of Γ and α_i on the thickness of the n-$In_{0.08}Ga_{0.92}N$ waveguide thickness. The modeling indicated that a structure with 60 nm of n-$In_{0.08}Ga_{0.92}N$ and 40 nm of p-$In_{0.08}Ga_{0.92}N$ resulted in

the best tradeoff between high confinement factor and low internal mode loss. For all these simulations as well as for the actual demonstrated device, ZnO was chosen as the TCO in the top cladding based on the simulation results in Chapter 3.3, due to its promise for lower contribution to the LD mode loss compared to ITO top cladding.

Attempting to further lower the overall strain relaxation in the laser structure, the LD whose device characteristics are discussed in chapter 4.5 had thinner quantum wells than the device demonstrated in Chapter 3.5. Experimentally, the design changes of thinning out the AlGaN in the bottom cladding and thinning the QWs are supported by fluorescence microscopy (FLM) characterizations of as-grown LAE III-nitride device surfaces. Fig. 4.3(a) shows the FLM image of a laser with 1 μm thick AlGaN in the bottom cladding and 4.8 nm thick QWs while Fig. 4.3(b) shows the FLM image of a laser with 750 nm of AlGaN in the bottom cladding and 3.7 nm QWs. Both these LD structures had a 100 nm thick $In_{0.08}Ga_{0.92}N$ waveguiding layer and 200 nm of p-GaN in the top cladding. As can be seen in Fig. 4.3(a), the sample with thicker AlGaN and QWs has a higher density of misfit dislocations on its LAE stripe mesas than the sample with thinner AlGaN and QWs, which is shown in Fig. 4.3(b). Non-basal slip (crisscross patterns) is observed in the field between the LAE strip mesas for both LD structures. This FLM comparisons is not definitive proof of the repeatable

benefits of thinning out the bottom cladding and the QWs, but it does suggest

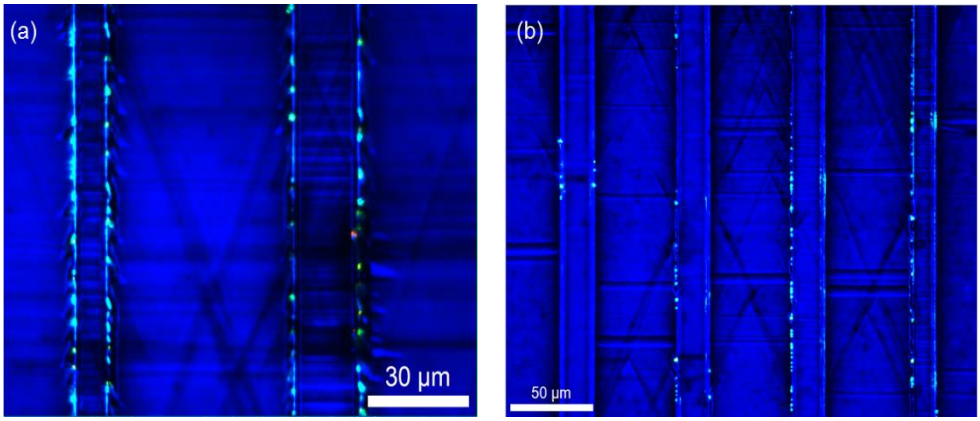

Figure 4.3 Fluorescence microscope of LAE LDs with (a) 1 µm thick AlGaN in the bottom cladding and 4.8 nm thick quantum well and with (b) 750 nm of AlGaN in the bottom cladding and 3.7 nm quantum wells. The structure with thicker AlGaN bottom cladding and thicker quantum wells has a higher density of misfit dislocations visible on the LAE stripe mesas. Non-basal slip is observed in the field between the LAE stripe mesas for both laser structures.

improved device material quality through observing reduced density of strain relaxation related defects.

The full LD structure whose results are presented in Chapter 4.5 consisted of 600 nm Si-doped GaN template, followed by a 186 period $Al_{0.1}Ga_{0.9}N$/GaN modulation-doped SPSL n-cladding, having a total thickness of ~750 nm and average AlN fraction of 5%. Following the cladding, the structure consisted of a 60 nm n-$In_{0.08}Ga_{0.92}N$ waveguiding layer, an undoped active region consisting of three unintentionally doped (UID) 3.7 nm $In_{0.2}Ga_{0.8}N$ QWs and four 7.6 nm GaN QBs, a 10 nm p-$Al_{0.21}Ga_{0.79}N$ EBL, a 40 nm p-$In_{0.08}Ga_{0.92}N$ waveguiding layer, a 205 nm p-GaN layer, and 12 nm p^+ GaN contact layer. ZnO was then deposited

using the hydrothermal method. The improved solution chemistry and additional ZnO film structural characterization will be presented in the next section.

4.3 Characterization of ZnO film morphology

Improving the solution stoichiometry of low temperature aqueous solution deposition of ZnO is an on-going process. This method of ZnO deposition, which can be applied to both light emitting diodes (LEDs) and LDs, was optimized for both semipolar and *c*-plane devices,[9,10] but the solution chemistry of the ZnO seed

Precursor	***Semipolar sequence***		***c-plane sequence***	
	Seed layer	**2nd layer**	**Seed layer**	**2nd layer**
18 MΩ DI H_2O	90 mL	90 mL	90 mL	90 mL
Trisodium citrate $Na_3C_6H_5O_7$	0.13 g	0.13 g	-	0.13 g
Zinc nitrate hexa-hydrate $Zn(NO_3)_2{:}6H_2O$	0.67 g	0.67 g	0.54 g	0.67 g
Ammonium nitrate NH_4NO_3	-	-	2.52 g	-
Ammonium hydroxide NH_4OH 29% concentration	4.68 mL	4.68 mL	0.47 mL	4.68 mL
N_2 anneal	500 °C	250 °C	500 °C	250 °C

Table 4.1 List of precursors amounts and anneal times for low temperature aqueous deposition of ZnO, for the semipolar and *c*-plane deposition sequences. All anneal times are 15 minutes. Solution chemistry courtesy of Asad Mughal

layer for semipolar devices is different from that of *c*-plane devices.[11] We'll refer

to the solution chemistry used for ZnO growth on $(20\bar{2}1)$ devices as the semipolar sequence and the solution chemistry used for ZnO growth on (0001) devices as the *c*-plane sequence. Both semipolar and *c*-plane sequences were successfully applied to $(20\bar{2}1)$ planar-TCO lasers, but a systematic comparison of the structure and morphology of the two growth sequences on this crystal plane had not been conducted. To that end, ZnO was hydrothermally deposited on free standing $(20\bar{2}1)$ bulk GaN substrates, using both the semipolar and *c*-plane sequences and4.1 details the precursor amounts and annealing conditions that were used for this comparison study.

Fig. 4.5 shows the SEM top view images of the seed layer of ZnO for the two aqueous deposition solution chemistries. Fig. 4.5(a)-(c) shows the ZnO seed layer morphology that results from the semipolar sequence. As is observed, this layer grows in layered, lamellar-like stacks that are parallel to the growth surface, without fully coalescing. The zoomed-out SEM image in Fig. 4.5(b) shows that although it is not a fully coalesced layer, the ZnO lamellar-like features are very dense, closely packed and they cover the whole growth surface. Their size varies, as seen in Fig. 4.5(c): their width ranges from ~0.44 μm to ~0.64 μm while their length ranges from ~0.7 μm to ~1.13 μm.

Fig. 4.5(d)-(f) shows the SEM top view images of the ZnO seed layer surface morphology that results from the *c*-plane sequence. Contrary to the

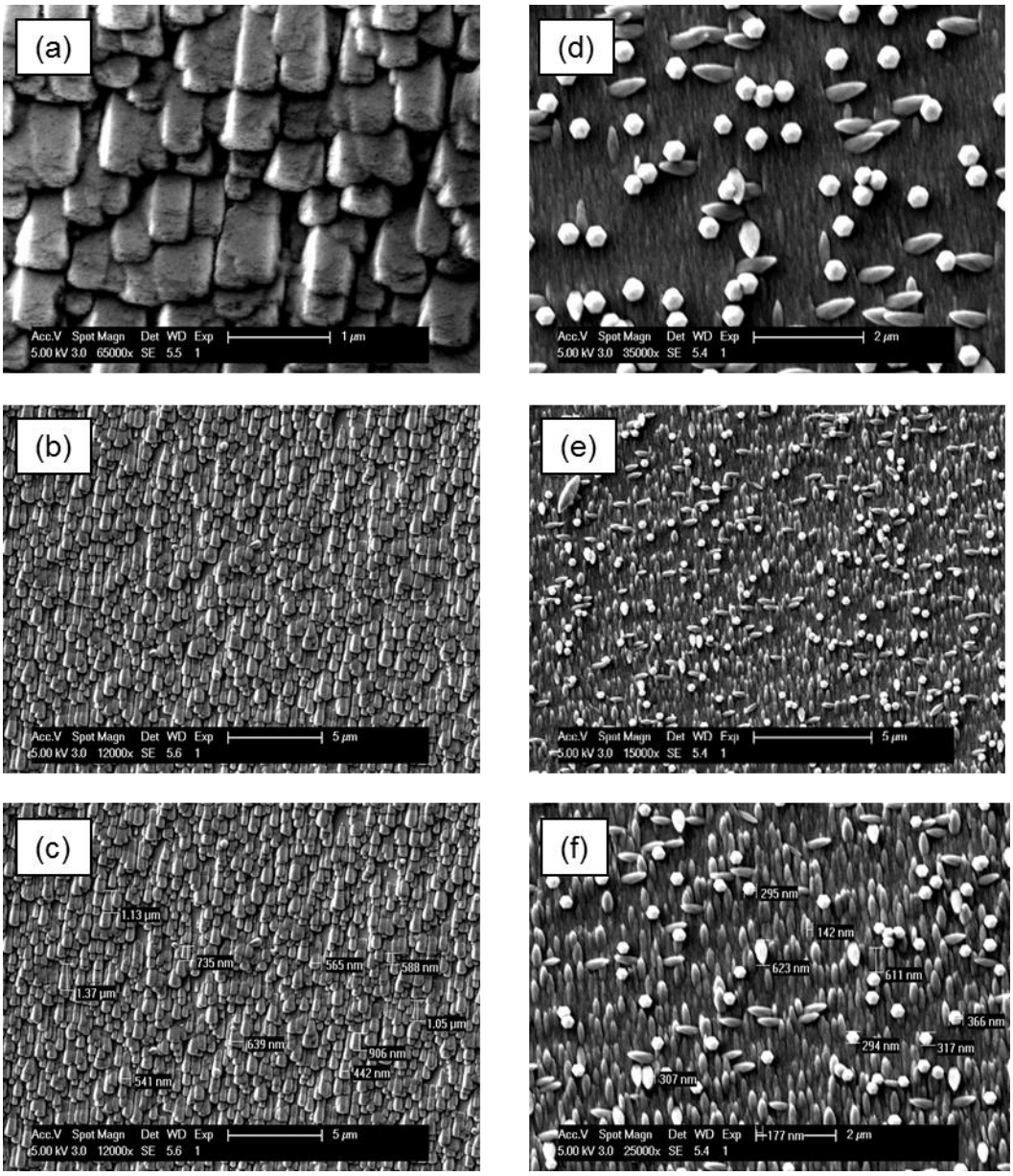

Figure 4.5 Top view SEM images of the ZnO seed layer using (a)-(c) the semipolar sequence and (d)-(f) the *c*-plane sequence. The semipolar sequence results in dense lamellar-like ZnO crystal stacks which the *c*-plane sequence results in higher film coalescence and protruding pillar like formations. The ZnO seed crystals vary in size for both deposition chemistry sequences.

the samples were characterized using scanning electron microscopy (SEM). Table

semipolar sequence, the morphology resulting from the *c*-plane sequence solution chemistry indicates a more coalesced seed layer with pointed hexagonal pillar-like ZnO formations protruding from the film. The zoomed-out image in Fig. 4.5(e) shows a film that covers the whole growth surface without any visible gaps. The ZnO hexagonal pillars are mostly vertically aligned in the direction of the growth surface, but some of them are aligned along various directions. The diameter of the vertically aligned pillars ranges from ~190nm to ~370 nm. The length of the not-vertically aligned pillars is in the order of 600 nm.

The surface morphology of the second ZnO layer for both solution chemistries is shown in the top view SEM images in Fig. 4.6. Fig. 4.6(a)-(c) shows the ZnO surface resulting from the semipolar sequence. The second layer is fully coalesced and has hexagonal features protruding from the planar ZnO surface towards the *c*+ projection, which has been observed before.[11] These hexagonal features width ranges from ~2.2 μm to ~2.7 μm, as seen in Fig. 4.6(c). Contrarily, the ZnO second layer surface resulting from the *c*-plane sequence, shown in Fig. 4.6(d)-(f), is not fully coalesced, and has visible gaps in between staggered, flat features. These features, which are hexagonally shaped, seem to have different heights as suggested by the gaps in the layered/staggered surface. The features' width ranges from ~2 μm to ~2.6 μm.

Both samples were cleaved to observe the cross-sectional morphology of

CHAPTER 4. ZINC OXIDE TOP CLADDING LIMITED AREA EPITAXY LASER DESIGN

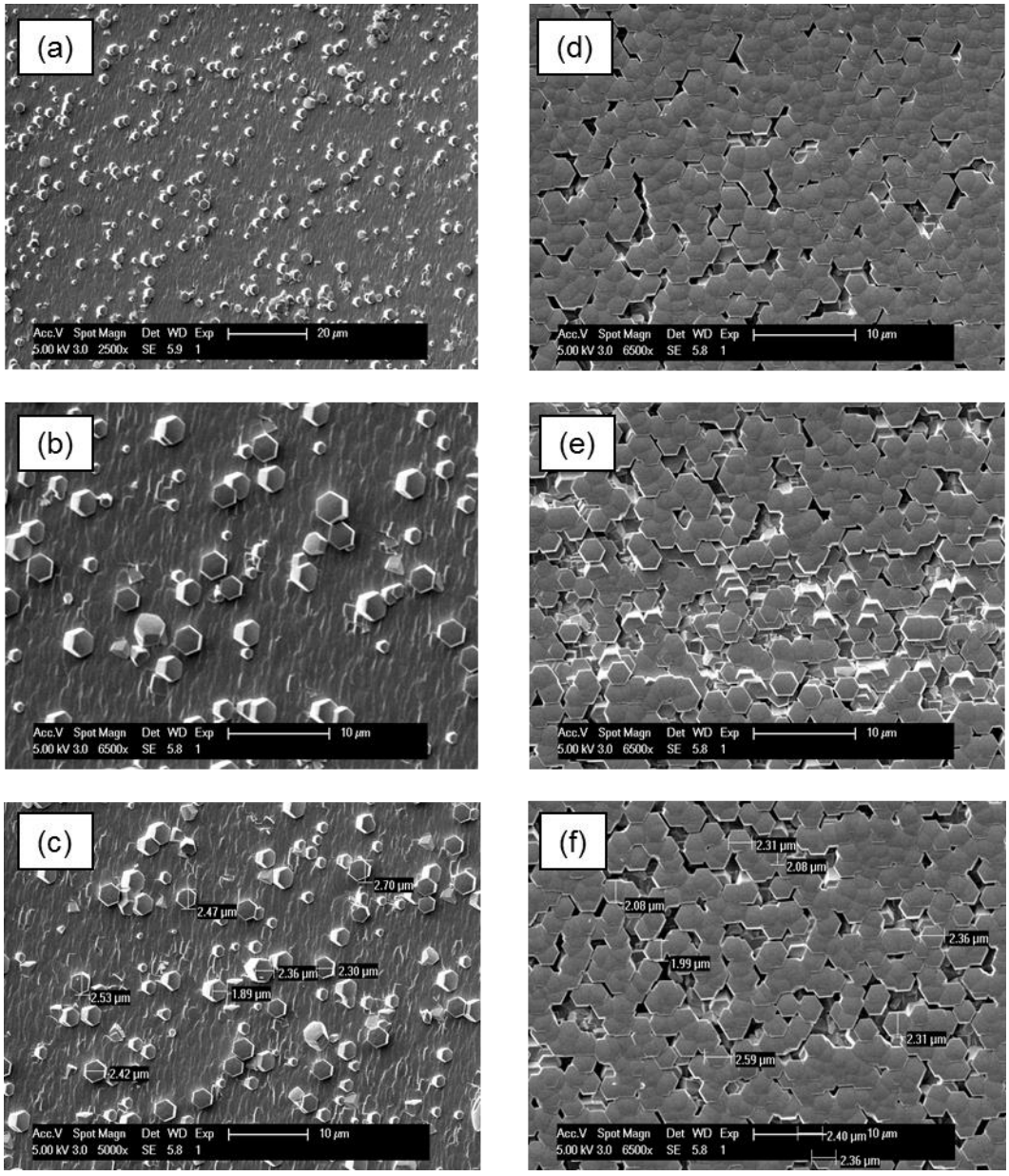

Figure 4.6 Top view SEM images of the ZnO second layer using (a)-(c) the semipolar sequence and (d)-(f) the *c*-plane sequence. The semipolar sequence results in a fully coalesced planar surface which the *c*-plane sequence results in the staggered surface gaps.

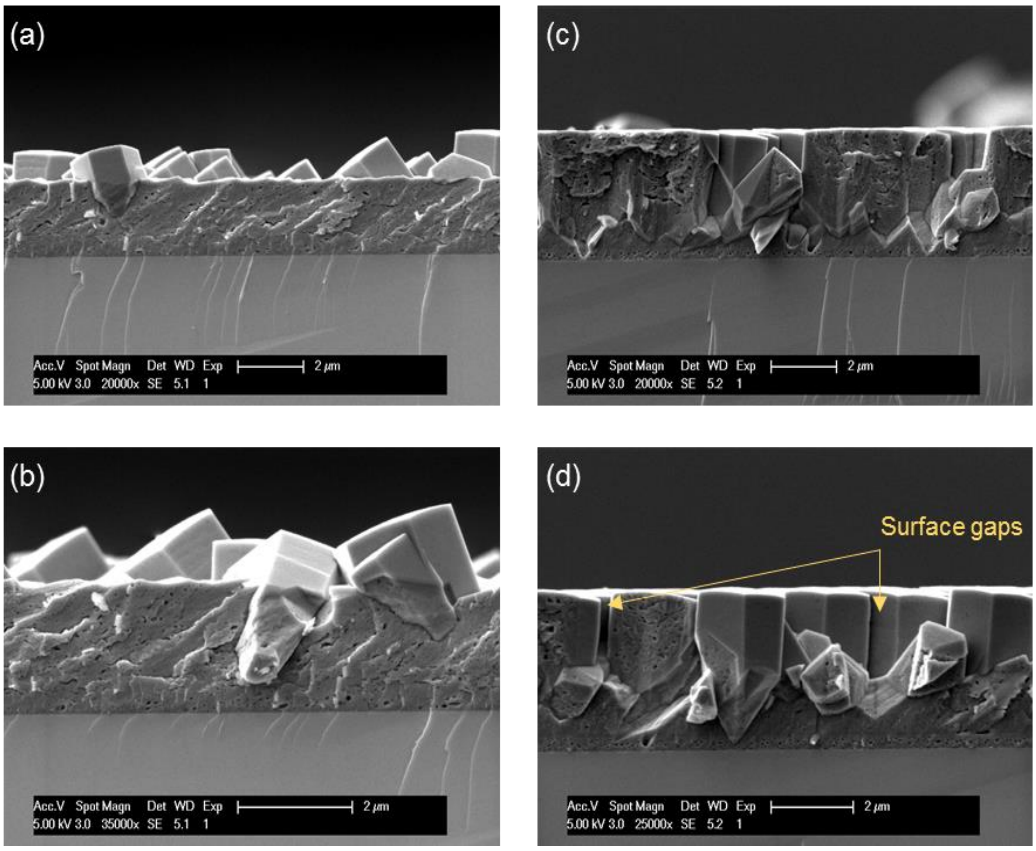

Figure 4.7 Cross sectional SEM images of the ZnO second layer for (a)-(b) the semipolar solution chemistry and (c)-(d) for the *c*-plane solution chemistry. The semipolar sequence deposition results in a fully coalesced surface without structural gaps. Porosity of the ZnO layer is observed. In contrast, the *c*-plane sequence deposition results in surface gaps that extend throughout the whole film.

the bilayer ZnO films. Fig 4.7(a)-(b) shows that the semipolar sequence results in a continuous, fully coalesced, albeit porous second ZnO layer. In contrast, the *c*-plane sequence results in a ZnO second layer that isn't fully coalesced as it consists of hexagonal pillars aligned vertically to the growth direction with clearly visible gaps between them. In addition, the interface between the ZnO seed layer

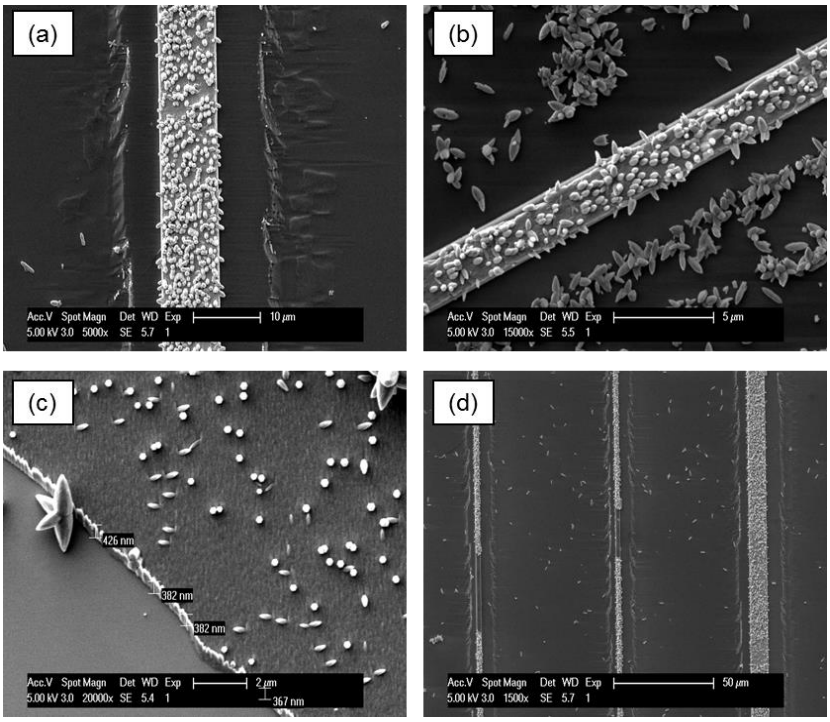

Figure 4.8 SEM top view images of ZnO deposited on LAE stripe mesas of an LD, showing (a) ZnO seed layer crystals on LAE stripe mesa, (b) ZnO 2nd layer on LAE mesa and ZnO residue that can deposit on the dielectric layer. Air bubbles that can form in solution during growth affect (c) ZnO growth on a planar surface and (d) interrupt ZnO continuity on LAE stripe mesas.

and GaN is more porous for the *c*-plane sequence compared to the same interface for the semipolar sequence. Based on the SEM characterization of the surface and cross-sectional morphologies in this comparison study, the semipolar solution chemistry was used for the $(20\bar{2}1)$ LAE-ZnO lasers discussed in Chapter 4.5.

Having looked at the morphology of ZnO deposited on a planar bulk substrate, it's important to discuss what ZnO looks like deposited on an LAE $(20\bar{2}1)$ substrate. The top view SEM images in Figs. 4.8(a)-(b) show that as

expected, ZnO films deposit only on exposed p-GaN on the LD ridges. However, if the sample is not properly cleaned before the two-layer deposition or sonicated in between the seed and second layer depositions, ZnO precipitates will form and deposit on the SiO_2 surface. The precipitate density can be mitigated by reducing the amount of precursors available in the growth solution. Figs. 4.8(c)-(d) show the effect that possible air bubbles in the growth solution have on the ZnO surface covereage. Air bubbles can prevent ZnO from nucleating on the GaN surface, as is observed on a bulk $(20\bar{2}1)$ surface in Fig. 4.8(c), and on the stripe mesas of an LAE-patterned $(20\bar{2}1)$ LD sample, as can be seen in Fig. 4.8(d). Stirring the solution with a magnetic stir bar during the two-layer deposition is thus integral to conformal ZnO hydrothermal deposition.

4.4 Device Fabrication

The laser devices discussed in this chapter were fabricated using an LAE-TCO polished facet (PF) process. This PF process is like the PF process used for devices with ITO top cladding in Chapter 3.4 but adapted for the low temperature aqueous deposition of ZnO. It will be referred to as LAE-ZnO PF process henceforth. The semipolar solution chemistry discussed in Chapter 4.3 was used to deposit the ZnO on these devices. The facet polishing method was improved while developing the LAE- ZnO PF process and its respective

polishing sequence upgrades will be discussed as they happened during the fabrication process.

Just like the LAE-ITO PF process, the first step of the LAE-ZnO PF process is the pre-MOCVD growth LAE patterning of the free standing $(20\bar{2}1)$ GaN substrate, using reaction ion etching (RIE) for mesa definition. As shown in Fig. 4.9(a), the LAE stripe mesas were 1 μm deep into the substrate and had varying widths of 4 μm, 8μm, and 14 μm. MOCVD growth of the III-nitride layers of the laser structure and p-GaN activation follow the LAE patterning step. The LAE-ZnO PF process uses a self-aligned ridge waveguide process to define LD ridges of varying widths (1.6, 1.8, 2.0, 4.0 and 8.0 μm) and varying lengths (600 μm, 900 μm and 1200 μm) through a bilayer lithography and an RIE etch, as noted in Fig. 4.9 (a).

MOCVD growth of the III-nitride LD structure is done on the LAE-patterned substrates, depicted in Fig. 4.9(b). Next the laser ridge mesas are delineated: the ridge lithography, shown in Fig. 4.9(c), consists of ~250 nm of non-photosensitive photoresist (PR) to provide the dielectric liftoff undercut (LOL 2000) and ~1.8 μm of positive resist (SPR 955 CM-1.8) to define the LD ridges. The ridge waveguides were defined using a BCl_3/Cl_2 reactive ion etch, that stops 100 nm above the QWs. Following the waveguide etch, 250 nm of SiO_2 was

CHAPTER 4. ZINC OXIDE TOP CLADDING LIMITED AREA EPITAXY LASER DESIGN

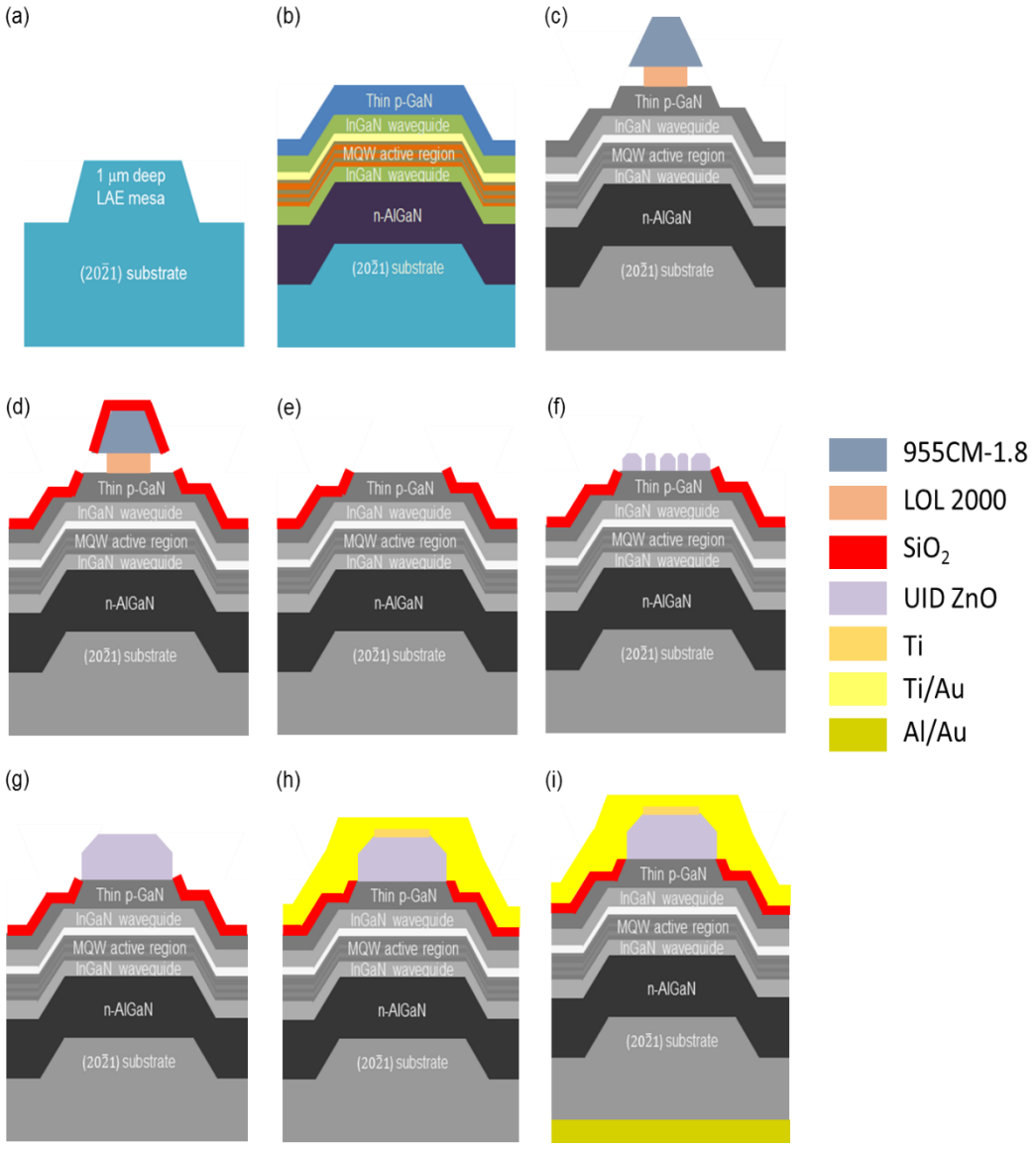

Figure 4.9 Step by step fabrication sequence for the LAE-ZnO PF process, showing an individual ridge's profile for (a) LAE pre-growth mesa patterning (b) MOCVD growth of laser structure, (c) ridge lithography and RIE ridge etch, (d) sputter deposition of dielectric, (e) dielectric liftoff, exposing top of the ridge for ZnO deposition, (f) ZnO seed layer hydrothermal deposition, (g) ZnO 2nd layer hydrothermal deposition, (h) Ti thin metal and Ti/Au top metal lithographies and metal depositions (i) Al/Au common back metal deposition.

deposited via sputtering for electrical isolation, shown in Fig. 4.9(d). The SiO_2 on top of the ridges was then lifted off to expose the top surface of the laser stripes for the preferential hydrothermal deposition of the bilayer ZnO, shown in Fig. 4.9(e).

The samples were cleaned for ZnO depositions using the same two-step acid cleaning process discussed in Chapter 2.4. The total ZnO thickness as measured by Dektak profilometry was 1.43 μm. This is a much thicker ZnO thickness than desired and it highlights the poor thickness control that can happen during low temperature aqueous deposition of ZnO. After the hydrothermal ZnO deposition, which is shown in Fig. 4.9(f)-(g), 30 nm of Ti was deposited by electron beam evaporation along the entire length of the laser ridge for uniform current injection and then 30/1000 nm of Ti/Au metal was deposited also by electron beam evaporation to form a p-contact pad. The thin metal lithography uses negative resist (AZ n-LOF 2020) while the p-contact pad lithography uses a thick bilayer resist (OCG 825/SPR 955 CM-1.8) to enable clean liftoff of ~1 μm of metal. The metal depositions are shown in Figs. 4.9(h)-(i).

The sample was then diced to form laser bars with a cavity length of 600 μm, 900 μm and 1200 μm. The dicing conditions were optimized iteratively during the LD development in this thesis. The latest ADT dicing saw setup optimizations employed for the two-cut dicing sequence, which used a 53 mm

flange and a diamond coated 2.187.4C-9RU-3 blade, showed that the following dicing settings resulted in less dicing-induced chip damage: blade cutting speed at 0.5 mm/sec, spindle rotation at 10 kRPM, first cut height of 0.33 mm and second cut height of 0.06 mm. These settings were used to dice the lasers discussed in this chapter.

Following dicing, the samples were wax-mounted on polishing chucks in the same way as described in Chapter 2.4. The facet polishing sequence had to be modified to reduce the chances of ZnO delamination. The tendency for delamination increase as the ZnO thickness increases.[12,13] The polishing direction also affects the chances for delamination. In our polishing setup (refer to Fig. 2.16 in Chapter 2.4) the clockwise polishing direction tends to accumulate more debris on the polishing surface because the polishing film hits the substrate first.

Fig. 4.10 shows the polished facet damage that results in the delamination of the ZnO top cladding. The dark horizontal lines underneath the ZnO in Fig. 4.10(a) show the gaps that appears between the ZnO and the underlying p-GaN. Delamination can also occur to the dielectric as seen in Fig. 4.10(a) – (b). ZnO can also peel off from the p-GaN during polishing as can be observed in Fig. 4.10(c). The amount of debris that can accumulate on the polishing surface increases when polishing for longer times with finer grit size films. Such debris can cause scratches and cracks and damage the facet surface considerably, as

pointed out in Fig. 4.10(a) and (d). The optical microscope images in Fig. 4.11 show the top view of what PF sample looks like when ZnO delaminates and

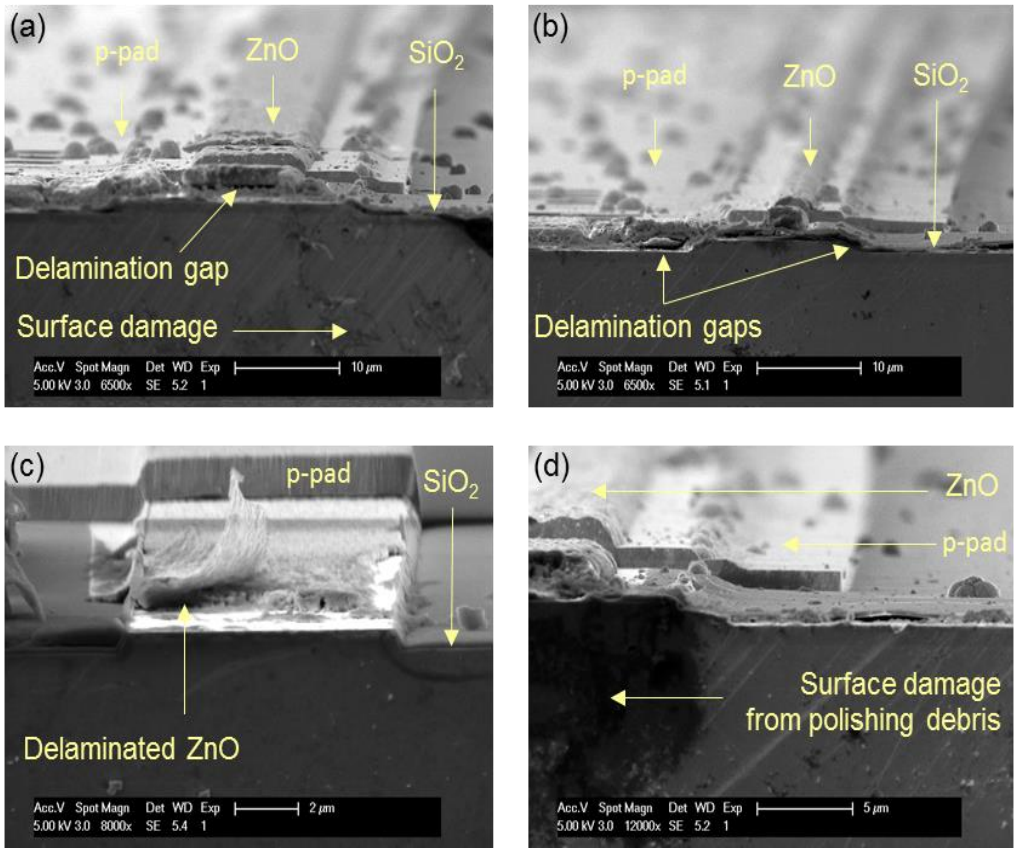

Figure 4.10 Side view SEM images of polishing induced facet surface damage that resulted in (a)-(c) delamination of the ZnO top cladding and partly of the dielectric and (d) scratched and crumbled laser ridge and facet.

crumbles and the facets are damaged. In cases where the intended polishing depth is exceeded or when the sample facet is not well aligned with the polishing chuck's edge, this kind of polishing damage can affect a high number of ridges and decrease the device yield of the process.

CHAPTER 4. ZINC OXIDE TOP CLADDING LIMITED AREA EPITAXY LASER DESIGN

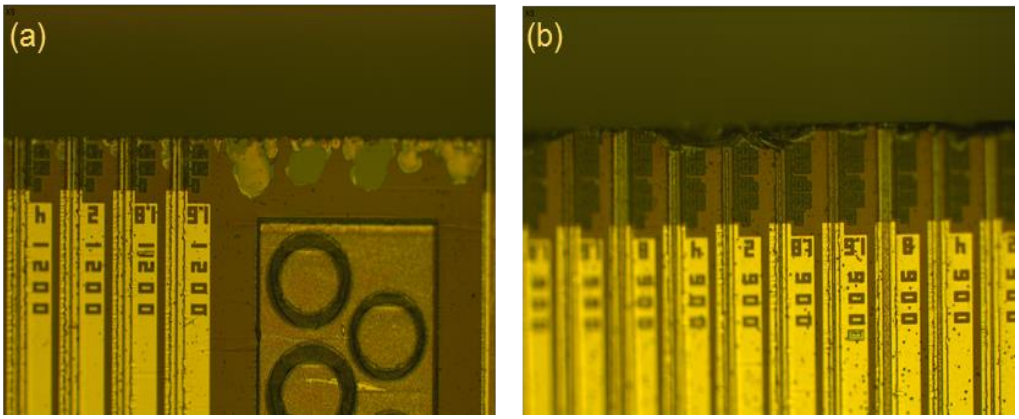

Figure 4.11 Top view optical microscope image of polishing induced damage to (a) the chip edge and (b) to the laser ridges' thin metal edges.

ZnO delamination and facet surface damage were mitigated by starting the facet polish with a much higher grit size, optimizing the polishing rotation direction, chuck oscillation and polishing times. Table 5.2 details the improved polishing sequence and Appendix A. IV discusses the polishing setup and steps in much more detail. Introducing the 30 μm diamond polishing film helped speed up the initial polish which brings the surface of the sapphire corral and the laser's facet flush with each other. In addition, reducing the polishing time of the final three grit sizes greatly reduced facet surface damage because there's less time for polishing residue to accumulate and get stuck on the facet.

This polishing sequence, during which the sample rotation was in counter clockwise (CCW) direction, also included spindle arm oscillation for the larger grit sizes and limited rotation of the chuck for the remaining grit sizes. These

Polishing film grit size (μm)	Polishing film material	Chuck movement	Polishing depth (μm)*	Polishing time
30.0	Diamond	Oscillate	40 - 60	As needed
6.0	Diamond	Oscillate	25 - 40	As needed
3.0	Diamond	Oscillate	15 - 25	As needed
1.0	Diamond	Limit rotation	10 - 15	≤ 5 min
0.3	Diamond	Limit rotation	9	2 min
0.1	Diamond	Limit rotation	9	25-30 sec
0.05	Al_2O_3	Limit rotation	9	25-30 sec
0.02	Al_2O3	Limit rotation	9	20-25 sec

Table 4.2 Polishing sequence detailing the expanded grit size grade, polishing film material, and polishing depth and time per grit size. The polish time of the finer grit size films was reduced dramatically from the times listed in Table 2.5 to decrease chances of delamination and polishing debris-induced surface damage to the laser facets. *The polish depth is measured with respect to the edge of the thin Ti contact layer on the LD ridges and is annotated on the PF mask to monitor the polishing depth during each polish round.

settings facilitate efficient removal of the polished material from the facet-polishing film interface. The laser fabrication was completed with the deposition of a 50/300 nm Al/Au common back side contact via electron beam evaporation, which is illustrated in Fig. 4.10(i). These PF fabricated LDs lased under pulsed and continuous wave operation. The next section will show and discuss the full extent of the LAE-ZnO laser device characterization.

4.5 Device results

The $(20\bar{2}1)$ LAE LD structure, whose results will be discussed in this

section, is shown in Fig. 4.12. It consisted of 600 nm Si-doped GaN template, followed by a 186 period $Al_{0.1}Ga_{0.9}N$/GaN modulation-doped SPSL n-cladding, having a total thickness of ~750 nm and average AlN fraction of 5%. Following the cladding, the structure consisted of a 60 nm n-$In_{0.08}Ga_{0.92}N$ waveguiding layer, an undoped active region consisting of three unintentionally doped (UID) 3.7 nm $In_{0.2}Ga_{0.8}N$ QWs and four 7.6 nm GaN QBs, a 10 nm p-$Al_{0.21}Ga_{0.79}N$ EBL, a 40 nm p-$In_{0.08}Ga_{0.92}N$ waveguiding layer, a 205 nm p-GaN layer, and 12 nm p^+ GaN contact layer. The low temperature aqueous solution deposited ZnO bi-layer was 1.43 μm thick. This thickness is higher than desired or necessary for a laser cladding, but we have poor control over film thickness when using low temperature aqueous solution or hydrothermal deposition of ZnO. Optical

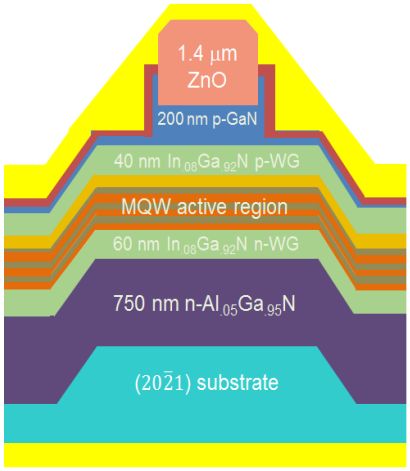

Figure 4.12 The LAE-ZnO semipolar LD layer structure for the devices discussed in Chapter 4.5. The orange layer above the active region is p-AlGaN EBL layer. The layer thicknesses and compositions are detailed above.

modeling done using the assumptions outlined in Chapter 3.3, indicate this structure had a Γ of 4.7% and a_i of 15.09 cm^{-1}.

The pulsed light-current-voltage (*L-I-V*) measurement from the 900 μm bar, followed by the pulsed results from the 1200 μm bar will be discussed in Chapter 4.5.1. The laser bar mounting for CW operation and CW results from the 900 μm bar will be discussed in Chapter 4.5.2 to complete the section. The LAE-ZnO PF process had a very high yield. Pulsed lasing was achieved from laser bars of different lengths: 900 μm and 1200 μm. The quality of the mirrors of the lasers on the 900 μm long chip was much better than those of the 1200 μm long chip. The poor mirror quality caused poor performance of the 1200 μm chip, therefore length dependent analysis for internal parameters was not performed. After pulsed laser testing, the 900 μm long chip was mounted on a Cu block and tested in continuous wave (CW) operation. CW operation was achieved for multiple 4 μm wide x 900 μm long LD ridges. This is the first CW operation demonstration of a blue LD grown on $(20\bar{2}1)$ at UCSB.

4.5.1 Pulsed operation device results

The LAE-ZnO PF process had a very high yield. Unlike the LAE-ITO laser demonstrated in Chapter 3.5, pulsed lasing was achieved from all ridge

widths for the 900 μm and 1200 μm bar. This was the first semipolar TCO PF LD process to result in multiple, different length LD ridges that didn't fail after the first or second *L-I-V* measurement and we believe it was facilitated by the better LD design and much improved polishing sequence. Thus, it was possible to measure the *L-I-V* from both facets for each lasing LD ridge and compare the polishing quality of a given LD bar's mirror facet surfaces.

It would be too cluttered and nonintuitive to plot the *L-I-V* curves for each ridge that lased on the 900 μm bar. Instead the *L-I-V* for the ridge with the highest

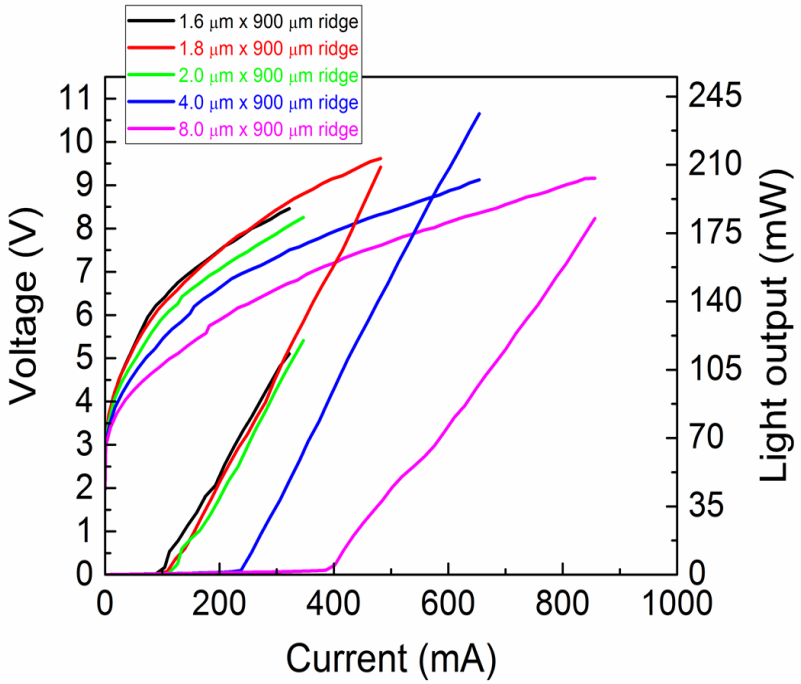

Figure 4.13 Pulsed *L-I-V* characteristics from each ridge width on the 900 μm long PF bar. These are *L-I-V* curves from a single facet so they represent the highest single facet differential efficiency per given ridge width. The best double facet differential efficiencies per ridge width are tabulated in Table. 4.3.

single facet slope efficiency is plotted in Fig. 4.13, for each of the five ridge widths of the 900 μm long bar. The devices were tested under pulsed electrical injection with a pulse width of 1μs and 1% duty cycle. The slope efficiency, η_{sl}, expressed in units of W/A, is the slope of the *L-I* curve, calculated at currents higher than the threshold current, I_{th}.[14] The differential efficiency, η_d, per facet, can then be calculated using equation 4.1. To get the double facet slope and differential efficiencies of a ridge, the values of each facet are added together. For each ridge width that lased the threshold conditions and other *L-I-V* parameters for the ridges with the highest double facet differential efficiency are tabulated in Table 4.3. We picked the differential gain as a metric for evaluating the

$$\eta_d = \left[\frac{q}{h\nu}\right]\frac{dP_0}{dI}, \quad (I > I_{th}) \tag{4.1}$$

Ridge Dimensions	J_{th} (kA/cm^2)	V_{th} (V)	R_d (Ω)	P_{out} (mW)	η_{sl} (W/A)	η_d (%)
1.6 mm x 900 mm	6.47	6.30	8.56	113.24	0.73	26.07
1.8 mm x 900 mm	6.75	6.36	7.39	208.81	0.77	27.72
2.0 mm x 900 mm	6.03	6.05	8.32	119.94	0.72	25.75
4.0 mm x 900 mm	6.57	6.94	4.82	236.17	1.03	36.80
8.0 mm x 900 mm	5.34	7.13	4.36	182.48	0.59	21.12

Table 4.3 Threshold conditions and other parameters attained from *L-I-V* characteristics for each ridge width on the 900 μm long PF bar. Only the ridges with the highest double facet differential efficiency are tabulated.

replacement of ITO with ZnO in the top cladding and as a parameter directly related to LD wall plug efficiency.[14]

The LIV curves in Fig. 4.13 show an increasing current threshold for increasing ridge width. The threshold current density, J_{th}, for all the ridge widths plotted in Fig. 4.13 is lower than the J_{th} of the LAE-ITO laser discussed in Chapter 3.5. The threshold voltage, V_{th}, follows a similar pattern: for all the ridge widths tabulated in Table 4.3, the V_{th} is lower than that of both the planar-ZnO and LAE-ITO LD devices reported in Chapters 2.5 and 3.5, respectively. The pulsed differential resistance has a spread, but is lower for the widest ridges.

The η_d values for these LDs, are in line with the η_d value attained from the planar-ZnO LDs reported in Chapter 2.5, with the 4 μm wide ridge resulting in the highest η_d value of 36.8%. The power output, *Pout*, of these LAE-ZnO LDs showed a remarkable improvement over the blue TCO LDs reported in Chapter 2.5 and 3.5,[2] and the blue LAE LDs reported by Hardy *et. al.*[5] The power output observed from the 4 μm x 900 μm ridge is the highest optical power output reported on $(20\bar{2}1)$ from UCSB.

Although this LAE-ZnO PF process was improved compared to the planar-ZnO and LAE-ITO PF processes, it is still affected by the alignment and parallelity of the LD bar to the polishing chuck edge and the uniformity of the

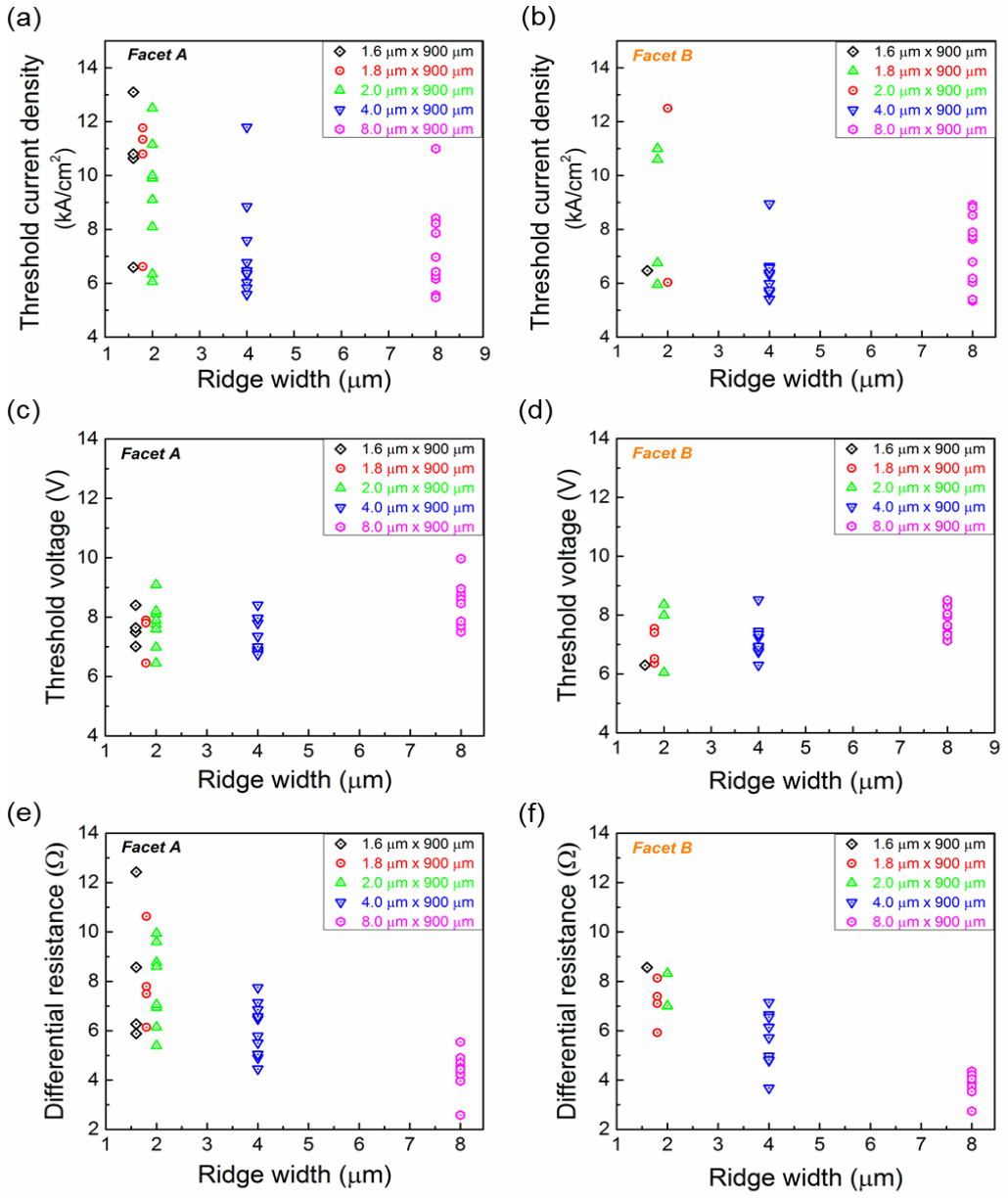

Figure 4.14 Pulsed *L-I-V* results showing the parameter value ranges for both facets of all the 900 μm long ridges that lased, including J_{th} for (a) facet A and (b) facet B; V_{th} for (c) facet A and (d) facet B; R_d for (e) facet A and (f) facet B. Facet A refers to the facet on which the ridge length is denoted in the PF mask set, namely the top facet seen in Fig. 4.11.

TCO in the top cladding. Mirror facet polishing quality is also affected by how much wax bond is between the LD bar and the top sapphire corral (the thinner the wax bond the better). All these factors and possible In composition fluctuations in the active region,[15–18] as well as probe placement and contact during *L-I-V* characterization could have facilitated the considerable range in parameter value per given ridge width. To visualize the pulsed data spread, all parameters, including J_{th}, V_{th}, R_d, P_{out}, η_{sl} and η_d, for all the ridges that lased were plotted in Figs 4.15 and 4.16 for each facet of the 900 μm long bar. Furthermore, for all LD ridge widths, statistical analysis was done for each parameter for each facet. That analysis is shown in Tables 4.4 through 4.8, for ridge widths of 1.6 mm, 1.8 mm, 2.0 mm, 4.0 mm and 8.0 mm, respectively.

Not all ridge widths had the same laser yield. The 1.6 μm wide ridges had the lowest yield and the 2.0 μm wide ridges had the highest LD failure going from measuring facet to measuring facet B. Facet A refers to the side of the LD bar on which the ridge length (i.e. 900 μm or 1200 μm) is marked on the PF mask set. An example of this demarcation is the top side of the bars shown in Fig. 4.11. Facet B is the opposite side, which is unmarked for all three ridge lengths on the PF mask set. The highest LD yield came from the 4 μm and the 8 μm ridges, with at least 10 lasers per facet for each width.

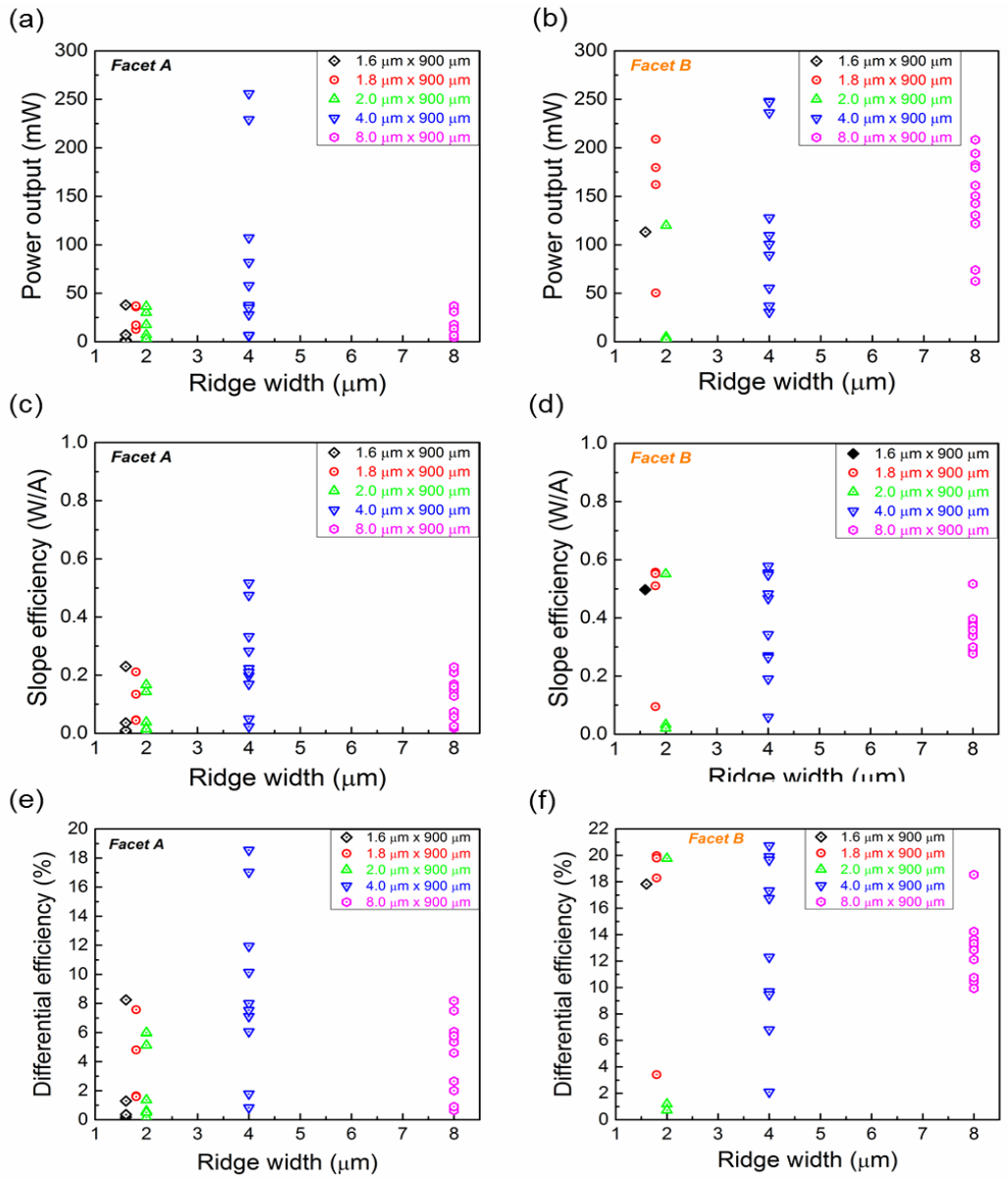

Figure 4.15 Pulsed *L-I-V* results showing the parameter value ranges for both facets of all the 900 μm long ridges that lased, including P_{out} for (a) facet A and (b) facet B; η_{sl} for (c) facet A and (d) facet B; η_d for (e) facet A and (f) facet B. Facet A refers to the facet on which the ridge length is denoted in the PF mask set, namely the top facet seen in Fig. 4.11.

Parameter	Units	Facet A	Facet B
Average J_{th}	kA/cm^2	10.28	6.47
Std. Dev.	kA/cm^2	5.47	-
Lowest J_{th}	kA/cm^2	*6.59*	*6.47*
Average V_{th}	V	7.64	6.30
Std. Dev.	V	0.58	-
Lowest V_{th}	V	*7.01*	*6.30*
Average R_d	Ω	8.29	8.56
Std. Dev.	Ω	3.01	-
Lowest R_d	Ω	*5.88*	*8.56*
Average P_{out}	mW	12.01	113.24
Std. Dev.	mW	17.46	-
Highest P_{out}	mW	*37.86* *	*113.24*
Average η_{sl}	W/A	0.07	0.50
Std. Dev.	W/A	0.11	-
Highest η_{sl}	W/A	*0.23*	*0.50*
Average η_d	%	2.51	17.82
Std. Dev.	%	-	-
Highest η_d	%	*8.25*	*17.82*

Table 4.4 Average, standard deviation and optimal (lowest or highest, depending on parameter) values for pulsed *L-I-V* parameters including J_{th}, V_{th}, R_d, P_{out}, η_{sl} and η_d of the 1.6 μm x 900 μm LDs. Facet A had 3 *L-I-V* points while Facet B had 1 point per parameter. This ridge width had the lowest yield and the quality of the two facets can't realistically be compared due to the lack of facet B data points. *The power output measurement was capped at 50 mW for when measuring facet A, therefore the power output between the two facets is so different. Judging from the one point, slope and differential efficiency values indicate that facet B had better polishing quality.

Parameter	Units	Facet A	Facet B
Average J_{th}	kA/cm^2	10.13	8.58
Std. Dev.	kA/cm^2	2.38	2.60
Lowest J_{th}	kA/cm^2	*6.62*	*5.95*
Average V_{th}	V	7.49	6.96
Std. Dev.	V	0.69	0.60
Lowest V_{th}	V	*6.45*	*6.36*
Average R_d	Ω	8.02	7.14
Std. Dev.	Ω	1.89	0.92
Lowest R_d	Ω	*7.50*	*5.92*
Average P_{out}	mW	25.61	150.20
Std. Dev.	mW	12.54	69.39
Highest P_{out}	mW	*36.87*	*208.81*
Average η_{sl}	W/A	0.11	0.43
Std. Dev.	W/A	0.08	0.22
Highest η_{sl}	W/A	*0.21*	*0.56*
Average η_d	%	3.90	15.37
Std. Dev.	%	-	-
Highest η_d	%	*7.57*	*19.98*

Table 4.5 Average, standard deviation and optimal (lowest or highest, depending on parameter) values for pulsed *L-I-V* parameters including J_{th}, V_{th}, R_d, P_{out}, η_{sl} and η_d of the 1.8 μm x 900 μm LDs. Both facets A and B had 4 *L-I-V* points per parameter. The power output measurement for facet A was capped at 50 mW before realizing the LD quality; facet A was not remeasured for fear of burning out or damaging the ridges. The power output measurements for facet B were capped at 500 mW so the power output between the two facets is so different. The different R_d values could be due to the probe contact or ZnO nonuniformity. Judging from this ridge width's average and optimal values, facet B had better polishing quality and higher single facet differential efficiency.

Parameter	Units	Facet A	Facet B
Average J_{th}	kA/cm^2	8.83	12.78
Std. Dev.	kA/cm^2	2.25	6.89
Lowest J_{th}	kA/cm^2	*6.06*	*6.03*
Average V_{th}	V	7.71	7.47
Std. Dev.	V	0.85	1.24
Lowest V_{th}	V	*6.45*	*6.05*
Average R_d	Ω	7.93	7.44
Std. Dev.	Ω	1.75	0.76
Lowest R_d	Ω	*5.39*	*6.99*
Average P_{out}	mW	14.12	42.36
Std. Dev.	mW	14.15	67.20
Highest P_{out}	mW	*36.3* *	*119.94*
Average η_{sl}	W/A	0.08	0.20
Std. Dev.	W/A	0.07	0.30
Highest η_{sl}	W/A	*0.17*	*0.55*
Average η_d	%	2.87	7.22
Std. Dev.	%	-	-
Highest η_d	%	*5.99*	*19.76*

Table 4.6 Average, standard deviation and optimal (lowest or highest, depending on parameter) values for pulsed *L-I-V* parameters including J_{th}, V_{th}, R_d, P_{out}, η_{sl} and η_d of the 2.0 μm x 900 μm LDs. Facet A had 7 *L-I-V* points while Facet B had 3 point per parameter. This ridge width had the most failed devices going from facet A to facet B, as can is reflected in their respective number of data points. *The power output measurement was capped at 50 mW for when measuring facet A, therefore the power output between the two facets is so different. Facet B seems to have better polishing quality, but the lower number of data points and higher standard deviations make this observation inconclusive.

Parameter	Units	Facet A	Facet B
Average J_{th}	kA/cm^2	7.02	7.54
Std. Dev.	kA/cm^2	1.85	3.74
Lowest J_{th}	kA/cm^2	*5.58*	*5.41*
Average V_{th}	V	7.38	7.11
Std. Dev.	V	0.58	0.59
Lowest V_{th}	V	*6.74*	*6.30*
Average R_d	Ω	5.96	5.66
Std. Dev.	Ω	1.07	1.07
Lowest R_d	Ω	*4.45*	*3.68*
Average P_{out}	mW	80.09	128.12
Std. Dev.	mW	85.91	85.64
Highest P_{out}	mW	*255.87*	*248.03*
Average η_{sl}	W/A	0.24	0.38
Std. Dev.	W/A	0.15	0.18
Highest η_{sl}	W/A	*0.48*	*0.58*
Average η_d	%	8.63	13.47
Std. Dev.	%	-	-
Highest η_d	%	*17.04*	*20.73*

Table 4.7 Average, standard deviation and optimal (lowest or highest, depending on parameter) values for pulsed *L-I-V* parameters including J_{th}, V_{th}, R_d, P_{out}, η_{sl} and η_d of the 4.0 μm x 900 μm LDs. Facet A had 11 *L-I-V* points while Facet B had 10 point per parameter. This ridge width had high yield from both facets. The electrical parameters are comparable on average and optimally for both facets, while the single facet slope efficiency is higher for facet B. Overall, the data indicates that facet B had better polishing quality, in agreement with the observations made for this facet in Tables 4.4 - 4.6.

Parameter	Units	Facet A	Facet B
Average J_{th}	kA/cm^2	7.24	7.21
Std. Dev.	kA/cm^2	1.69	1.32
Lowest J_{th}	kA/cm^2	*4.71*	*5.40*
Average V_{th}	V	8.42	7.88
Std. Dev.	V	0.74	0.49
Lowest V_{th}	V	*7.50*	*7.13*
Average R_d	Ω	4.36	3.89
Std. Dev.	Ω	0.76	0.44
Lowest R_d	Ω	*2.58*	*2.74*
Average P_{out}	mW	25.31	146.13
Std. Dev.	mW	13.45	46.84
Highest P_{out}	mW	*36.91*	*208.31*
Average η_{sl}	W/A	0.12	0.36
Std. Dev.	W/A	0.07	0.07
Highest η_{sl}	W/A	*0.23*	*0.52*
Average η_d	%	4.36	12.91
Std. Dev.	%	-	-
Highest η_d	%	*8.18*	*18.54*

Table 4.8 Average, standard deviation and optimal (lowest or highest, depending on parameter) values for pulsed *L-I-V* parameters including J_{th}, V_{th}, R_d, P_{out}, η_{sl} and η_d of the 8.0 μm x 900 μm LDs. Facet A had 10 *L-I-V* points while Facet B had 11 point per parameter. This ridge width had high yield from both facets. The power output measurement for facet A was capped at 50 mW, while for facet B it was capped at 300 mW. The parameters are comparable for both facets, which indicates that possible ZnO or material nonuniformities are less noticeable for a wider ridge. Overall, the data indicates that facet B had better polishing quality, in agreement with the observations made for this facet for all the other PF ridge widths.

For all ridge widths, excluding the 4.0 μm wide ridge, the maximum measurable P_{out} for facet A *L-I-V*s was capped at 50 mW and the measurements were done before realizing the high quality and optical power output of the lasers. Facet A *L-I-V*s were not repeated to avoid damaging or burning out the lasers after having measured facet B. That is the reason for the power output values being so different between the two facets, in Tables, 4.4 - 4.6 and Table 4.8. The reason for the different slope and differential efficiencies between the different

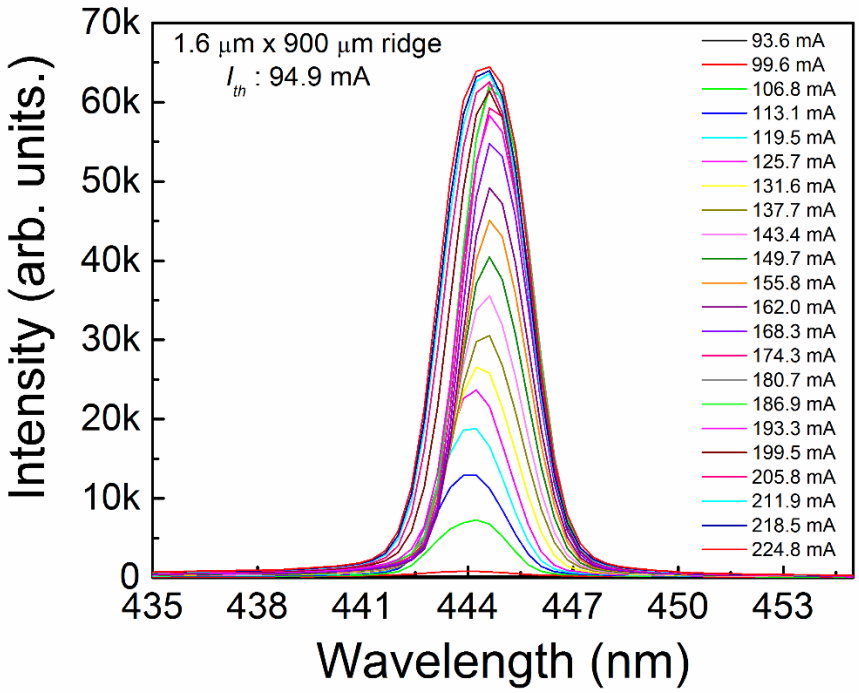

Figure 4.16 Pulsed, current dependent spectra of a 1.6 μm wide by 900 μm long LD, emitting at 445 nm for currents higher than the threshold current of 94.9 mA. This wavelength and spectra is representative of the other ridge widths from this PF laser bar.

facets of a given ridge width are due to different polishing quality. Judging from the data in Tables 4.4 – 4.8, facet B had better polishing and mirror facet quality.

Fig. 4.16 shows the current dependent spectra for a 1.6 μm wide by 900 μm long LD. Single peak emission was achieved at 445 nm at a 2.37I_{th} current value. The 900 μm had uniform emission wavelength for the various ridge widths. Fig. 4.17 shows the pulsed *L-I-V* far field patterns for 1.6 μm, 1.8 μm, and 8.0 μm wide LDs. Multiple modes are visible in the far field pattern of the 8.0 μm wide LD at currents much higher than threshold. Fig. 4.18 shows the pulsed temperature dependent *L-I-V* curves of a 4.0 μm wide x 900 μm long LD. The I_{th} increases with increasing stage temperature, as expected.

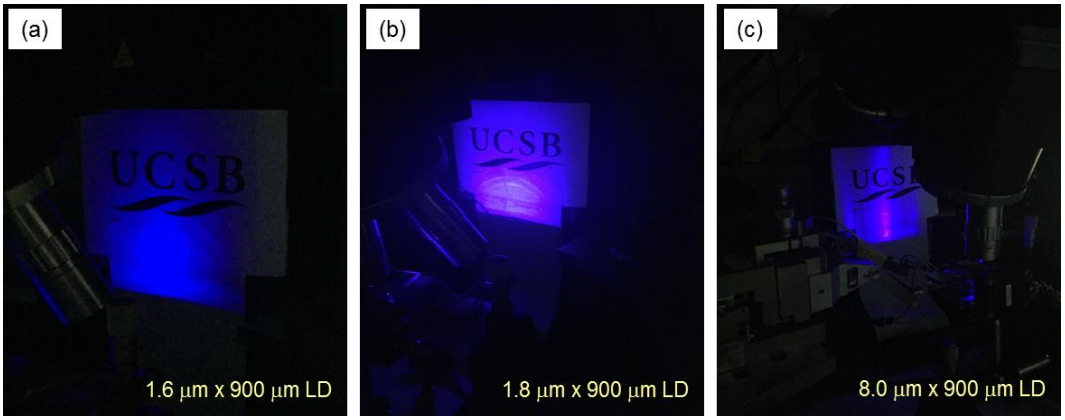

Figure 4.17 Pulsed *L-I-V* far field patterns for (a) 1.6 μm, (b) 1.8 μm and (c) 8.0 μm wide LDs. Multiple modes are visible in the far field pattern of the 8.0 μm wide LD.

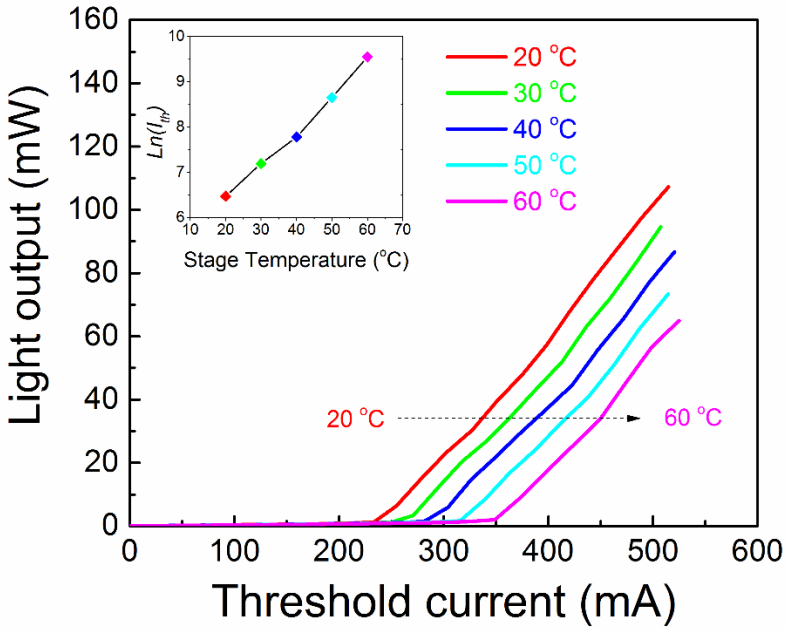

Figure 4.18 Pulsed temperature dependent *L-I-V* for a 4.0 μm wide x 900 μm long LD, showing increasing I_{th} with increasing stage temperature. The inset shows the natural log of I_{th} versus stage temperature. The inverse of the slope of the linear fit of the ln(I_{th}) vs temperature data gives the T_o of the device, which was found to be 103.7 K.

The LDs characteristic temperature, T_o, can be calculated by linearly fitting the dependence of the logarithmus naturalis of the threshold current on the measurement setup stage temperature; a dependence that is shown in the inset graph of Fig. 4.18, for a stage temperature ranging from 20 °C to 60 °C. The inverse of the slope of that linear fit is the laser's T_o value.[14] For the LD analyzed in Fig. 4.18, the T_o value was calculated to be 103.7 K. The characteristic temperature is a measure of the laser structure's insensitivity to thermal changes during operation: a higher T_o value, indicates lower susceptibility of the device

performance to temperature fluctuations during lasing. This blue $(20\bar{2}1)$ LAE-ZnO T_o of 103.7 K is higher than the T_o for blue *m*-plane LDs reported by Farrell *et.al.*[19] and lower than the T_o for green $(20\bar{2}1)$ LDs reported by Sizov *et.al.*[20] The blue $(20\bar{2}1)$ LAE-ZnO T_o is expected to be lower than the green $(20\bar{2}1)$ T_o because the shallower QWs are expected to have more carrier overflow.

As mentioned, the mirror facet quality of the 1200 μm bar was very poor because the ZnO delaminated during polishing, as shown in Figs. 4(a)-(b). Even with such poor facets, lasing was achieved from all the ridge widths on this bar. The devices were tested under pulsed electrical injection with a pulse width of 1μs and 1% duty cycle. Fig. 4.19 shows the *L-I-V* characteristics for each ridge width for the 1200 μm bar, choosing the LDs with the highest P_{out} per given ridge width. The laser performance parameters, attained from the *L-I-V* characteristics are tabulated in Table. 4.9. Fig. 4.12 show, as expected, that I_{th} increases with increasing ridge width and that the single facet P_{out} is much lower than the P_{out} observed for the same original PF chip's 900 μm long ridges. The R_d values are lower than those observed for the 900 μm long ridges which could indicate either local increased uniformity of the ZnO layer or better probe contact during *L-I-V* testing. The single facet slope efficiencies and in turn differential efficiencies are as expected very low compared to the values observed from either facet of the 900

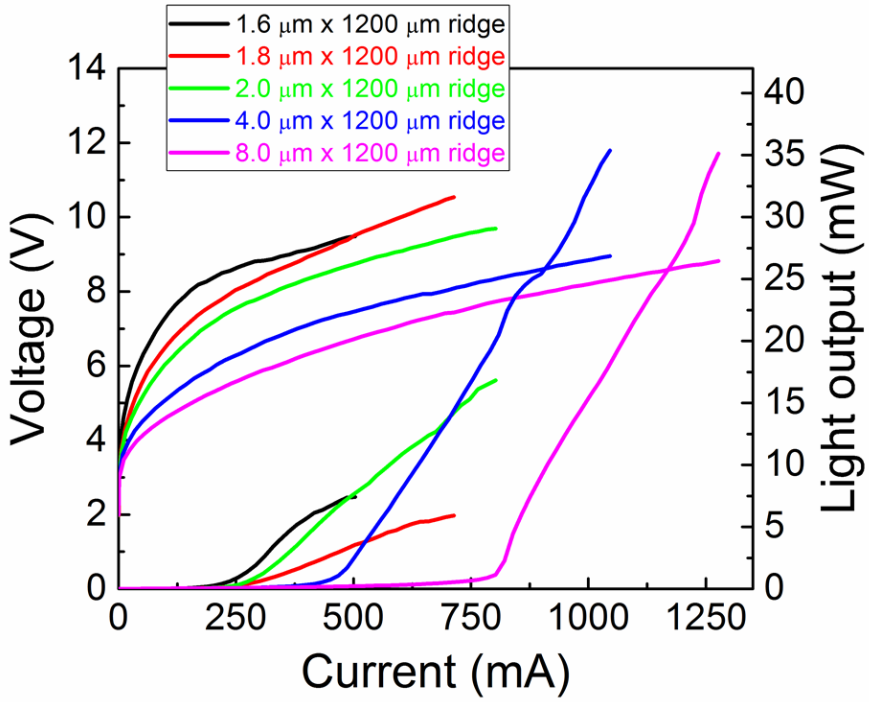

Figure 4.19 Pulsed *L-I-V* characteristics from each ridge width on the 900 μm long PF bar. These are *L-I-V* curves from a single facet so they represent the highest single facet differential efficiency per given ridge width. The best double facet differential efficiencies per ridge width are tabulated in Table. 4.3.

Ridge Dimensions	J_{th} (kA/cm^2)	V_{th} (V)	R_d (Ω)	P_{out} (mW)	η_{sl} (W/A)	η_d (%)
1.6 μm x 1200 μm	10.40	8.38	3.33	7.42	0.04	1.32
1.8 μm x 1200 μm	10.20	7.77	5.41	6.08	0.02	0.54
2.0 μm x 1200 μm	10.40	7.59	3.81	16.83	0.03	1.20
4.0 μm x 1200 μm	9.45	7.30	2.74	35.37	0.05	1.94
8.0 μm x 1200 μm	8.24	7.69	2.30	35.12	0.09	3.19

Table 4.9 Threshold conditions and other parameters attained from *L-I-V* characteristics for each ridge width on the 1200 μm long PF bar. Only the ridges with the highest single facet optical power output are tabulated.

μm long ridges. This correlates to the SEM imaging of the very poor quality of polishing that occurred for this PF laser bar. The 1200 μm bar was polished before the polishing sequence improvements that were discussed in Chapter 4.4 were developed and employed.

4.5.2 Continuous wave operation device results

Based on the promising pulsed *L-I-V* characteristics of the PF LAE-ZnO 900 μm long bar, discussed at length in the previous section, we decided to mount this LD bar on a Cu heatsink using Pb/Sn solder and test whether the lasers would lase in continuous wave (CW) operation. To prepare the samples for Cu heatsink mounting, an additional metal stack was deposited on top of the existing Al/Au common back metal. Prior to the additional back metallization, the 900 μm bar was thoroughly solvent cleaned with a standard 2 min Acetone: 2 min Isopropanol: 2 min DI water rinse sequence. Following the solvent cleaning step, the sample was mounted with photoresist (PR) on a silicon piece and the following metal stack was electron beam deposited: 50 Å Ti – 300 Å Ni – 3000 Å Au. Ti ensures adhesion and Ni acts as a diffusion barrier. Out of all the LD ridge widths that lased in pulsed mode on the 900 μm bar, only the 4.0 μm wide

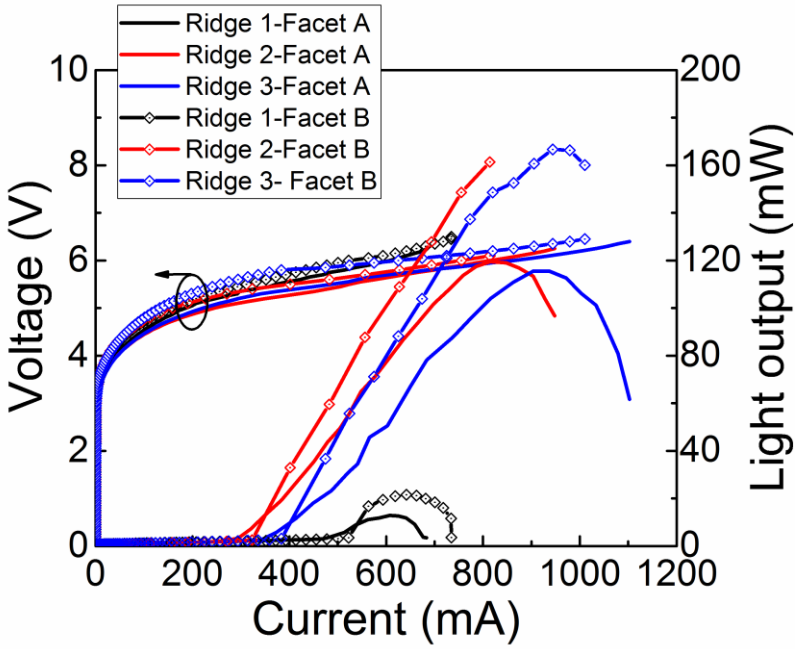

Figure 4.20 CW double facet *L-I-V* characteristics for three 4.0 μm wide by 900 μm long LDs. Facet B was tested first. Thus, the optical power at which thermal rollover occurs for facet B's *L-I* curves, denoted by open symbols, is higher than that at which thermal rollover occurs for facet A's *L-I* curves, denoted by solid lines. The CW R_d values are much lower than the pulsed R_d values.

ridges lased in CW mode. We could measure *L-I-V* characteristics for both facets for only three of the 4.0 μm x 900 μm LDs that lased in CW. Those double facet *L-I-V* characteristics are shown in Fig. 4.20.

Facet B was measured first as can be seen by the higher rollover optical power observed in the *L-I-V* curves denoted by open symbols. While these lasers emitted light from both facets, their performance is nonuniform. The hero CW laser's *L-I-V* parameter values were as follows: J_{th} was 10.43 kA/cm^2, V_{th} was

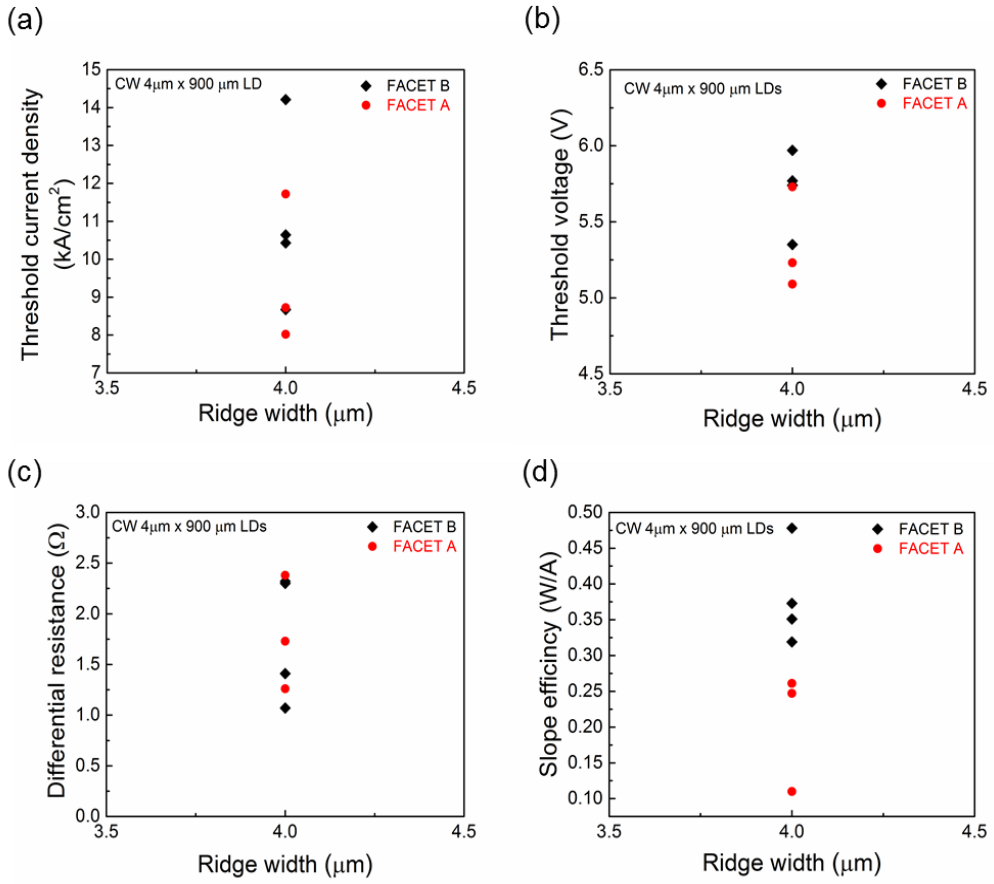

Figure 4.21 CW *L-I-V* results showing the parameter value ranges for both facets of all the 900 μm long ridges that lased, including (a) J_{th} ; (b) V_{th} ; (c) R_d ; and (d) η_{sl} Facet A refers to the facet on which the ridge length is denoted in the PF mask set, visualized as the top facet seen in Fig. 4.11.

5.77 V, R_d was 1.07 Ω, P_{out} was 166.68 mW, single facet η_{sl} was 0.37 W/A while double facet η_{sl} was 0.63 W/A, corresponding to a double facet η_d of 22.59 %. The full spread of the all the CW laser parameters obtained for both facets of the 4.0 μm x 900 μm LDs is shown in Fig. 4.21. The R_d of these CW LDs were quite low and comparable to green CW LD literature values.[21]

4.6 Conclusions

In summary, we have improved the blue $(20\bar{2}1)$ LAE-TCO design by thinning out the n-AlGaN bottom cladding, thinning out the QWs in the active region, replaced ITO with ZnO in the top cladding and optimizing the hydrothermal deposition solution chemistry and structurally characterizing the improved ZnO films and improving the polishing sequence for mirror facet formation. These optimization efforts resulted in a high LD yield PF process with improved pulsed *L-I-V* characteristics and the first CW LD demonstration on $(20\bar{2}1)$ at UCSB.

4.7 Future work

The results attained in this dissertation, especially the LAE-ZnO CW devices, are very encouraging. There is still a lot of room for improvement and optimization. LAE has been used to demonstrate green emitting $(20\bar{2}1)$ lasers,[22] so a natural next step is to push this design to longer wavelengths, initially towards green. Given that the index contrast between III-nitride alloys and GaN decreases as operating wavelength increases,[23] the modeling results from Chapter 3.3 and 4.2 indicated that LAE-enabled higher Al composition and thinner bottom cladding can be utilized in the push towards longer wavelengths. The LD active region also has room for optimization, specifically: QW number and thickness,

QB thickness, EBL doping grade and growth temperature, and the In composition and total thickness of the InGaN waveguide. The p-GaN doping grade and growth temperature merit further optimization.

CAIBE fabricated LDs have recently shown very promising results,[24,25] so the CAIBE process should be applied the LAE-TCO LD facet formation to mitigate mirror facet quality nonuniformities that arise from the current polishing setup. The ZnO deposition method also has much room for improvement. Preliminary work has shown that using either atomic layer deposition (ALD) or electron beam deposition for the ZnO seed layer combined with hydrothermal deposition of the ZnO 2nd layer results in lower forward voltages in LEDs. Therefore, the ZnO top cladding deposition method merits further development and optimization. Finally, a systematic CTLM comparison study of the ITO and ZnO contact quality to the p-GaN layer on semipolar devices as well as on bulk p-GaN should be performed to deconvolute the sources of the highest contributions to the LD operation voltage.

Bibliography

[1] E. Kioupakis, P. Rinke, A. Schleife, F. Bechstedt, and C.G. Van de Walle, Phys. Rev. B **81**, 241201 (2010).

[2] A. Myzaferi, A.H. Reading, D.A. Cohen, R.M. Farrell, S. Nakamura, J.S. Speck, and S.P. DenBaars, Appl. Phys. Lett. **109**, 61109 (2016).

[3] M.T. Hardy, Stress Engineering for Semipolar (20 $\bar{}$ 21) Blue and Green InGaN Based Laser Diodes, 2013.

[4] T. Kyono, Y. Yoshizumi, Y. Enya, M. Adachi, S. Tokuyama, M. Ueno, K. Katayama, and T. Nakamura, Appl. Phys. Express **3**, 18 (2010).

[5] M.T. Hardy, S. Nakamura, J.S. Speck, and S.P. Denbaars, Appl. Phys. Lett. **101**, 0 (2012).

[6] R. Goldhahn, a. T. Winzer, a. Dadgar, a. Krost, O. Weidemann, and M. Eickhoff, Phys. Status Solidi Appl. Mater. Sci. **204**, 447 (2007).

[7] E. Kioupakis, P. Rinke, and C.G. Van De Walle, Appl. Phys. Express **3**, 82101 (2010).

[8] M.T. Hardy, C.O. Holder, D.F. Feezell, S. Nakamura, J.S. Speck, D. a. Cohen, and S.P. DenBaars, Appl. Phys. Lett. **103**, 81103 (2013).

[9] A.H. Reading, J.J. Richardson, C.-C. Pan, S. Nakamura, and S.P. DenBaars, Opt. Express **20**, A13 (2012).

[10] A.J. Mughal, S. Oh, A. Myzaferi, S. Nakamura, J.S. Speck, and S.P. Denbaars, Electron. Lett. **52**, 304 (2016).

[11] A.H. Reading, Aqueous Synthesis of Zinc Oxide Films for GaN Optoelectronic Devices, University of California Santa Barbara, 2014.

[12] B. Huang, M.-H. Zhao, and T.-Y. Zhang, Philos. Mag. **84**, 1233 (2004).

[13] J. MacHado, N. Ravishankar, and M. Rajamathi, Solid State Sci. **12**, 1399 (2010).

[14] L.A. Coldren, S.W. Corzine, and M.L. Masanovic, *Diode Lasers and Photonic*

Integrated Circuits (John Wiley & Sons, Inc., 2012).

[15] T.J. Prosa, P.H. Clifton, H. Zhong, A. Tyagi, R. Shivaraman, S.P. Denbaars, S. Nakamura, and J.S. Speck, Appl. Phys. Lett. **98**, (2011).

[16] D.A. Browne, B. Mazumder, Y.-R. Wu, and J.S. Speck, J. Appl. Phys. **117**, 185703 (2015).

[17] R. Shivaraman, Y. Kawaguchi, S. Tanaka, S.P. Denbaars, S. Nakamura, and J.S. Speck, Appl. Phys. Lett. **102**, 2011 (2013).

[18] Y.-R. Wu, R. Shivaraman, K.-C. Wang, and J.S. Speck, Appl. Phys. Lett. **101**, 83505 (2012).

[19] R.M. Farrell, D.A. Haeger, P.S. Hsu, K. Fujito, D.F. Feezell, S.P. Denbaars, J.S. Speck, and S. Nakamura, Appl. Phys. Lett. **99**, 17 (2011).

[20] D. Sizov, R. Bhat, K. Song, D. Allen, B. Paddock, S. Coleman, L.C. Hughes, and C.E. Zah, Appl. Phys. Express **4**, 1 (2011).

[21] T. Miyoshi, S. Masui, T. Okada, T. Yanamoto, T. Kozaki, S.I. Nagahama, and T. Mukai, Appl. Phys. Express **2**, (2009).

[22] M.T. Hardy, F. Wu, P. Shan Hsu, D.A. Haeger, S. Nakamura, J.S. Speck, and S.P. Denbaars, J. Appl. Phys. **114**, 0 (2013).

[23] J. Piprek, *Semiconductor Optoelectronic Devices* (Academic Press, California, 2003).

[24] D.L. Becerra, L.Y. Kuritzky, J. Nedy, A. Saud Abbas, A. Pourhashemi, R.M. Farrell, D.A. Cohen, S.P. DenBaars, J.S. Speck, and S. Nakamura, Appl. Phys. Lett. **108**, (2016).

[25] L.Y. Kuritzky, D.L. Becerra, A.S. Abbas, J.G. Nedy, S. Nakamura, D.A. Cohen, and S.P. DenBaars, Semicond. Sci. Technol. **31**, 1 (2016).